

UNDERSTANDING OF MUTUAL INTERACTIONS BETWEEN LIQUID JETS: ENTRAINMENT AND SHEET FORMATION

A DISSERTATION

*Submitted in partial fulfilment of the
requirements for the award of the degree*

of

**INTEGRATED DUAL DEGREE
(BACHELOR OF TECHNOLOGY & MASTER OF TECHNOLOGY)**

in

**MECHANICAL ENGINEERING
(With Specialization in Thermal Engineering)**

By

VATSAL SANJAY



**DEPARTMENT OF MECHANICAL & INDUSTRIAL ENGINEERING
INDIAN INSTITUTE OF TECHNOLOGY ROORKEE
ROORKEE - 247 667 (INDIA)**

MAY, 2018

**©INDIAN INSTITUTE OF TECHNOLOGY ROORKEE, ROORKEE-2018
ALL RIGHTS RESERVED**

CANDIDATE'S DECLARATION

I, VATSAL SANJAY, hereby certify that the work which is being presented in the dissertation entitled "**UNDERSTANDING OF MUTUAL INTERACTIONS BETWEEN LIQUID JETS: ENTRAINMENT AND SHEET FORMATION**" in partial fulfilment of the requirements for the award of the degree of "**INTEGRATED DUAL DEGREE**" in Mechanical Engineering with specialization in Thermal Engineering, submitted to the Department of Mechanical and Industrial Engineering in the Indian Institute of Technology Roorkee is an authentic record of my own work carried out under the supervision of Dr. Arup Kumar Das, Assistant Professor, Department of Mechanical and Industrial Engineering, Indian Institute of Technology Roorkee.

I have not submitted the matter embodied in this report for the award of any other degree or diploma.

Date: May 7, 2018

(VATSAL SANJAY)

Place: Roorkee

CERTIFICATION

This is to certify that the above statement made by the candidate is correct to the best of my knowledge and belief.

(Dr. ARUP KUMAR DAS)

Dedicated to

My Mentor,
&
My Parents

Acknowledgments

First of all, I would like to thank my mentor and guide, Dr. Arup Kumar Das for introducing me to the world of research. I still remember the first day when I walked into his office, with a desire to do contribute in the field of fire and fluid dynamics. He welcomed me, an undergraduate at that time, and guided me through the inception process. It has been 4 years since then, and there has been no turning back. His passion for science and willingness to explore new things have helped me throughout this journey. Working with Dr. Das has given me an extensive idea about the modeling of physical processes, develop theories to explain the physics and finally conduct experiments to confirm them. I have learned so many things from him, related to both, the subject and life in general. I always enjoy discussions and conversations with him. Thank you, sir, for your constant support and guidance.

I would also like to thank my parents and sister for their willingness to support me through higher studies. In a society where graduating from a college, and seeking job represent the norm, I am lucky to be born in a family which encourages higher education. Words cannot acknowledge the support I have received from them. Next, I would like to mention my friends, Rahul, Sonali, Prarthana, Aditya, Yagya, and Arpit. They have stood by me throughout my stay at IIT Roorkee. If it was left to me, I would have never gone out in the social world. Thank you for always pushing and helping me to develop a great work-life balance. I would be amiss if I do not mention the special contributions from my best friend, Akanksha. For every moment in the past five years, when my codes refused to work, when the results looked impossible, when the gyroscopic balance of life was disturbed, and through every tide, thanks a lot for always being there for me. There were days when I had burnt out the motivation. Thank you for re-igniting the spark.

My special gratitude to Anjali, who is the best partner one can hope to have, for her love and support. It is wonderful to have someone who is willing to patiently listen to all the technical jargon. There have been times when I have gotten new ideas from our discussions. This journey would have been difficult without your constant presence in my life. My warm hugs and a big thank you to you. A special acknowledgment to Akash, for being such a great critique of my works. and proofreading all my research publications without fail.

My past few years working in Two-Phase Flow & Instability Lab were really wonderful. I really liked the lab environment, my office room, my work, and my late night stay backs to finish works. I loved the place not just because of the work, but also because of the people around me. I would like to take this chance to thank my seniors and colleagues, Parmod Kumar and Saikat Datta, for their constant help in technical and non-technical aspects. Our

late night discussions on different topics of Fluid Mechanics and the workings of Gerris have always concluded with interesting insights. The enthusiasm we share for Physics is something I will cherish throughout my life. My sincere thanks to Digvijay Singh, Lokesh Rohilla, Dr. B. K. Rana, and all other members of the group for their constant support. I must also thank Sneha Malhotra for so many discussions we have had. I still maintain that theory is more important than applications. I would also like to mention my juniors, Sandeep, Anurag, Abhinav, and Mihir for their help with the work, and their dedication to the lab. I have been privileged to be surrounded by such curious people, who have taught me never to forgo the eagerness to learn new things. Along the same lines, I would also like to thank my high-school Physics teacher, Mr. Rohit Dewan for making me curious enough to explore the field.

I am grateful to Prof. J-P. Matas and Prof. J. J. Jerome, for giving an opportunity to work in their lab during the summers of 2016. It has been a great learning experience for me. The tricks and techniques related to post-processing of simulation data that I have learned there helped in the work I have presented here. The internship also strengthened my resolve to continue in the field of academia. I would like to express my sincere gratitude to Dr. K. M. Singh for motivating me throughout my stay. The way he taught the course on Computational Fluid Dynamics (CFD), which forms a major part of my research work, is unique and incredible. I would also like to thank all the faculty members of I.I.T. Roorkee, who taught me in the last five years, for keeping my interest in Fluid Dynamics alive. The fundamental courses on Thermodynamics by Dr. S. Dutta and Prof. R. P. Gakkhar, on Fluid Dynamics by Prof. B. K. Gandhi, on Modeling & Simulations by Dr. K. Murugesan, and on Heat & mass transfer by Prof. R. Kumar and Prof. A. Gupta have been vital for my work. In addition, the applied courses by Dr. A. Bansal, Dr. M. Mishra, and Dr. A. Kumar have made me realize the importance of Mechanical Engineering.

Last but not the least, I would like to express my deep recognition for IIT Roorkee, my alma mater. The quiet, lush green campus, the historical and magnificent main building, and the beautiful Ganges canal were always there when I needed a long walk to clear my head. Furthermore, I cannot thank enough the well-maintained Mahatma Gandhi Central Library (MGCL) for providing access to almost all internationally acclaimed journals. Finally, I acknowledge everyone who has been a part of my life for helping me, in one way or the other, through the course of this endeavor.

(VATSAL SANJAY)

Abstract

Interactions between two facing liquid jets and consequences of jet impingement onto a pool are studied using detailed numerical simulations and intelligent experimental investigations. The collision between liquid jets leads to the formation of a sheet in the median plane and is illustrated numerically. The sheet subsequently transforms into a chain like fluidic structure with successive dwarf links in mutually orthogonal planes. This structure is analyzed to pertain towards a steady state. Since the velocity of the sheet is super-critical (higher than the speed of the capillary waves), the first link is studied for the flow kinematics. To understand the behavior of fluid parcels inside the chain, flow is studied with streamlines. Their radial dispatch after the collision of jets is followed by self-similar paths with respect to the chain outer periphery. Further, a scaling law is presented for the variation of fluid velocity across the azimuthal direction of the flow. The influence of several non-dimensional parameters has been found on the shape of the first link of the chain. This has been generalized over the entire chain structure. For the understanding of chain profiles over a wide range of operating parameters, a correlation has been proposed based on numerical simulations and subsequent regression analysis. Citing analogy between the impact of jets for the formation of elemental links and traversal of non-deformable fluid quanta after the collision, an attempt has been made to understand the fundamental physics of this phenomenon through force balance. The analogy helps to take into account the role of surface tension and other forces on the shape and size of the liquid sheets. Further, the formation of higher order links is proposed as equivalent to the collision between the liquid rims bounding the sheet, modeled as the jets of reduced strengths and smaller impingement angles. Finally, the effects of various fluid properties on the dimensions of these links are assessed, illustrating the viscous dissipation at the time of collisions.

Furthermore, the air entrainment due to impingement of a water jet on a pool is studied extensively to understand the physics of the initiation and the cluster of bubbles formed below the free surface. Possible outcomes due to the jet impingement in a pool have been identified as smooth free surface without entrainment or formation of rigorous bubble cluster below the jet-pool contact. A triangular entrained region is found to be a three-dimensional association of disconnected bubble population continuously breaking and making with the neighbors. A correlation for prediction of maximum entrained height for a range of jet diameters and lengths is proposed. The trajectory of a single bubble is also studied to understand the kinematics of the bubble cluster. Alongside, an electrical conductivity probe has been used to examine the probabilistic presence of the bubble at a given depth in the liquid pool.

Contents

Abstract	vii
List of Figures	xi
List of Tables	xvi
Nomenclature	xvii
1 Introduction	1
1.1 Motivation and background	2
1.1.1 Jet - solid interactions	2
1.1.2 Jet - jet interactions	3
1.1.3 Jet - pool interactions	5
1.2 Literature Survey	6
1.2.1 Collision of liquid jets	6
1.2.2 Air entrainment by impingement of liquid jet on a pool	8
Experimental work	8
Numerical work	10
1.3 Lacuna in literature	10
1.3.1 Collision of liquid jets	10
1.3.2 Air entrainment by impingement of liquid jet on a pool	11
1.4 Objectives of the present work	12
1.4.1 Collision of liquid jets	12
1.4.2 Air entrainment by impingement of liquid jet on a pool	12
1.5 Organization of the thesis	12
2 Numerical Framework	14
2.1 Governing equations	15
2.2 Solution sequence of governing equations	16
2.2.1 Effective discretized governing equations	16
Hodge decomposition of velocity field	17
Calculation of surface tension force	17
2.2.2 Temporal discretization of governing equations	18
Calculation of projected velocity field, V_i^*	18

Pressure - Poisson equation	18
Pressure - velocity coupling	19
Surface tension correction	20
2.3 Summary	20
3 Collision of liquid jets	21
3.1 Introduction	22
3.2 Numerical model	22
3.2.1 Setup of the numerical model	23
3.2.2 Validation of the numerical code	26
3.3 Collision and sheet formation	27
3.3.1 The process of chain formation	28
3.3.2 Velocity variation inside the sheet	29
3.3.3 Three dimensional streamline structure	31
3.4 Parametric variation	34
3.4.1 Variation of control parameters	34
3.4.2 Prediction of chain structure using regression analysis	36
3.5 Analytical model	38
3.6 Inter-relation between inter-connected links	40
3.7 Summary	43
4 Air entrainment by impingement of liquid jet on a pool	45
4.1 Introduction	46
4.2 Experimental setup and methodology	46
4.3 Numerical model	49
4.3.1 Setup of the numerical model	49
4.3.2 Validation of the numerical code	53
4.4 Continuous and no entrainment	54
4.5 Onset of entrainment	55
4.5.1 Pinch-off of first annular bubble	56
4.5.2 Dynamics of first pinch-off	58
4.6 Dynamics of bubble cluster	59
4.6.1 Attainment of quasi-steady bubble cluster	59
4.6.2 Characterization of bubble cluster	60
4.6.3 Kinematics of the cluster centroid	63
4.7 Bubble kinematics	64
4.8 Summary	66

5 Conclusion and Scope of Future Work	68
5.1 Salient features and key findings	69
5.1.1 Collision of liquid jets	69
5.1.2 Air entrainment by impingement of liquid jet on a pool	70
5.2 Scope of future work	71
References	72
Publications	81

List of Figures

1.1	Liquid jets in everyday lives: (a) a typical jet with surface undulations, (b) liquid sprinkler showing different regimes of jet atomization, and (c) a jet of water falling onto a solid substrate.	3
1.2	(a) The consequences of collision of two liquid jets: a schematic and (b) a typical life of smooth liquid jet, freely falling under the influence of gravity. Both these configurations result in the formation of the liquid chain structure.	4
1.3	Illustration of the bubble entrainment by a single jet: (a) jet impingement and formation of cavity, (b) cavity growth and necking, and (c) pinch-off of first annular bubble and retracting cavity.	5
1.4	Entrainment inside a liquid pool. High inertia liquid jets lead to chaotic flow of entrained bubbles.	6
3.1	Formation of the liquid sheet by the collision of laminar jets. (a) Different structural features and length scales. (b) The primary link structure colored based on half times the magnitude of the sheet thickness, non-dimensionalized with the jet diameter $\left(\frac{h}{2d_j}\right)$.	23
3.2	Representation of the Adaptive Mesh Refinement (AMR) technique at critical locations across the fluid chain structure.	24
3.3	Mesh sensitivity analysis for a representative chain structure with the outer periphery and velocity profiles across several critical regions in the fluidic chain structure. The flow in these sheets are characterized by $(Fr, Bo, Re/Fr, \alpha) = (a) (2, 3.5, 1100, 60^\circ)$ and $(b) (2, 3.5, 35, 60^\circ)$	25
3.4	Illustration of the validation of numerical model undertaken by comparison of (a) numerical interface and (b) liquid flux variation with the azimuthal angle, θ . The numerically obtained results are superimposed with the respective experimental values obtained by Bush & Hasha (2004) .	27
3.5	Formation of the liquid chain due to the collision of laminar jets. The figure illustrates the transient period through the temporal advancement from (a) pre-collision symmetric jets to $T\left(\frac{u_j t}{d_j}\right) = (b) 1.5, (c) 4, (d) 5, (e) 5.5, (f) 6.5, (g) 8.5, (h) 14.5, (i) 18.5$ and (j) 20. The variation of d_1 and l_1 with time is shown in inset ($\alpha, Fr, Re/Fr, Bo = 30^\circ, 2.5, 34, 5$). The video for this figure is added as a supplementary material.	28

- 3.6 Flow kinematics of the fluid parcels: (a) velocity vector field for two representative cases, (b) variation of velocity in the radial direction for four representative cases and (c) their radially averaged sheet velocity ($u_s(\theta)$), non-dimensionalized with the average sheet velocity (u_0) along the azimuthal direction in the sheet. The parameters identifying the identity of the cases follow ($\alpha, Fr, Re/Fr, Bo$). 30
- 3.7 Three dimensional velocity field for $(\alpha, Fr, Re/Fr, Bo) = (30^\circ, 2, 1125, 3.4)$ with (a) XY plane streamlines, (b) velocity vector field in the YZ plane at different collision locations, (c) the three dimensional stable chain structure, (d) streamlines at maximum link widths in the YZ plane and (e) XZ plane streamlines. 32
- 3.8 Three dimensional streamlines embedded on the chain structure illustrating the twist incurred as they traverse through the region of subsequent collisions for $\alpha = 30^\circ, Fr = 2, Bo = 3.4$ and (a) $Re/Fr = 1750$ and (b) $Re/Fr = 34$. The figures in inset show the offset (δy from XZ plane and δz from XY plane) of the streamline at the extreme end of the chain structure as it moves downstream with the flow for the corresponding cases. 33
- 3.9 Variation of first link boundary with (a) α at $Fr = 2.5, Bo = 4.57$ and $Re/Fr = 34$ (b) Fr at $\alpha = 30^\circ, Bo = 3.4$ and $Re/Fr = 34$ (c) Bo at $\alpha = 30^\circ, Fr = 2.5$ and $Re/Fr = 34$ and (d) Re/Fr at $\alpha = 30^\circ, Fr = 2$ and $Bo = 3.4$. 35
- 3.10 High fidelity numerical simulations of liquid jets collision to form chain structure for variation of (a) α at $Fr = 2.5, Bo = 4.57$ and $Re/Fr = 34$ (b) Fr at $\alpha = 30^\circ, Bo = 3.4$ and $Re/Fr = 34$ (c) Bo at $\alpha = 30^\circ, Fr = 2.5$ and $Re/Fr = 34$ and (d) Re/Fr at $\alpha = 30^\circ, Fr = 2$ and $Bo = 3.4$. 36
- 3.11 Comparison between the values of expansion of the sheet outer periphery ($\Delta Z(x)$) as predicted from equation 3.10 and from numerical simulations for different test cases with (symbol, $\alpha, Fr, Bo, Re/Fr$) = ($\blacksquare, 30^\circ, 2.5, 5, 34$); ($+, 30^\circ, 2.5, 4, 34$); ($\blacklozenge, 30^\circ, 2.5, 2.3, 20$); ($\times, 25^\circ, 2.5, 4.57, 34$) and ($\bullet, 30^\circ, 2.5, 3.75, 20$). The first two inset figures (from the left) visualizes the corresponding three dimensional structure of the first link for the primary link and the third inset depicts the comparison between the equation 3.10 and the results of [Bush & Hasha \(2004\)](#). 37

- 3.12 Fluid quanta collision analogy: (a) schematic of the model and free-body diagram and comparison between the link shape obtained through numerical simulations and the fluid quantum trajectory (ζ , ■) for $(\alpha, Fr, Re/Fr, Bo) = (a) (30^\circ, 2.5, 34, 5)$, (b) $(30^\circ, 2.5, 23, 3.85)$, (d) $(30^\circ, 2, 34, 4.56)$ and (e) $(45^\circ, 2, 34, 3.4)$. 38
- 3.13 Inter-relation between links of chain reproduction of secondary link of Case 1 ($\alpha = 30^\circ, Fr = 2.5, Bo = 4, Re/Fr = 34$) as primary link of case 2 ($\alpha = 25^\circ, Fr = 2.2, Bo = 4, Re/Fr = 34$) and tertiary link of Case 1 as secondary link of Case 2 and primary link of case 3 ($\alpha = 11.25^\circ, Fr = 1.98, Bo = 4, Re/Fr = 34$) using (a) three dimensional chain structure and (b) two dimensional planar link locations. 41
- 3.14 Generalization of fluid rim collision for the higher order links with the prediction of angles of impingement for (a) secondary and (b) tertiary collisions and (c) the account of rim strength (Fr) in different links. 42
- 3.15 Evaluation of the dimensional characteristics of the secondary and tertiary links relative to the primary link, for variations of (a) α at $Fr = 2.5, Bo = 4.57$ and $Re/Fr = 34$ (b) Fr at $\alpha = 30^\circ, Bo = 3.4$ and $Re/Fr = 34$ (c) Bo at $\alpha = 30^\circ, Fr = 2.5$ and $Re/Fr = 34$ and (d) Re/Fr at $\alpha = 30^\circ, Fr = 2$ and $Bo = 3.4$. 43
- 4.1 (a) In house developed experimental setup for the study of entrainment process. The coordinate system has been defined using the Cartesian system centered at the point of impact of the jet on the pool. (b) Sequence of image processing applied for the characterization of the bubble cluster. 47
- 4.2 Signal behavior for different closure of circuitry. In case water closes the circuit the voltage signal is normal. However, with the presence of bubbles, an instantaneous dip can be observed 49
- 4.3 The computational domain with the implemented boundary conditions. 50
- 4.4 Determination of time taken for pinch off of first bubble after impact on the pool. The in-box figures represent instant of the pinch off. The $Fr_D Fr_L = 1.4$ and $Re = 8000$ are kept constant. Interfacial grids obtained by full Adaptive Mesh Refinement (AMR) are shown in the inset corresponding to case 2 with a relatively coarse grid as well as in case 5 and case 10 with fine grids. 52

- 4.5 (a) Schematic of the different locations where the velocity profile is plotted and compared. The phase boundary corresponds to that of case 6. (b) Velocity profile as observed at indicated locations. ($Fr_D Fr_L = 1.4$ and $T = \frac{V_j t}{d_j} = 2.5$) 52
- 4.6 (a) Experimental snapshot of the bubble cluster below the liquid pool with points of the interface obtained from numerical simulation (b) Numerically obtained bubble cluster at $Fr_D Fr_L = 1.4$; both experimental snap and numerical contours are plotted at $T = 300$ starting from jet touching the pool. 53
- 4.7 Comparison between experimental and numerically obtained results for temporal variation of (a) Velocity vector of a typical bubble in the entrained region at $Fr_D Fr_L = 1.8$ (b) Projected area of the entrained bubble cluster 54
- 4.8 Possible outcomes as the jet impinges onto the pool: (a) No entrainment $Fr_D Fr_L = 0.125$, (b) Continuous Entrainment with diverging converging cluster $Fr_D Fr_L = 1.25$ and (c) Continuous Entrainment with triangular entrainment region $Fr_D Fr_L = 3.8$ 55
- 4.9 The temporal record of the onset of entrainment; (left: experimental and right: numerical) (a) Jet impacts the liquid pool and forms a cavity at $T = \frac{V_j t}{d_j} = 1$, (b) Elongation of the cavity formed at $T = 1.95$, (c) Necking of the elongated cavity at $T = 2.5$ as surface tension force tries to overcome jet's inertia and (d) Pinch off of the first annular air bubble at $T = 3.5$. ($Fr_D Fr_L = 2.2$). 56
- 4.10 Experimental snapshots of pinch off for $Fr_D Fr_L = 1$ at $T =$ (a) 2.04, (b) 2.28, (c) 2.52, (d) 2.76, (e) 2.88, (f) 3, (g) 3.24, (h) 3.35, (i) 3.5, (j) 3.75, (k) 4, (l) 4.25, (m) 4.5, (n) 5, (o) 5.5 and (p) 6 57
- 4.11 (a) Depth of penetration of liquid cavity formed during the impact of jet onto the pool and subsequent collapse of cavity. (b) Streamlines developed around the formed cavity before (on left) and after (on right) pinch off. 58
- 4.12 Temporal variation of maximum depth of entrainment. The inset figure takes a closer look at the variation of the height of entrainment, which pertains to a nearly constant value. 59
- 4.13 Attainment of steady state entrainment height for $Fr_D Fr_L = 4$ with the interface colored by the depth as measured from the liquid pool interface at $T =$ (a) 85, (b) 90, (c) 95 and (d) 100 60
- 4.14 Steady entrainment pattern for $Fr_D Fr_L =$ (a) 1.4, (b) 2, (c) 3.25 and (d) 3.75 61

4.15 Steady state depth of entrainment as a function of the product of Froude numbers, $Fr_D Fr_L$; both experimental and numerical data points are mentioned.	62
4.16 Projected area of the region affected by entrained bubble cluster; plane is constructed by experimental observations and numerical data points are shown by symbols.	62
4.17 Temporal variation of the normalized abscissa of the centroid related to the entrainment cluster.	63
4.18 Variation of the acceleration of the centroid with its normalized abscissa related to the entrainment cluster.	64
4.19 Bubble trajectory in the entrained region at $Fr_D Fr_L = 1.8$, as obtained from experimental observation. The bubble inception occurs at the tip of the thin air sheath, traverses through the entrainment region, stops the downward motion as the buoyancy dominates its motion and erupts back at the free surface.	65
4.20 Characteristic probability density function of the experimental probe signals at different values of $Fr_D Fr_L$. More the peak is shifted towards the left, the high density of bubbles are present at the spatial location of the electrodes.	66

List of Tables

3.1	Performance data of the processors used for simulations to determine the refinement level in the Grid Independence Study. The simulations are done using four Intel Core i7-6500U CPU having clock speed of 2.5GHz each and 8 GB RAM.	26
3.2	Factors ($C_{m,n}$) involved in equation 3.11 determined by linear regression analysis to find the polynomial coefficients of equation 3.10.	37
4.1	Details of the physical properties of the tap water used in the experiments and the ambient air conditions.	48
4.2	Variation of different parameters associated with the flow. The Reynolds number and the product of Froude numbers are based on jet characteristics	48
4.3	Designation of cases considered for the grid sensitivity analysis.	51
4.4	CPU performance data for simulations done for the Grid Independence Study. The simulations are done using four Intel Core i7-6500U CPU having clock speed of 2.5GHz each and 8 GB RAM.	51

Nomenclature

α	Half of the impingement angle between liquid jets	rad
Δ	Length scale for interpolation of predicted velocity field	m
ΔZ	Rim to rim distance across the sheet	m
δl	Minimum size of the grid cell in octree system	m
δ_s	Dirac delta tensor, 1 for interface & 0 otherwise	—
δy	Streamline twist in the XZ plane	m
δz	Streamline twist in the XY plane	m
ζ	Trajectory of fluid quantum	m
θ	Azimuthal angle coordinate	rad
κ	Curvature of the interface	m^{-1}
μ	Fluid viscosity	Pas
σ	Surface tension coefficient	$N m^{-1}$
ρ	Fluid density	$kg m^{-3}$
ϕ	Angle of the tangent to fluid quantum trajectory from vertical	rad
Ψ	Volume fraction of the fluid	—
a_n	Acceleration of fluid quantum in normal direction	$m s^{-2}$
a_t	Acceleration of fluid quantum in tangential direction	$m s^{-2}$
Bo	Bond number associated with the working fluid	—
D_{ik}	Deformation tensor	s^{-1}
d_j	Diameter of liquid jet	m
d_s	Depth of bubble entrainment cluster inside the liquid pool	m
Fr	Froude number of the liquid jet	—
Fr_D	Diametrical Froude number	—
Fr_L	Longitudinal Froude number	—
f_n	Force of constant magnitude to mimic surface tension	N
g_i	Acceleration due to gravity	$m s^{-2}$
h	Thickness of the liquid sheet	m
l_j	Height of liquid jet inlet from the pool surface	m
m	Mass of the fluid quantum	kg
m_i	Normal unit vector for the liquid-gas interface	—
P	Pressure	Pa
$Q(\theta)$	Liquid volume flux inside the sheet	$m^3 s^{-1} rad^{-1}$

Re	Reynolds number of the liquid jet	—
r	Radial coordinate location	m
r_{max}	Maximum radial spread of the liquid sheet	m
T	Dimensionless inertial time	—
u_0	Sheet velocity	m s^{-1}
u_f	Local sheet velocity	m s^{-1}
u_n	Inlet velocity of the liquid jet as a function of jet radial distance	m s^{-1}
u_s	Averaged sheet velocity	m s^{-1}
V_i	Velocity vector field	m s^{-1}
V_i^n	Velocity vector field at time step n	m s^{-1}
V_i^*	Predicted velocity vector field at time step n	m s^{-1}
$V_i^{c,n}$	Cell centered velocity vector field at time step n	m s^{-1}
$V_i^{f,n}$	Face centered velocity vector field at time step n	m s^{-1}
x_i	Spatial vector dimension	m

Chapter 1

Introduction

1.1 Motivation and background

Liquid jets are ubiquitous in nature. [Eggers & Villermaux \(2008\)](#) defines jets as “a stream of particles having more or less columnar shape”. Liquid jets are affected by different kinematic (such as flow field in jet and surrounding medium) and physical properties (such as density and viscosity of the liquid and the surrounding medium, as well as the interfacial surface tension). Therefore, fundamentally, they form a unique system in which the influence of these properties on the dynamics of flow will be quite interesting to study. Not surprisingly, liquid jets have sought the attention of the researchers from the very inception of scientific curiosity ([Da Vinci 1508](#)). A quick look across the literature reveals an abundance of work in the field of surface undulations ([Driessen et al. 2014](#); [Lord Rayleigh 1879, 1889](#)), jet atomization ([Ling et al. 2015](#); [Matas & Cartellier 2013](#); [Matas et al. 2011](#); [Yang & Turan 2017](#)), interactions of liquid jets ([Bremond & Villermaux 2006](#); [Bush & Hasha 2004](#); [Ibrahim & Przekwas 1991](#); [Koralek et al. 2018](#)), multiphase entrainment ([Biń 1993](#); [Kersten et al. 2003](#); [Kiger & Duncan 2012](#); [Sande & Smith 1976](#)), and other topics investigating jets as means of heat and mass transfer ([Kate et al. 2007](#); [Martin 1977](#)). The study of surface undulations is germane to describe the instabilities, especially the Rayleigh-Plateau instability ([Hoeve et al. 2010](#)), which leads to the formation of thin liquid threads and droplets ([Baek & Han 2017](#)). Figure 1.1(a) shows a typical liquid jet encountered in daily life. One can notice the surface undulations on an otherwise smooth jet. These perturbations are enhanced in time, because of increase in inertia of jet or by the influence of surrounding medium, and leads to atomization process as Figure 1.1(b). Liquid jet atomization finds its application in numerous industrial processes, such as the fuel injection system in the combustion engine and sprinklers. Further, the interaction of liquid jets has invoked the curiosity of researchers, eminent even in the scientific artworks by [Da Vinci \(1508\)](#). The theoretical and experimental analysis accounting for different types of interactions involving liquid jets is classically summarized in a recent effort by [Eggers & Villermaux \(2008\)](#). Depending on the complementary member, these interactions can be classified into three categories. Next, an overview of these interactions is provided.

1.1.1 Jet - solid interactions

Figure 1.1(c) shows a liquid jet impingement onto a solid surface, and accompanying hydraulic jump. This configuration has several aesthetic and industrial consequences. One everyday example can be observed in the classically studied hydraulic jump in kitchen sink ([Eggers & Villermaux 2008](#)). With respect to industries, liquid jet impingement is used

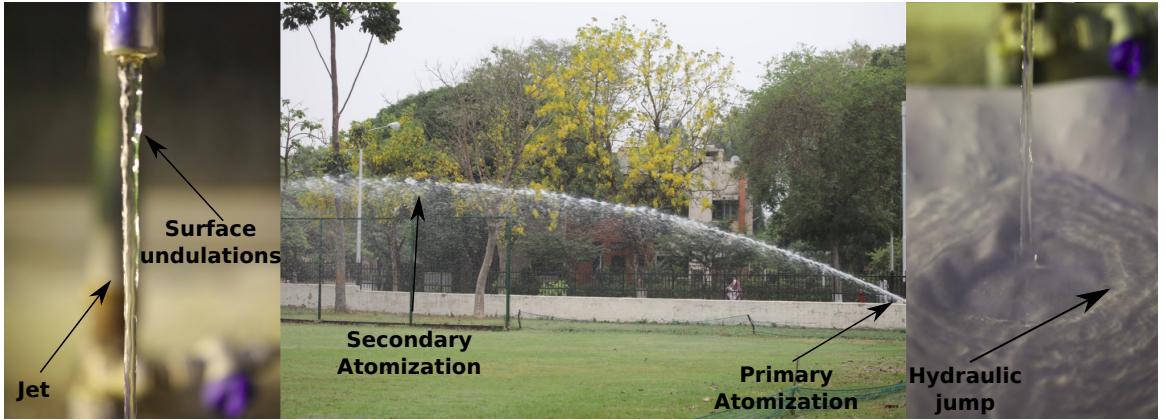


FIGURE 1.1: Liquid jets in everyday lives: (a) a typical jet with surface undulations, (b) liquid sprinkler showing different regimes of jet atomization, and (c) a jet of water falling onto a solid substrate.

for achievement of high heat transfer coefficients for cooling of turbine blades, electronic equipment and pistons ([Bergles & Ma 1983](#); [Chen et al. 2018](#)), water jet machining, and metal processing. Recently, building on the innovative works of [Kate et al. \(2007\)](#), [Singh & Das \(2018\)](#) presented an extensive investigation of the accompanying hydraulic jump during such impingements. In case of a vertical impingement, the liquid sheet spreads radially, and symmetric jump is observed whereas, in case of an oblique impingement, the asymmetric jump can be obtained. The interplay between wall-adhered outward flow and back-flow from the downstream of the sheet determines the physics governing formation and stability of these hydraulic jumps.

1.1.2 Jet - jet interactions

Most elemental among the interactions of liquid jets is the collision between two identical jets. This configuration is one of the canonical configurations for generation of liquid sheets ([Wadhwa et al. 2013](#)). It gives way to atomized droplets in high inertial regime ([Bremond & Villermaux 2006](#)). If the strengths of the two jets are identical, the liquid sheet is formed, as a planar one, in the median plane, ie., mid-way between the jets at the point of collision ([Bush & Hasha 2004](#)). This configuration is usually employed in the afterburners of the aircraft or in the thrust engines used in rockets ([Chen et al. 2013](#)) and has advantages over the conventional coaxial liquid-gas jet atomization technique because of the improved inertial driven destabilization and mixing between jets ([Erni & Elabbadi 2013](#)). Moreover, the droplets formed in this process come from the thin sheet, making the droplet size distribution skewed towards the lower size and more evenly spread ([Inoue et al. 2008, 2009](#)) as compared to the droplets formed from the single jet atomization as the latter are ejected

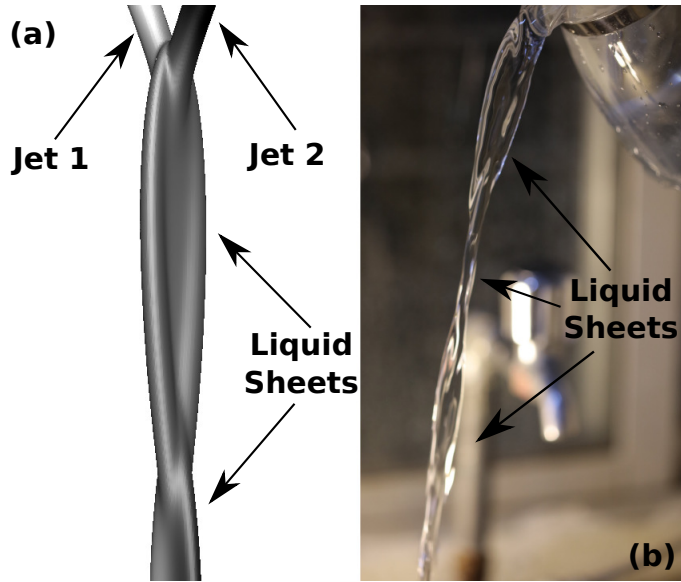


FIGURE 1.2: (a) The consequences of collision of two liquid jets: a schematic and (b) a typical life of smooth liquid jet, freely falling under the influence of gravity. Both these configurations result in the formation of the liquid chain structure.

from a thick liquid jet core instead of a thin sheet. This aids in the post-atomization combustion process ([Lhuissier & Villermaux 2011](#)). The collision of laminar jets to form stable sheets is the fundamental case of such atomization processes and also holds physical significance for the exploration of physics behind atomization. Moreover, these structures can be used as wall-free continuous reactors ([Erni & Elabbadi 2013](#)) as well. Recently, [Koralek et al. \(2018\)](#) demonstrated the generation of the free-flowing sheet with the thickness in the order of few nanometers. These sheets can be used for Infra-Red, X-ray and even electron spectroscopy.

At low velocities or narrow angles of impingement, jets may coalesce to form a unified one or they may bounce off due to the presence of a thin film of air between them ([Wadhwa et al. 2013](#)). On increasing the flow rates, laminar jets may lead to the formation of a stable liquid sheet bounded by the thicker rims at the periphery ([Yang et al. 2014](#)). The inertial and the gravitational forces act to expand the liquid sheet formed, but the action of surface tension helps the sheet to converge so that the successive collisions of the thick rims downstream of the flow result in the formation of mutually orthogonal liquid sheets ([Bush & Hasha 2004](#)). Figure 1.2(a) illustrates this structure termed as the liquid chain with the complementary orthogonal sheets forming the different links. A similar structure can also be observed when a liquid sheet falls under the influence of gravity. The sheet has minimum thickness at the center, whereas at the periphery, by virtue of surface tension, thicker rims are present. These rims undergo collision to form subsequent sheets. A

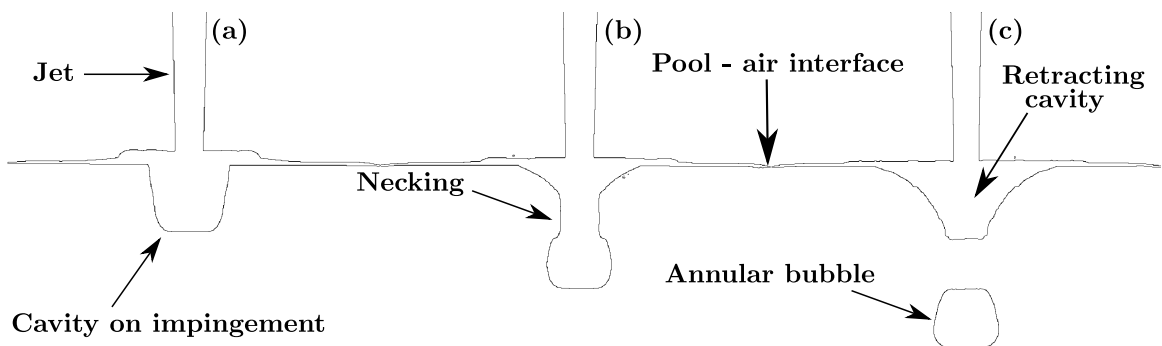


FIGURE 1.3: Illustration of the bubble entrainment by a single jet: (a) jet impingement and formation of cavity, (b) cavity growth and necking, and (c) pinch-off of first annular bubble and retracting cavity.

daily life example could be pouring out of water from jet as illustrated in Figure 1.2(b). It must be noted that for these interactions, the liquid jet must be small enough to allow Rayleigh-Plateau instabilities to kick in ([Eggers & Villermaux 2008](#)).

1.1.3 Jet - pool interactions

Entrainment inside a pool, beneath a plunging liquid jet, plays a favorable role in aeration process of chemical reactors ([Biń 1993](#)). A look around reveals the presence of this phenomenon in everyday life, ranging from filling of a glass of water using tap to several industrial processes. The plunging jet configuration is often used in wastewater treatment plants ([Donk et al. 1979](#)) and have several other industrial applications, like gas-liquid mixing and reactions ([McKeogh & Ervine 1981](#)) and operation of jet propulsion vehicles (navy vessels) ([Deshpande et al. 2012](#)). It can also be used in several oxygenation processes, especially in fish-keeping. However, the air bubbles can be detrimental in processes like casting, causing a reduction in strength of the resultant mold. It is of utmost importance to understand the process of entrainment before controlling it, either in favorable or opposing direction. The critical velocity of the liquid jet for the inception of entrainment depends on the dimensions of the jet ([Chanson et al. 2004; Lin & Donnelly 1966](#)) and the disturbances present on its surface ([Sene 1988](#)). Figure 1.3 illustrates the process of air-entrainment initiation. Near inception, flow conditions have been revealed by [Cummings & Chanson \(1998, 1999\)](#) as symmetric cylindrical air-entry about the centerline of the vertical jet ([Roy et al. 2013](#)) (Figure 1.3(a)). Air entry as unified mass is restricted by surface tension causing pinch off of bubbles (Figure 1.3(b)). After the pinch-off occurs, the cavity retracts back to the pool surface and this cycle repeats for continued entrainment ([Roy et al. 2013](#)) (Figure 1.3(c)). The continuous pinch-off pertains towards a statistically steady

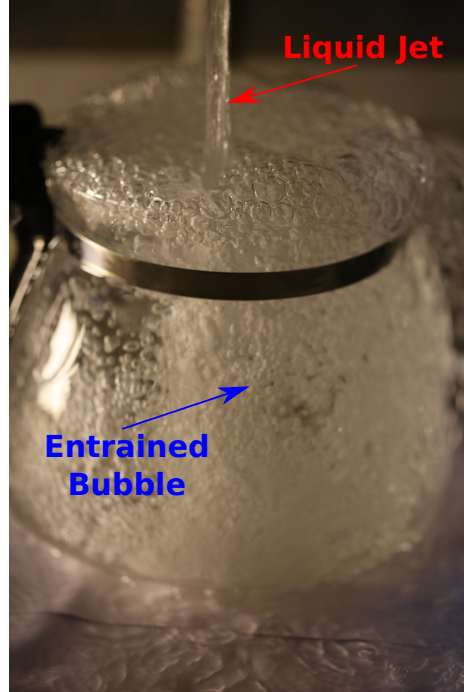


FIGURE 1.4: Entrainment inside a liquid pool. High inertia liquid jets lead to chaotic flow of entrained bubbles.

state and this bubble population behaves like a single cluster whose characteristics play a crucial role in two-phase chemical reactors (Bagatur 2014; Chanson & Cummings 1994; Clanet & Lasheras 1997; Harby et al. 2014). Some recent studies by Ma et al. (2011, 2012) have revealed the critical role of velocity gradient at the impinging interface. They have also analyzed the void fraction and bubble count inside the liquid pool. At very high inertia of liquid jets, the bubble cluster become chaotic. One such situation is depicted in Figure 1.4.

1.2 Literature Survey

In the present work, liquid jet interactions of types described in sections 1.1.2 and 1.1.3 are thoroughly investigated. Therefore, in this section, the literature pertaining to these two studies is discussed.

1.2.1 Collision of liquid jets

Lord Rayleigh (1879, 1889) was probably the first researcher to formally study the chain-like structures. He reported that the chain structure was generated because of the undulations formed at the surface of a single elliptical liquid jet. Unlike cylindrical jets, they do

not have an axis of overall symmetry. This results in thickening of the jet at the periphery (similar to Figure 1.2(b)) leading to the formation of the chain-like structure due to the impact of these rims.

[Taylor \(1960\)](#) formulated an impingement theory for impact of liquid jets to form a fluid sheet at the median plane, mid-way between the jets. Prior to his work, only the inertial and gravitational forces were considered to describe the phenomenon which gave an expanding liquid sheet. He realized that the flow inside the thicker rim at the periphery can be sustained only if the surface tension force provides the necessary centripetal acceleration to the fluid parcels inside the rim. The velocity field in the rim is also accelerating due to loss of gravitational potential. On balancing the inertial and surface tension forces, [Taylor \(1960\)](#) proposed an expression for the sheet radius, given by $r_{max} = \rho u_0 Q(\theta) / (2\sigma)$ (where, u_0 denotes the average sheet velocity assumed constant throughout including the rim, $Q(\theta)$ implies liquid flux distribution inside the sheet and ρ, σ are the fluid density and its surface tension coefficient with the air, respectively).

[Ibrahim & Przekwas \(1991\)](#) demonstrated that the stable sheet structures can serve as the base case for the atomization studies because the droplets are formed from the perturbed liquid sheet. At high viscosities, different flow instabilities die down but at higher inertial strengths, as the flow becomes turbulent, the flapping atomization takes place.

[Clanet & Villermaux \(2002\)](#) and [Villermaux & Clanet \(2002\)](#) discussed the instabilities inside the liquid sheet. As the velocity exceeds a critical value, the Kelvin-Helmholtz instability takes over and results in formation of destabilizing waves. This also speeds up the process of fingering instabilities at the peripheral rim of the sheet.

[Bush & Hasha \(2004\)](#) worked on the classical formulation proposed by [Taylor \(1960\)](#) and gave a comprehensive theoretical and experimental theory for collision of liquid jets. They introduced several regimes to characterize the different flow structures obtained from such collisions and gave an exhaustive experimental analysis of the stable liquid chain formed by the collision of laminar jets. Their work also verifies the formulation given by [Taylor \(1960\)](#) which predicts the sheet dimensions within experimental precision. Emphasis has been also given by [Bush & Hasha \(2004\)](#) for prediction of shapes of leaf-like links forming chain structure. We have used the results developed by them to validate our numerical model.

[Bremond & Villermaux \(2006\)](#) studied the several instability modes related to the rim at the periphery of the sheet. These instabilities are magnified as the velocity of fluid parcels inside the rims increase and the curvature dependent surface tension forces are not able to maintain equilibrium. First, finger-like projections are observed at the rims' outer boundaries causing Plateau-Rayleigh instability and droplet generation.

[Choo & Kang \(2001, 2002, 2007\)](#) have worked extensively on the characterization of the first link of the chain structure, including the velocity field inside. Contrary to the earlier belief, they have shown that the sheet velocity is not a constant parameter but varies with the azimuthal angle variation. This has been demonstrated in our studies as well. Moreover, they have also discussed the variation in the sheet characteristics with respect to the velocity profile at the exit of the nozzles, inside the jets. They prescribe that a parabolic profile gives a better estimate for the fully developed laminar jet as compared to the uniform profile or any other power law fit. Further, they gave the justification for the presence of thicker liquid rim at the periphery using Particle Image Velocimetry (PIV) technique. The radial streamlines were observed near the point of impingement and the fluid parcels travel towards the periphery resulting in the formation of the thick rim due to fluid accumulation. [Chen et al. \(2013\)](#) have shown the formation of liquid chain using Finite Volume based Volume of Fluid (VOF) framework. They attempted the reproduction of different flow regimes as proposed by [Bush & Hasha \(2004\)](#). The same numerical framework is used in the present method with some modifications on the mesh refinement criteria.

[Inamura & Shirota \(2014\)](#) studied the presence of stagnation point inside the liquid sheet. Unlike the head-on collision of liquid jets where this point is at the intersection of the jets, it was found to shift upstream by some factor. The factor was found to be dependent on the impingement angle. These works summarize the variation of fluid velocity inside the sheet.

[Yang et al. \(2014\)](#) discussed the influence of different flow parameters on the shape and size of the first link in the chain structure. They acknowledged the variations due to physical parameters as well. In the present study, their arguments are generalized for the entire chain structure.

[Da et al. \(2016\)](#) also demonstrated the formation of liquid chain using Boundary Element Method (BEM). This simulation work comprises of inviscid flow assumption but gives mesmerizing fluid structures. They have successfully reproduced all the regimes observed in the experimental works but fail to acknowledge the internal dynamics of the liquid sheet.

1.2.2 Air entrainment by impingement of liquid jet on a pool

Experimental work

[Biń \(1993\)](#) gave an extensive review of all the theoretical and experimental work present at that time. The compiled works include description of entrainment mechanism, conditions for its onset, details of entrained cluster and empirical formulas for associated mass

transfer. The review paper also consisted a detailed description of two-dimensional jet impingement (Goldring et al. 1980; Sene 1988).

Evans et al. (1996) identified that the gas entrainment rate depends on the effective diameter of the free jet at the plunge point and the annular film thickness adjacent to the surface of the jet. The works of El Hammoumi et al. (2002), McKeogh & Ervine (1981), and V. Donk (1981) recorded the air concentration profiles and velocity distribution in the fully developed flows. The authors targeted the global measurements of air entrainment.

Chanson (1996) explained the mechanism of air entrainment with the help of an advection-diffusion model, resulting in a diverging entrainment cone. The region of pool surrounding the intersection of jet and pool acts as the source of bubble inception. Inside the pool, as the buoyancy balances the downward flow of bubbles, they start moving upwards. Depending on the inertia of incoming jet, either a converging-diverging or a diverging overall cluster is formed.

Clanet & Lasheras (1997) reported some experiments conducted with round plunging jets that reveal interesting results concerning the depth of penetration of the bubble cluster under a wide range of jet diameters, velocities and plunging angles.

Cummings & Chanson (1999) studied extensively the effects of velocity on the air entrainment phenomenon and its quantity along with coalescence and breaking of individual bubbles.

Chanson et al. (2004) investigated air entrainment and bubble dispersion in the developing vertical circular plunging jets and came up with some remarkable results and expressed a requirement to study the air-water velocity distribution and turbulent velocity fluctuations. Soh et al. (2005) gave an analytical approach to the problem. They have related the maximum height of the air void with the properties of water jet using the energy balance method. However, the method is too idealized, neglecting the losses and simplification of geometry. The theory seems to be in good agreement with the experimental results only for low diametrical Froude numbers ($Fr_D < 10$, where, $Fr_D = \frac{V_j}{\sqrt{gd_j}}$) with an error as high as 50% for $Fr_D > 50$.

Efforts are also being noticed to understand the physics of entrainment using numerical approach. Qu et al. (2011) published a combined experimental and numerical investigation. They studied the mixture approach against the level-set method for flow modeling. Since, this phenomenon rigorously involves the consideration of interface and its deformations with time, level-set approach has an edge over the mixture approach.

Numerical work

Zhu et al. (2000) studied the mechanism of air entrainment due to surface roughness. However, the work involves numerical simulations only up to the impact and pinch off point. Recent study complies with the proposed air cavity formation reported in the above paper. Kersten et al. (2003) examined the spread of falling liquid over the receiving pool, formation of cavity and eventual pinch off. The initial bubble that pinches off after the closure of cavity and the air sheath around the submerged jet can be designated as the source of bubbles inside the pool. Recently, comprehensive research has been carried out on further characterization of different parameters related to entrainment (Bagatur 2014; Belden et al. 2012; Harby et al. 2014). Several researchers have mentioned the requirement for the study of influence of the controlling parameters, such as jet length and the velocity on penetration depth and entrainment volume (Qu et al. 2013). Roy et al. (2013) examined descriptively the trajectory of a single bubble in the entrainment region.

Durve & Patwardhan (2012) outlined the onset of gas entrainment through numerical simulations. It can be easily established that over the past couple of decades, the main focus has been to explore the mechanism of the entrainment process.

Kiger & Duncan (2012) highlighted the role of air-entrainment for two distinct systems. The first included a standard configuration of single liquid jet impinged onto a stationary pool, and the other comprised on plunging horizontal waves. In an extensive review of available literature, the authors have investigated the flow inception conditions and given insights into the more complex, breaking wave entrainment. The surface vortices have been found to be an important aspect in this regard. Deshpande & Trujillo (2013) studied the distinguishing features of the shallow angle plunging jets using VOF methodology. However, the work deals with inclined jets and till the pinch off moment for vertical jets.

Brouilliot & Lubin (2013) reported remarkable compliance of numerical and experimental results with classical VOF-PLIC method. At the same time limitations of this method to account for inclusions smaller than the mesh grid size can be observed.

1.3 Lacuna in literature

1.3.1 Collision of liquid jets

Critical assessment of literature reveals that an in-depth study of fluid chain regime is still due which can explore fundamental physics behind the formation of primary link and establish a relation between successive diminishing links. Moreover, most of the analytical

or empirical models, used to describe the flow, need input from the experiments to close the system of equations prior to obtaining any solution ([Bush & Hasha 2004](#)). The work in the direction of numerical simulation to obtain such structures is few as per the knowledge of the author ([Chen et al. 2013; Da et al. 2016](#)). A major challenge that lies in the prediction of the chain-like structure is the proper resolution of the sheet (approximately $1/100^{th}$ of jet diameter) between the rims, which are supposed to mingle once again for forming next link in a mutually perpendicular plane. [Chen et al. \(2013\)](#) have demonstrated the presence of a diversity of length scales in such a simplistic fluid link. If the grid resolution is not sufficient, occurrence of numerical pinch-off is observed, whereby non-physical holes are created inside the sheet because of the lack of cells. The works of [Da et al. \(2016\)](#) do give satisfactorily result in this regard but, their exhibition of chain-like structure along with other physical jet related structures is limited to inviscid fluids. The inability of their numerical model to incorporate viscosity has led to inaccuracies in the study of chain structure along with its kinematics and dynamics.

1.3.2 Air entrainment by impingement of liquid jet on a pool

Most of the theoretical works prior to the review by [Biń \(1993\)](#) included two-dimensional plunging liquid jet. However, from an industrial point of view, three dimensional jets are more important since they are easy to achieve and widely studied by researchers. Nevertheless, there have been only a few studies on the flow fields just below the impingements. Most of the works revolve around what [Bonetto & Lahey \(1993\)](#) termed as the global measurements. Undoubtedly these studies are important to have a control over the process and may allow correlation of the onset of air-carry under criteria. However, very little or no information is provided about the kinematics and dynamics of the entrained bubbles and the resultant dispersion of the submerged jet. Even though this process is so common in nature, the mechanism involved is not well understood. Entrainment characteristics need to be related with flow rate, jet diameter and length of jet for better understanding. Irrespective of such attempts at development of correlations, as argued by [Sande & Smith \(1976\)](#), a lack of generality is observed (discrepancies of the order of 3 or more). It has been observed that the parameters proposed by one investigator is off by noticeable amount when compared to data from others. Furthermore, the literature still lacks an exhaustive account for the analysis of bubble life cycle during entrainment. Moreover, there have been very little work on the characterization of the region affected in the liquid.

1.4 Objectives of the present work

1.4.1 Collision of liquid jets

- To understand the formation of fluid chain through a series of temporal snapshots leading to the formation of a steady structure after initial transients.
- To study the overall behavior of the fluid chain while focusing on the physics of flow for the primary link by analyzing the dimensional characteristics and velocity fields.
- To generalize the overall behavior of the fluid chain structure from the characteristics of the first link.
- To model the collision of liquid jets in a manner analogous to the impact of discrete non-deformable fluid parcels (hereinafter referred as fluid quanta or particles).
- To analyze the formation of higher order links as a result of the collision of rims of the preceding links.

1.4.2 Air entrainment by impingement of liquid jet on a pool

- To understand the formation of air cavity and subsequent pinch off details along with fragmentation of the initial bubble into smaller bubbles.
- To characterize the cluster of bubbles and the region of entrainment in the liquid pool.
- To study dynamic behavior of the interface cluster and observe the variation in shape with time starting from the point of inception of entrainment.
- To investigate the kinematics and dynamics of bubble lifecycle, commencing at the time of entrainment to its trajectory inside and outside the bubble cluster to the instance when it erupts at the water surface.
- To develop a conductivity probe in order to obtain strength of entrainment at different flow rates.

1.5 Organization of the thesis

The current work is undertaken to understand the fundamental physics behind two important jet interactions categories, namely, collision of liquid jets to form chain and impingement of jet onto a pool to initiate entrainment. The present chapter summarizes the work

available in the literature, and the scope of improvement. The following chapter includes the description of the mathematical model, as both the topics involve detailed numerical simulations. Chapter 3 represents the results corresponding to the collision of laminar smooth liquid jets. At first, a series of transient features are studied to reach a steady state structure. We have Special attention is given to the second and third collisions, leading to the formation of the subsequent mutually orthogonal links. The flow kinematics are studied based on the velocity field inside the sheet. The impact of fluid quanta is then used to model the behavior of fluid parcels inside the sheet. Post-collision, the effect of surface and viscous forces is included with a constant magnitude force, which is always perpendicular to the trajectory of individual fluid quantum. This helps to understand the dynamics of liquid sheet formation. The second important aspect of our work is to generalize the impingement model for the entire chain structure, taking into account the reduced strength of rims that collide to form the subsequent perpendicular links.

Furthermore, chapter 4 consists of the results for impingement of liquid jet onto a pool surface. It is a combined experimental and numerical study to understand the process of entrainment inception and subsequent cluster formation. Different modes of entrainment are discussed followed by study of the onset of entrainment. The life cycle of first annular bubble, from the time of inception, is investigated in detail. Furthermore, the association of air bubbles formed by the fragmentation of first annular bubble and continued entrainment results in formation of a cluster. This has been treated as an individual system, and different kinematic and dynamic features are discussed. At last, a conductivity probe is used to investigate the bubble kinematics.

Chapter 2

Numerical Framework

In the present work, a three-dimensional finite volume framework is employed for numerical simulations. An open source freeware, transient, multi-fluid, Navier-Stokes solver Gerris is used. Developed by Popinet (2003, 2009), Gerris has provided a stable and accurate platform for surface tension inclusive flows. It has been successful used frequently by researchers, such as Chen et al. (2013) and Kumar et al. (2016, 2017a,b), to delve into similar problems in interfacial flows involving liquid sheets (Fuster et al. 2013; Zhang & Wang 2017), jet (Xie et al. 2017; Yang & Turan 2017) and thin features like ligaments and films (Agbaglah et al. 2015; Walls et al. 2015) to capture intricate flow details and investigate the process. In this chapter, the detailed numerical framework adopted by Gerris is given. First, the governing equations are presented followed with a discussion on the discretization schemes along with the step-by-step sequence of the solution procedure implemented.

2.1 Governing equations

Conventional mass and momentum conservation equations for incompressible flow have been solved in presence of the surface tension and gravitational force. Equation 2.1 contains the mass conservation equation for incompressible flow, which simply states that the velocity field ($V_i = V_1\hat{i} + V_2\hat{j} + V_3\hat{k}$) must be divergence free.

$$\frac{\partial V_i}{\partial x_i} = 0 \quad (2.1)$$

The momentum equation for the incompressible Newtonian fluids that is solved for all the spatial coordinates can be summarized as given in equation 2.2. In the equation, the forces applied on the control volume chosen consist of the pressure in form of its gradient $\left(\frac{\partial P}{\partial x_i}\right)$, the volume specific body force due to gravitation (ρg_i), the surface forces due to shear stress ($2\mu D_{ik}$, where μ represents the coefficient of dynamic viscosity and D_{ik} is the deformation tensor) and the interface specific surface tension force ($\sigma\kappa$, where σ is the surface tension coefficient and κ denotes the curvature of the interface).

$$\rho \left(\frac{\partial V_i}{\partial t} + V_k \frac{\partial V_i}{\partial x_k} \right) = - \frac{\partial P}{\partial x_i} + \frac{\partial (2\mu D_{ik})}{\partial x_k} + \sigma\kappa\delta_s m_i + \rho g_i \quad (2.2)$$

Moreover, the surface tension term is multiplied with the Dirac distribution function (δ_s) to ensure that the force due to surface tension acts only at the interface having a normal vector m_i . Further, the deformation tensor D_{ik} is defined using the symmetric part of the velocity

field gradient as given in equation 2.3.

$$D_{ik} = \frac{1}{2} \left(\frac{\partial V_i}{\partial x_k} + \frac{\partial V_k}{\partial x_i} \right) \quad (2.3)$$

The equation 2.2 implicitly takes care of the mechanical energy. Moreover, the temperature variations are too small to affect the phenomenon being investigated and therefore, no thermal energy equation is considered. The interface tracking is done using the Volume Of Fluid (VOF), a front capturing approach involving volume fraction of liquid, defined as $\Psi(x_i, t)$, at the spatial and temporal instance of x_i and t respectively. The density and viscosity for the study can be described using equation 2.4 in terms of a generic property A .

$$A(\Psi) = \Psi A_1 + (1 - \Psi) A_2 \quad \forall A \in \{\rho, \mu\} \quad (2.4)$$

The VOF approach is implemented in a two-step process of interface reconstruction (based on the values of Ψ and piecewise linear interface construction scheme, PLIC) along with geometric flux computation and interface advection, shown in equation 2.5.

$$\frac{\partial \Psi}{\partial t} + \frac{\partial(\Psi V_i)}{\partial X_i} = 0 \quad (2.5)$$

2.2 Solution sequence of governing equations

In this section, a brief discussion about the solution scheme is presented. The details of this procedure can be found in the work of [Popinet \(2003, 2009\)](#).

2.2.1 Effective discretized governing equations

$$\rho^{n+1/2} \left(\frac{V_i^{n+1} - V_i^n}{\delta t} + \left(V_k \frac{\partial V_i}{\partial x_k} \right)^{n+1/2} \right) = - \left(\frac{\partial P}{\partial x_i} \right)^{n+1/2} + \frac{\partial}{\partial x_k} (\mu^{n+1/2} (D_{ik}^n + D_{ik}^{n+1})) + (\sigma \kappa \delta_s m_i)^{n+1/2} + \rho g_i \quad (2.6)$$

$$\frac{\Psi^{n+1/2} - \Psi^{n-1/2}}{\delta t} + \frac{\partial(\Psi^n V_i^n)}{\partial X_i} = 0 \quad (2.7)$$

$$\frac{\partial V_i^n}{\partial x_i} = 0 \quad (2.8)$$

Equations 2.6 to 2.8 consist of the effective discretization employed in the Gerris. It uses second-order accurate time discretization of momentum and continuity equations with time

splitting algorithm as proposed by Chorin (1968), whereby an unconditionally stable corrector predictor time marching approach is adopted. A multigrid solver is used for the solution of the resulting pressure-velocity coupled Poisson equation. The advection term of the momentum equation $\left(V_k \frac{\partial V_i}{\partial X_k}\right)$ is estimated using the Bell-Colella-Glaz second-order unsplit upwind scheme (Bell et al. 1989), which requires the restriction to be set up on the time step. Following Popinet (2009), time step has been determined to satisfy Courant-Friedrich-Lowy (CFL) stability criteria of less than unity.

Hodge decomposition of velocity field

Equation 2.6 involves solution of both velocity and pressure fields. Further, as seen from equation 2.6 and 2.7, a couple of interesting things can be realized. Firstly, solution to both velocity and pressure field is required. Since, the flow is assumed incompressible, the only instance of pressure comes in equation 2.6. This is done by making the use of Hodge decomposition, according to which, the velocity field can be written as a sum of a divergence free, and an irrotational component as given in equation 2.9. This also helps in the time-splitting projection method for solution of Navier-Stokes equations (Chorin 1968).

$$V_i^* = V_i + \frac{\partial \psi}{\partial x_i} \quad \forall \epsilon_{ijk} \frac{\partial}{\partial x_j} \left(\frac{\partial \psi}{\partial x_k} \right) = 0 \quad (2.9)$$

In the control volume, the velocity field needs to be divergence free. On using this fact, the above equation is modified as equation 2.10 (Popinet 2009).

$$\frac{\partial V_i^*}{\partial x_i} = \frac{\partial^2 \psi}{\partial x_i^2} \quad (2.10)$$

Calculation of surface tension force

An important feature in the governing equations of two-phase flow processes is the inclusion of interfacial focused surface tension. The influence of this surface force is included as a source term in equation 2.2. The Dirac distribution tensor, δ_s ensures that the effect is only accounted for the interface between two fluids. Applying the Brackbill et al. (1992) approximation of surface tension, one can obtain:

$$\sigma \kappa \delta_s m_i \approx \sigma \kappa \frac{\partial \Psi}{\partial x_i} \quad (2.11)$$

The curvature term associated with the above equation can be given by:

$$\kappa = \frac{\partial m_i}{\partial x_i} \quad \forall \quad m_i = \frac{\frac{\partial \Psi}{\partial x_i}}{\sqrt{\frac{\partial \Psi}{\partial x_i} \frac{\partial \Psi}{\partial x_i}}} \quad (2.12)$$

Calculation of the curvature, κ forms an integral part of the two-phase flow solver. [Popinet \(2009\)](#) describes the approach adopted in Gerris.

2.2.2 Temporal discretization of governing equations

A second order accurate, unconditionally stable predictor-corrector (projection) scheme is used in Gerris for solution methodology ([Chorin 1968](#)). Here, a step-by-step sequence of the solution procedure, at each time step, is provided.

Calculation of projected velocity field, V_i^*

$$\rho^{n+1/2} \left(\frac{V_i^* - V_i^n}{\delta t} + \left(V_k \frac{\partial V_i}{\partial x_k} \right)^{n+1/2} \right) = \frac{\partial}{\partial x_k} (\mu^{n+1/2} (D_{ik}^n + D_{ik}^*)) + (\sigma \kappa \delta_s m_i)^{n+1/2} + \rho g_i \quad (2.13)$$

At first, a projected velocity field, V_i^* is calculated using the above equation. It is interesting to note the presence of fractional time step variables, such as density field ($\rho^{n+1/2}$), advection term $\left(V_k \frac{\partial V_i}{\partial x_k} \right)^{n+1/2}$, viscosity ($\mu^{n+1/2}$) and surface tension force $(\sigma \kappa \delta_s m_i)^{n+1/2}$ in equation 2.13. Out of these, the advection term is approximated using method proposed by [Bell et al. \(1989\)](#) and surface tension is modeled using proposition of [Brackbill et al. \(1992\)](#) described in Section 2.2.1. Moreover, the properties, like density and viscosity, are modeled using the solution obtained from equations 2.7 and 2.5. With these approximations, the equation 2.13 can be used to obtain the projected velocity field, V_i^* . Furthermore, it must be noted that the effect of pressure is not considered in this calculation and will be used later on to find divergence free velocity field.

Pressure - Poisson equation

Including the effect of pressure in the velocity field, the following equation for momentum balance is obtained:

$$V_i^{n+1} = V_i^* - \frac{\delta t}{\rho^{n+1/2}} \left(\frac{\partial P}{\partial x_i} \right)^{n+1/2} \quad (2.14)$$

Here, V_i^{n+1} must represent the divergence free velocity field in order to satisfy the continuity equation, given in temporal form as:

$$\frac{\partial V_i}{\partial x_i}^{n+1} = 0 \quad (2.15)$$

Using, equations 2.14 and 2.15, the following pressure - velocity Poisson equation is obtained:

$$\frac{\partial}{\partial x_i} \left(\frac{\delta t}{\rho^{n+1/2}} \left(\frac{\partial P}{\partial x_i} \right)^{n+1/2} \right) = \frac{\partial V_i}{\partial x_i}^* \quad (2.16)$$

This Poisson equation is solved using iterative Gauss - Seidel iterative method with a relaxation operator ([Popinet 2003](#)). The solution is carried out on a quadtree (two-dimensional) or an octree (three-dimensional) based multilevel solver. The outcome of this solution step is to obtain a pressure field at fractional time step.

Pressure - velocity coupling

Once projected velocity (V_i^*) and pressure ($P^{n+1/2}$) fields are known, the velocity field can be calculated using equation 2.14. However, Gerris uses collocated grid which is known to suffer from lack of pressure - velocity coupling. This may lead to pressure oscillations. In order to solve this issue, following corrections in the velocity field are implemented:

$$\frac{\partial V_i}{\partial x_i}^* = \frac{1}{\Delta} \sum_f \delta_{ij} V_i^{f,*} m_j \quad (2.17)$$

$$V_i^{f,n+1} = V_i^{f,*} - \frac{\delta t}{\rho^{n+1/2}} \left(\frac{\partial^f P}{\partial x_i} \right)^{n+1/2} \quad (2.18)$$

$$V_i^{c,n+1} = V_i^{c,*} - \left\langle \frac{\delta t}{\rho^{n+1/2}} \left(\frac{\partial^f P}{\partial x_i} \right)^{n+1/2} \right\rangle^c \quad (2.19)$$

Equation 2.17 is used to find out the face centered projections of the velocity field ($V_i^{f,*}$) using linear interpolations. As mentioned earlier, the pressure field is calculated from equation 2.16. Using these two fields, the face centered ($V_i^{f,n+1}$) and cell centered ($V_i^{c,n+1}$) velocity fields are corrected. The face centered velocity, $V_i^{f,n+1}$, is used in calculation of the flux across the faces of individual cells. This is also used in estimation of the advection term as suggested by [Bell et al. \(1989\)](#). Additionally, it must be noted that the operator $\langle \rangle^c$ represents averaging across all the faces.

Surface tension correction

In Section 2.2.1, the [Brackbill et al. \(1992\)](#) approximation is elucidated. Following the momentum equation formulations of [Francois et al. \(2006\)](#) and [Renardy & Renardy \(2002\)](#) along with the above approximation, equation 2.20 is obtained.

$$-\left(\frac{\partial P}{\partial x_i}\right)^{n+1/2} + \sigma\kappa\frac{\partial\Psi^{n+1/2}}{\partial x_i} = 0 \quad (2.20)$$

An equilibrium discretized solution for the above equation is given by $P^{n+1/2} = \sigma\kappa\Psi^{n+1/2} + C$, where C is a constant. Using this and employing implementations identical to equations 2.18 and 2.19, the predicted face centered ($V_i^{f,*}$) and cell centered ($V_i^{c,*}$) velocities are corrected by using following equations:

$$V_i^{f,*} \leftarrow V_i^{f,*} + \frac{\delta t\sigma\kappa^{f,n+1/2}}{\rho\Psi^{f,n+1/2}} \frac{\partial^f}{\partial x_i} (\Psi)^{n+1/2} \quad (2.21)$$

$$V_i^{c,*} \leftarrow V_i^{c,*} + \left\langle \frac{\delta t\sigma\kappa^{f,n+1/2}}{\rho\Psi^{f,n+1/2}} \frac{\partial^f}{\partial x_i} (\Psi)^{n+1/2} \right\rangle^c \quad (2.22)$$

Another important feature of the VOF methodology for interfacial flow, implemented by Gerris, is the reconstruction of the interface using Piecewise Linear Interface Construction (PLIC). This is needed for the precise treatment of the interface dynamics.

2.3 Summary

This section serves as a precursor to the problem specific numerical model setups provided in the individual chapters. A detailed description of the governing equations is provided at the beginning, followed by a solution sequence of the discretized system of equations. Numerical schemes associated with the various components of momentum equation is mentioned along with the step-by-step solution procedure. Several important corrections, related to solution of checker-board problem and surface tension calculations, germane to the two-phase flow solutions, are also described. Further details of the solution methodology and implementation can be found in work of [Popinet \(2003, 2009\)](#).

Chapter 3

Collision of liquid jets*

*The results presented in this chapter are published in: Sanjay, V and Das, A. K. (2017). “Formation of liquid chain by collision of two laminar jets”. Physics of Fluids, 29.11, pp. 112101. DOI : 10.1063/1.4998288.

3.1 Introduction

The collision between two liquid jets has been studied in this present chapter. Numerical simulations illustrate the formation of mutually orthogonal link-like sheets which on the whole give rise to the chain structure (as depicted in Figure 3.1 (a)). Working on the classical formulations, chain structure has been identified by [Bush & Hasha \(2004\)](#), who introduced several regimes to characterize the different flow structures obtained from the collision of liquid jets. Earlier, similar structures generated because of the undulations on the surface of a single elliptical liquid jet were reported by [Lord Rayleigh \(1879, 1889\)](#). Although the method described in these works results in the formation of liquid chains where thin orthogonal sheets are observed, the collision of laminar liquid jets is also used as a canonical configuration for generation of liquid sheet ([Bush & Hasha 2004](#)). Moreover, a similar setup is also used in wall-free continuous chemical reactors ([Erni & Elabbadi 2013](#)). Therefore, a study has been made to understand the overall behavior of the fluid chain while the focus has been kept on the physics of flow for the primary link by analyzing the dimensional characteristics and velocity fields. Special attention is given to the second and third collisions, leading to the formation of the subsequent mutually orthogonal links. The collision of liquid jets is modeled in a manner analogous to the collision of discrete non-deformable fluid parcels (hereinafter referred as fluid quanta or particles). Post-collision, the effect of surface and viscous forces is included with a constant magnitude force, which is always perpendicular to the trajectory of individual fluid quantum. This helps to understand the dynamics of liquid sheet formation. The second important aspect of present work is to generalize the impingement model for the entire chain structure, taking into account the reduced strength of rims that collide to form the subsequent perpendicular links.

3.2 Numerical model

A freeware code, Gerris ([Popinet 2003, 2009](#)) has been used to study the collision between two liquid jets, and subsequent formation of the sheet. Over the years, several independent researchers have utilized and verified the capabilities of Gerris to investigate phenomena involving liquid jets ([Duchemin et al. 2002; Fuster et al. 2013; Yang & Turan 2017](#)) as well as fluid-fluid ([Chen et al. 2013; Zhang & Wang 2017](#)) and fluid-solid impingements ([Jian et al. 2018; Visser et al. 2015](#)). Therefore, Gerris has been used to carry out simulations specified in this study.

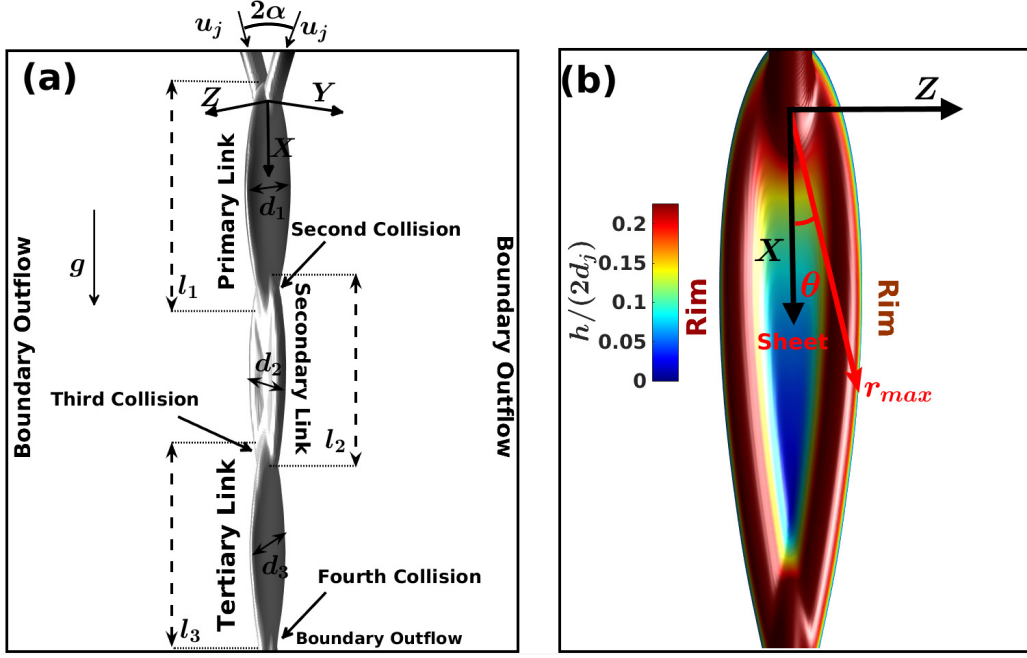


FIGURE 3.1: Formation of the liquid sheet by the collision of laminar jets. (a) Different structural features and length scales. (b) The primary link structure colored based on half times the magnitude of the sheet thickness, non-dimensionalized with the jet diameter $\left(\frac{h}{2d_j}\right)$.

3.2.1 Setup of the numerical model

The computational domain has also illustrated in Figure 3.1 (a) with parabolic inflow (equation 3.1 as suggested by Choo & Kang (2007)) of jets (diameter, d_j and impingement angle, 2α) and boundary outflow, elsewhere. In equation 3.1, u_n is the inlet velocity, u_j is the average velocity, r is the radial location in the jet from its centerline and d_j is the jet diameter.

$$\frac{u_n}{u_j} = 2 \left(1 - \left(\frac{2r}{d_j} \right)^2 \right) \quad (3.1)$$

Following the problem description, one can easily see that the different features of the liquid sheets can be represented in terms of the kinematic and dynamic properties, such as jet velocity (u_j), its diameter (d_j), angle of impingement (2α), acceleration due to gravity (g) and other physical properties such as the density of the fluid (ρ), its viscosity (μ) and the coefficient of surface tension (σ) at the fluid-air interface. On performing non-dimensional analysis, it can be observed that Froude number $\left(Fr = \frac{u_j}{\sqrt{gd_j}} \right)$, Bond number $\left(Bo = \frac{\rho g d_j^2}{\sigma} \right)$ and ratio between Reynolds number and jet Froude number $\left(Re/Fr = \frac{\rho \sqrt{gd_j^3}}{\mu} \right)$ govern

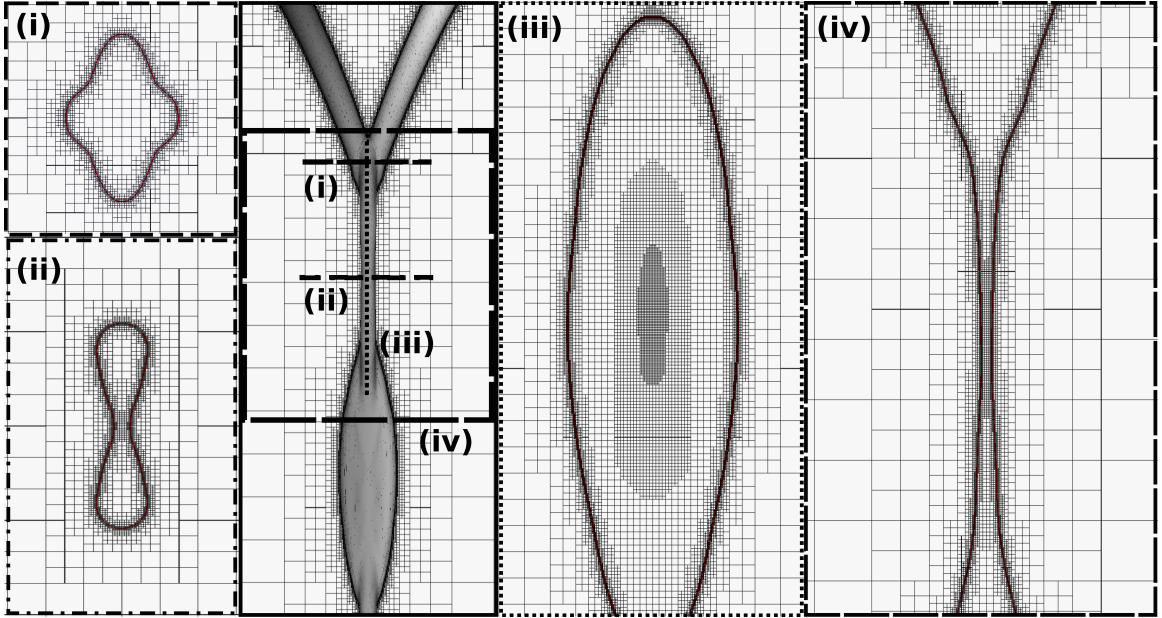


FIGURE 3.2: Representation of the Adaptive Mesh Refinement (AMR) technique at critical locations across the fluid chain structure.

the shape and sizes of different links in the fluid chain structure.

As identified from the literature ([Chen et al. 2013; Zhang & Wang 2017](#)), a major challenge that lies in the prediction of the chain-like structure is the proper resolution of the sheet (approximately $1/100^{\text{th}}$ of jet diameter) between the rims, which are supposed to mingle once again for forming next link in a mutually perpendicular plane. Figure 3.1 (b) demonstrates the presence of a diversity of length scales in such a simplistic fluid link and hence, the spatial discretization of the domain is undertaken using an octree-based structured hierarchical grid system, locally refined near the interface. It is necessary to capture the smallest features of the flow, in this case, the thickness of the liquid sheet. The multi-level grid structure adapts itself according to the gradient of the volume of fluid scalar field, Φ , which implies that the structured octree mesh is finest at the interface between the two fluids. This refinement is illustrated in Figure 3.2. It shows the mesh structure around different critical regions of the chain. [Choo & Kang \(2001\)](#) and [Hasson & Peck \(1964\)](#) have shown that the thickness of the liquid sheet can be given by the equation 3.2. This expression has been found to describe the thickness of the liquid sheet within experimental precision by several independent researchers ([Choo & Kang 2001; Ekimova et al. 2015; Shen & Poulikakos 1998](#)).

$$\frac{hr}{d_j^2} = \frac{1}{4} \frac{\sin^2 \alpha}{(1 - \cos \theta \cos \alpha)^2} \quad (3.2)$$

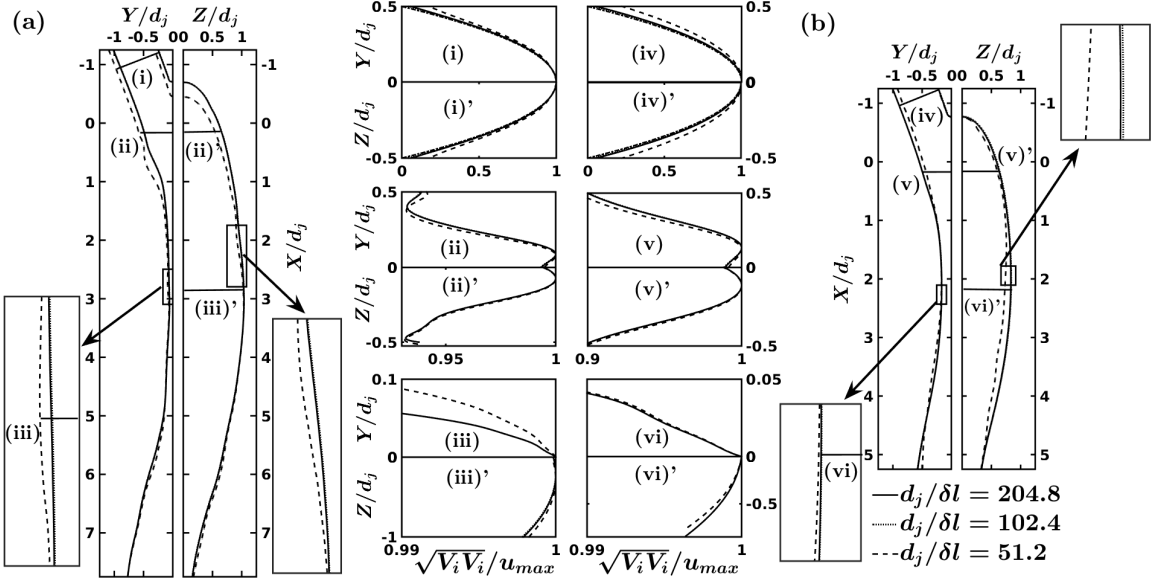


FIGURE 3.3: Mesh sensitivity analysis for a representative chain structure with the outer periphery and velocity profiles across several critical regions in the fluidic chain structure. The flow in these sheets are characterized by $(Fr, Bo, Re/Fr, \alpha) = (a) (2, 3.5, 1100, 60^\circ)$ and $(b) (2, 3.5, 35, 60^\circ)$

Here, r is the radial direction originating from the collision point of the jets and h is the measurement of the thickness of the film produced. Even though minima of equation 3.2 occurs at $\theta \rightarrow \pi$, it must be noted that the decrement in thickness is more prominent because of the increase in radial distance downstream of the first collision point ($h \propto \frac{1}{r}$). Further, it can also be shown that the thickness of liquid sheet follows:

$$\frac{hr}{d_j^2} \sim 1 \quad \forall \quad 2\alpha \in \{0, \pi/2\} \quad (3.3)$$

In order to select the minimum cell size, we have maintained the condition given in equation 3.4, where (δl) denotes the minimum size of the octree grid system. It must be noted that the expression is taken only as an initial guide for grid selection, and an extensive Grid Independence Study (GIS) is performed thereafter to finally select the minimum cell size.

$$\frac{d_j}{\delta l} \sim 10 \frac{r_{max}}{d_j} \quad (3.4)$$

The factor of 10 is included to have at least 10 grid points (Ling et al. 2015) across the smallest length scale for the structure to avoid numerical breakage of the sheet (Chen et al. 2013). To obtain good liquid film resolution, δl is varied to match the above-mentioned criteria. As representative simulations, we show the effect of variation of δl , in Figure 3.3,

TABLE 3.1: Performance data of the processors used for simulations to determine the refinement level in the Grid Independence Study. The simulations are done using four Intel Core i7-6500U CPU having clock speed of 2.5GHz each and 8 GB RAM.

$\left(\frac{d_j}{\delta l}\right)_{max}$	$\left(\frac{t_{CPU}}{t_{actual}}\right)$ (days/s)
51.2	~ 20
102.4	~ 28
204.8	~ 60

on the sheet profile and velocity pattern at different locations of the impinging jets and the resultant primary link. It can be observed that at $\frac{d_j}{\delta l} = 102.4$, well resolved film is obtained with acceptable computational cost ($\sim 50\%$ less than $\frac{d_j}{\delta l} = 204.8$). The results from this mesh sensitivity analysis have been summarized in Table 3.1. In the next section, the validation of the employed numerical method is demonstrated.

3.2.2 Validation of the numerical code

To check the accuracy of the developed mesh structure and the mathematical model, results from simulations are compared with experimental observations of [Bush & Hasha \(2004\)](#). Figure 3.4 presents a description of the results in this test. The one-to-one correspondence between the experimental sheet profile ([Bush & Hasha 2004](#)) and the numerical results is reported in Figure 3.4 (a). Making use of the fact that their experiments led to supercritical (greater than capillary wave speed) sheet speeds, [Bush & Hasha \(2004\)](#) were able to construct the variation of liquid volume flux ($Q(\theta)$) inside the sheet by scanning across the sheet and collecting liquid through a fine opening (as given by equation 3.5). Here u_n denotes the fluid parcel velocity perpendicular to the differential element across which the flux is calculated, r is the radial location of the element and h is the corresponding thickness of the sheet at that location.

$$Q(\theta) = \frac{dQ}{d\theta} = u_n h r \quad (3.5)$$

In order to get quantitative validation, the variation of liquid volume flux ($Q(\theta)$) inside the sheet is also plotted in Figure 3.4 (b) along with [Bush & Hasha \(2004\)](#). Matching between present numerical simulations and pioneering experimental results by [Bush & Hasha \(2004\)](#) provides confidence for the numerical understanding of the phenomenon, in present work. Furthermore, the accuracy also implies attainment of supercritical sheet velocities and hence a given link of the fluidic chain structure can be studied without worrying

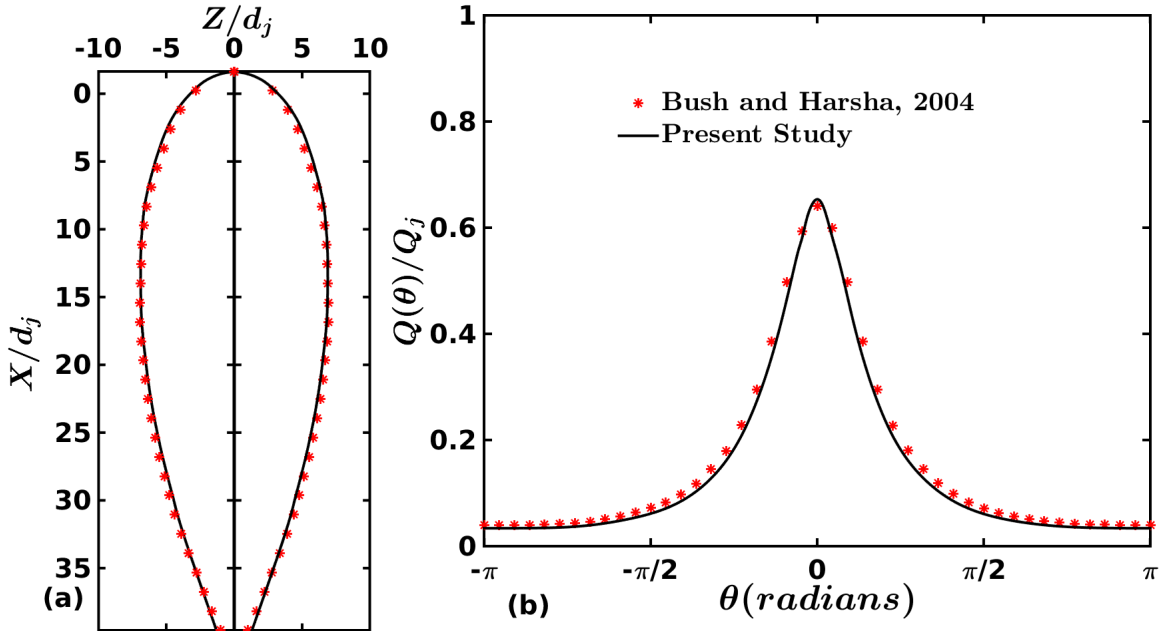


FIGURE 3.4: Illustration of the validation of numerical model undertaken by comparison of (a) numerical interface and (b) liquid flux variation with the azimuthal angle, θ . The numerically obtained results are superimposed with the respective experimental values obtained by [Bush & Hasha \(2004\)](#).

about the conditions downstream of the flow. In the next section, results of the numerical simulation using the presented model to study the collision of liquid jets are mentioned.

3.3 Collision and sheet formation

As the laminar liquid jets collide, a thin sheet bounded by thicker rims is formed in the median plane, perpendicular to the axes of the jets, whereas the formation of subsequent links is attributed to the collision of thicker rims formed in the preceding stage. The initialization of the liquid jets is done using small inclined cylinders with circular cross-sections. The geometric equation for this is given in equation 3.6 and the initialized jets are illustrated in Figure 3.5 (a).

$$\frac{|(\mathbf{x} - \mathbf{x}_1) \times (\mathbf{x} - \mathbf{x}_2)|}{|\mathbf{x}_2 - \mathbf{x}_1|} = \frac{d_j}{2} \quad (3.6)$$

Here, \mathbf{x} is the loci of the cylinder with axis marked by the vector $\mathbf{x}_2 - \mathbf{x}_1$ and d_j is the diameter of the cylinder. Across this inclined cylinder, a parabolic velocity profile is patched as discussed in section 3.2. In this section, the formation of chain structure due to the collision of liquid jets is discussed and the temporal variation of the same is illustrated. This is followed by the study of the kinematics of fluid parcels inside the liquid sheet. At last,

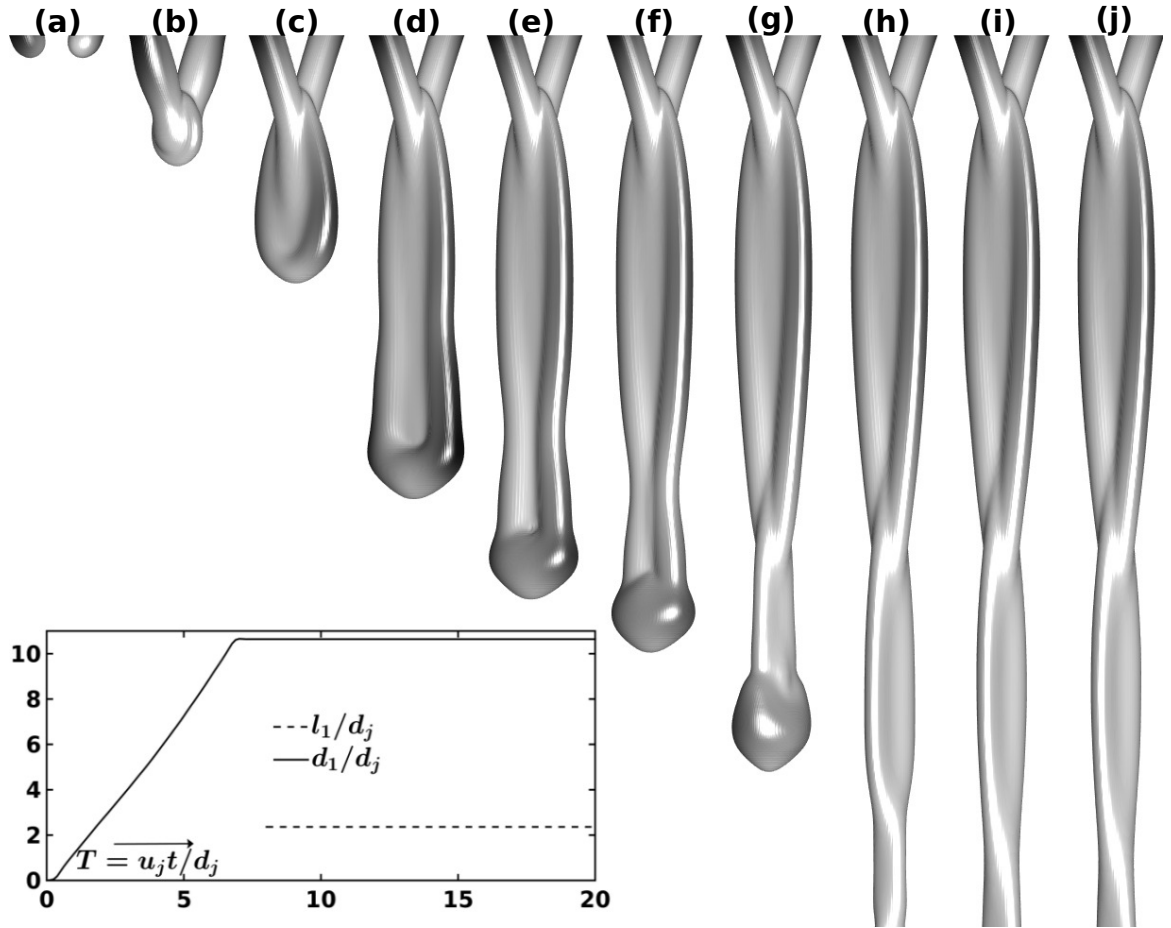


FIGURE 3.5: Formation of the liquid chain due to the collision of laminar jets. The figure illustrates the transient period through the temporal advancement from (a) pre-collision symmetric jets to $T(\frac{u_j t}{d_j}) =$ (b) 1.5, (c) 4, (d) 5, (e) 5.5, (f) 6.5, (g) 8.5, (h) 14.5, (i) 18.5 and (j) 20. The variation of d_1 and l_1 with time is shown in inset ($\alpha, Fr, Re/Fr, Bo = 30^\circ, 2.5, 34, 5$). The video for this figure is added as a supplementary material.

the three-dimensional streamline structure, showing the characteristic twists, is discussed. This is germane to understand the flow field inside the liquid chain. The three-dimensional streamline also generalizes the kinematics of fluid parcels through various converging (impingement) - diverging (sheet formation) regions.

3.3.1 The process of chain formation

Figure 3.5 shows temporal evolution of the fluid sheet when the two jets (shown in Figure 3.5 (a)) collide. The reference for temporal variations is kept at the instant when the jets collide. The fluid parcels are dispatched radially outwards from the point of impingement. In case of the head-on collision of the liquid jets ($\alpha = 90^\circ$), the sheet formed is always

radial in the absence of gravity (Eggers & Villermaux 2008) and the point of stagnation is in-line with the two liquid jets (Inamura & Shirota 2014). However, in this case, the net inertia of jets and gravity result in a bay leaf like sheet as shown in Figures 3.5 (b) and 3.5 (c). Present zone of consideration lies in $0.5 < Fr < 4$, where gravity plays a major role unlike Bremond & Villermaux (2006) and Bush & Hasha (2004). In absence of surface tension or at very high Weber number, the sheet keeps on expanding (figures 3.5 (d) and 3.5 (e)), leading to the formation of the open rim structures (Chen et al. 2013; Taylor 1960). However, due to the action of the surface tension, the sheet stops expanding and the two rims are formed at the periphery because of the accumulation of the fluid parcels from the liquid sheet. Surface tension also provides the necessary centripetal acceleration to sustain the liquid rims. These rims undergo a second oblique collision (Figure 3.5 (f)) at an angle smaller than the initial collision (Figure 3.5 (b)). After the secondary impingement, similar to Figure 3.5 (c), a flow biased sheet begins to develop (Figure 3.5 (g)). However, unlike the primary link, this is formed in the plane parallel to the incoming jets, and orthogonal to the preceding link. Formation of this second link has no effect on the characteristic features of the primary link as the sheet speed is supercritical (Bush & Hasha 2004), and therefore can be independently studied.

Temporal advancement results in the formation of a full-fledged secondary link as shown in figures 3.5 (h) to 3.5 (j). It must be noted that the plane of formation of this sheet is orthogonal to that of the primary link and therefore the secondary link shares the same plane as the axes of the jets. The process continues and a series of mutually orthogonal links are obtained, successively reducing in size until a long single liquid jet is formed (Bush & Hasha 2004). After the initial transients, as seen from Figure 3.5 and its inset, the links become steady (non-dimensionalized time, $T \left(\frac{u_j t}{d_j} \right) = 8.5$ as representation in primary link), which have been analyzed further.

3.3.2 Velocity variation inside the sheet

Jets progress towards each other and collide at a point in the median plane to form a sheet bounded by leaf-like rims. Fast moving thin sheet possess radial velocity pattern emerging from a stagnation point (δ_π higher than the impingement location). Inamura & Shirota (2014) have established $\delta_\pi = \lambda d_j / (2 \sin \alpha)$, where the factor λ is a function of the impingement angle. It needs to be noted that δ_π changes its value, depending upon the angle of impingement and can be taken as a parameter. Considering δ_π and velocity vectors, obtained from numerical simulations for two sets of non-dimensional numbers, flow pattern inside the sheet is reported in Figure 3.6 (a). It can be observed that velocity vectors follow a self-similar smooth path, as traced by sheet boundary. An increase of sheet span

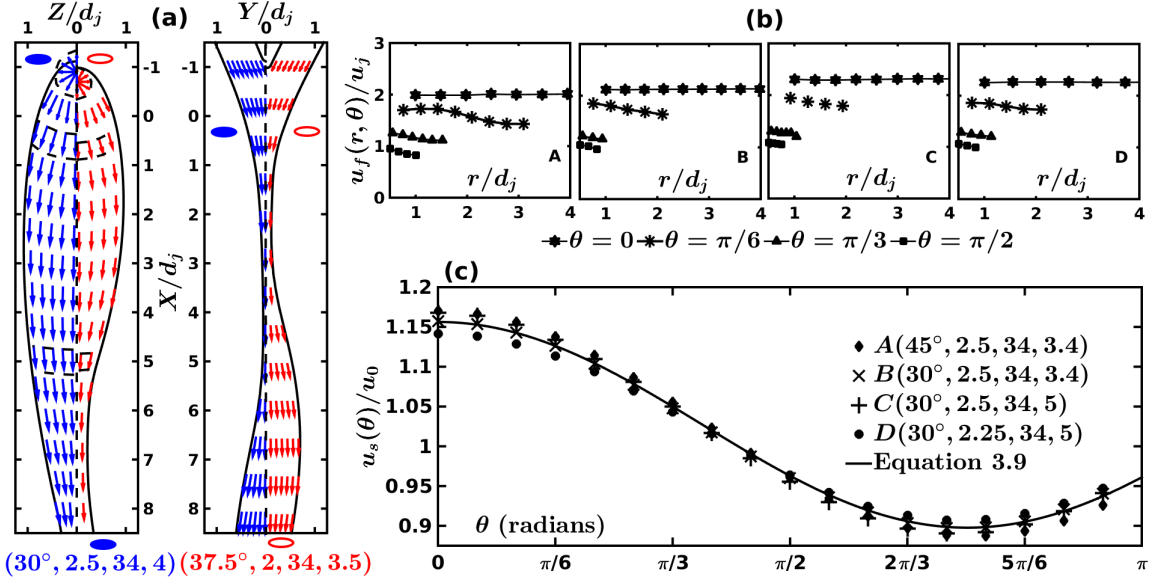


FIGURE 3.6: Flow kinematics of the fluid parcels: (a) velocity vector field for two representative cases, (b) variation of velocity in the radial direction for four representative cases and (c) their radially averaged sheet velocity ($u_s(\theta)$), non-dimensionalized with the average sheet velocity (u_0) along the azimuthal direction in the sheet. The parameters identifying the identity of the cases follow ($\alpha, Fr, Re/Fr, Bo$).

can be also noticed from the figure for a higher velocity of impacting jets.

An effort has been made to observe the local sheet velocity ($u_f(r, \theta)$) at a given radial and azimuthal point. The local sheet velocity ($u_f(r, \theta)$) (first used by Choo & Kang (2002)) denotes the steady average flow across the thickness of the sheet. Moreover, Figure 3.6 (a) shows the presence of both radial and azimuthal components of the velocity vectors. Therefore, the local sheet velocity ($u_f(r, \theta)$) can be expressed as equation 3.7, where Y is the coordinate direction parallel to link's thickness.

$$u_f(r, \theta) = \int_0^1 \sqrt{V_i V_i} d(Y/h) \quad (3.7)$$

V_i denotes the velocity field in Cartesian-tensor notation and $\sqrt{V_i V_i}$ is the total magnitude of the velocity given by $\sqrt{V_r^2 + V_\theta^2 + V_z^2}$. Azimuthal and radial velocities are considered here to accommodate spread of fluid streams which form chain and subsequent links in orthogonal planes. The variation of the local sheet velocity ($u_f(r, \theta)$) along radial plane at different azimuthal angles have been shown in Figure 3.6 (b). It can be observed that the order of change in the fluid velocity across the radial distance from the point of impact is less than the change across the azimuthal direction (also discussed by Choo & Kang (2002)). Making use of this feature, the sheet velocity ($u_s(\theta)$) in a particular azimuthal direction

has been also obtained by integrating the local sheet velocity, $u_f(r, \theta)$, as given by equation 3.8. ($u_s(\theta)$) gives a measure of the velocity of dispatch of fluid parcel in a given azimuthal direction.

$$u_s(\theta) = \int_0^1 u_f(r, \theta) d\left(\frac{r}{r_{max}(\theta)}\right) \quad (3.8)$$

It must be noted that $r_{max}(\theta)$ is the maximum radial spread of the liquid sheet in a particular azimuthal direction (θ). Upon non-dimensionalization of sheet velocity with its average ($u_0 = \int_0^\pi u_s(\theta) d\theta$), a self-similar behavior in azimuthal direction is observed and reported in Figure 3.6 (c) for a wide diversity of non-dimensional parameters. In this figure, four arbitrarily chosen parameters are shown which adhere to a functional relationship of $u_s(\theta)$ in the following fashion:

$$\frac{u_s(\theta)}{u_0} = 1.03 + 0.13 \cos\left(\frac{4.18\theta}{\pi}\right) \quad (3.9)$$

It needs to be noted that the equation 3.9 is valid for a large range of non-dimensional numbers explored in the present study, forming stable chain structure ($0^\circ < \alpha \leq 45^\circ$, $Fr \sim 1$, $Bo \sim 1$ and $10 \leq Re \leq 2300$). Using Figure 3.6 and equation 3.9, it can be realized that the thickness-averaged velocity field in equation 3.7 is a function of only one coordinate X and the functional dependence on coordinates r, θ is only through their combination $X = r \cos \theta$. Further, the integration in equation 3.8 over the radial direction is equivalent to the integral of function of local sheet velocity (u_f) over the interval $X \in \{0, r_{max}(\theta) \cos \theta\}$. The resulting function of sheet velocity will then be implicitly dependent on the azimuthal direction. Moreover, equation 3.9 clearly demonstrates that the non-dimensional sheet velocity $\left(\frac{u_s(\theta)}{u_0}\right)$ differs from unity (as predicted by [Choo & Kang \(2002\)](#)). The sheet velocity ($u_s(\theta)$) not only represents the kinematics of the flow field inside the link but also acts as a transition parameter. The chain structure no longer remains stable because of Kelvin - Helmholtz instability if u_s exceeds a limit ([Villermaux & Clanet 2002](#)). The discussion so far gives an idea about the two-dimensional velocity field. Next, discussion has been reported about the three dimensional velocity field with an aid of streamlines and vectors at different locations to explain the subsequent collisions.

3.3.3 Three dimensional streamline structure

An overall consideration of the three-dimensional chain structure (Figure 3.7 (c)) allows knowledge about velocity patterns at different axial locations. The streamlines follow steadily the phase contour boundary, with those inside the chain structure going in trajectories similar to the outer boundary as shown in figures 3.7 (a) and 3.7 (e). Figure 3.7

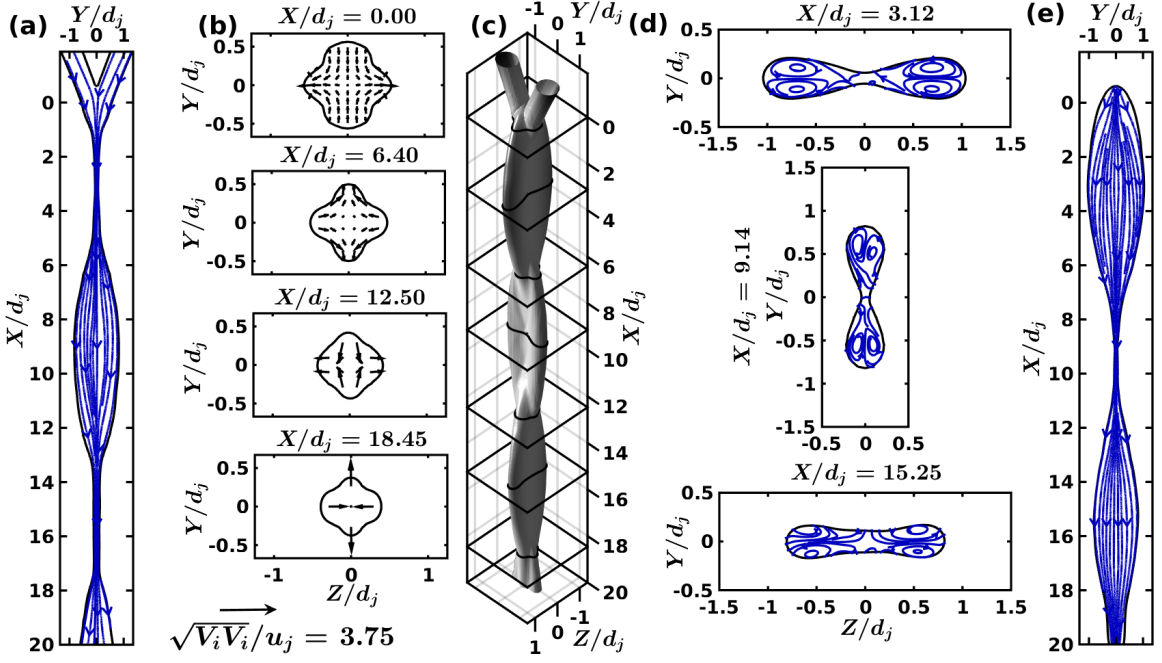


FIGURE 3.7: Three dimensional velocity field for $(\alpha, Fr, Re/Fr, Bo) = (30^\circ, 2, 1125, 3.4)$ with (a) XY plane streamlines, (b) velocity vector field in the YZ plane at different collision locations, (c) the three dimensional stable chain structure, (d) streamlines at maximum link widths in the YZ plane and (e) XZ plane streamlines.

(b) puts an effort towards highlighting velocity vectors at primary, secondary and tertiary links. One can observe from Figure 3.7 (b) that the spread of liquid influence at collision planes is reducing continuously as X/d_j increases. At the primary ($X/d_j = 0$) and tertiary ($X/d_j = 12.5$) collision points, the liquid jets and rims respectively converge onto themselves ($Z/d_j = 0$) marked by retracting velocity field, whereas the liquid sheet grows ($Y/d_j = 0$) in the Z direction, marked by an expanding velocity field. Trends opposite to these are obtained at the secondary ($X/d_j = 6.40$) and quaternary ($X/d_j = 18.45$) collision planes where a retracting velocity field is present at $Y/d_j = 0$ and expansion happens at $Z/d_j = 0$. This leads to the formation of three visible orthogonal links in this case (Figure 3.7 (c)). The velocity vector magnitudes go on increasing at each subsequent collision planes as the gravitational head is converted to dynamic head leading to narrowing of the extent of liquid phase boundary in the XZ plane. In the primary link, this converging-diverging trend of velocity vectors is continued from above the first collision point ($X/d_j = 0$) to the plane where the extent of the link perpendicular to the net flow direction in the plane of the link is maximum ($X/d_j = 3.12$). As illustrated in Figure 3.7 (d), the streamlines at the location of maximum width imply that the component of velocity perpendicular to the liquid sheet phase boundary is zero ($\frac{d\Psi}{dn} = 0$). This results in the formation of distinguished circulation patterns inside the lobes at the locations of the maximum extent ($X/d_j = 3.12, 9.14$ and

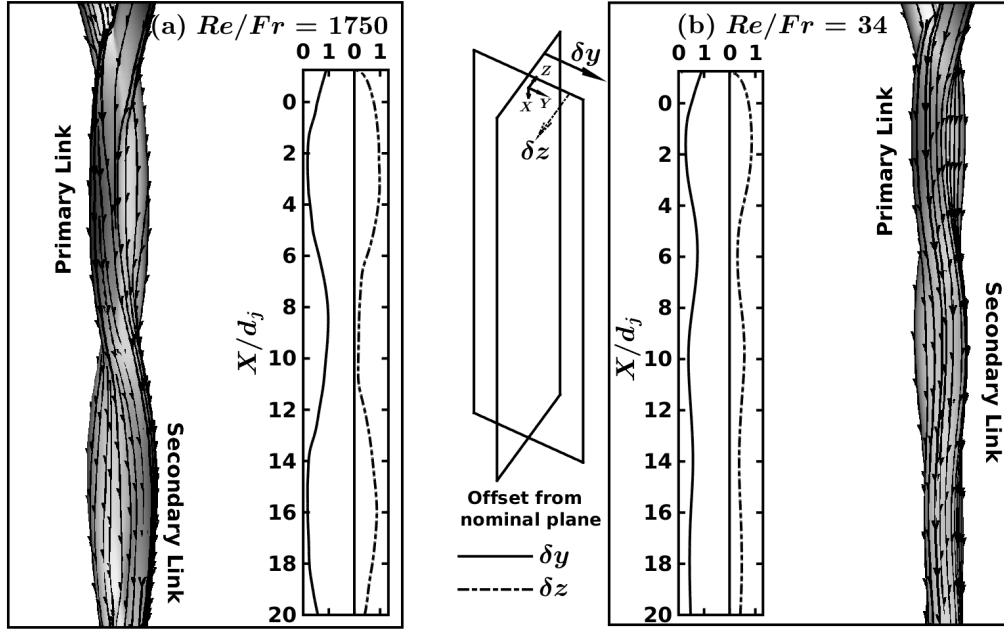


FIGURE 3.8: Three dimensional streamlines embedded on the chain structure illustrating the twist incurred as they traverse through the region of subsequent collisions for $\alpha = 30^\circ$, $Fr = 2$, $Bo = 3.4$ and (a) $Re/Fr = 1750$ and (b) $Re/Fr = 34$. The figures in inset show the offset (δy from XZ plane and δz from XY plane) of the streamline at the extreme end of the chain structure as it moves downstream with the flow for the corresponding cases.

15.25) corresponding to the three links visible in this case. Reduction of collision strength at different planes explains diminishing spans of the links, which can be also seen from sheet cross-sectional images (Figure 3.7 (d)).

A characteristic twist can be found in streamlines (Figure 3.8) as the flow propagates downstream through the locations of subsequent collisions. The twist occurs as the fluid parcels are restricted by surface tension to follow the chain's outer periphery. This twist is characterized by the offset of these streamlines from the two mutually orthogonal planes: the XY plane containing the axes of the liquid jets (δz) and the XZ median plane orthogonal to this one (δy). The offsets of the most extreme streamline are shown in the inset of Figure 3.8 for two representative cases having different ratios of Reynolds Number and Froude Number ($Re/Fr = 1750$ in Figure 3.8 (a) and $Re/Fr = 34$ in 3.8 (b)). The offset of all the streamlines from the XZ plane (δy) decreases continuously as the liquid jets approach each other (retracting velocity field as shown in Figure 3.7 (b)). After the collision, two extreme streamlines in XZ and XY planes are depicted in the inset of figures 3.8 (a) and 3.8 (b). It is observed that δy decreases continuously through the first link, but downstream of the second collision, the offset starts to increase, reaching the maxima at the location of the maximum width of the secondary link. The opposite trend is observed

for the XY plane whereby the offset (δz) increases after the first collision continuously till the maximum width of the primary link and then decreases for the secondary link. These variations in the offset of streamlines show the presence of twist, which is prominent until viscous effects start dominating and only a single jet of liquid is left at the end of the chain structure (as shown in Figure 3.8 (b) beyond $X/d_j = 16$). These viscous forces lead to dissipation of energy as the liquids jets (or rims for the post-primary link) collide with each other. It is clear from present discussions that values of dimensionless numbers α , Fr , Bo and Re/Fr determine the three-dimensional stable chain structures. The next section is devoted to analyzing such effects.

3.4 Parametric variation

Formation of the liquid sheet bounded by the rims is governed by inertia, viscous, buoyancy and surface forces apart from the angle of impingement between the jets (α). The relative importance of these forces is described by the parameters Fr , Bo and Re/Fr , as mentioned above. In this section, critical assessment of chain shapes is made for various non-dimensional numbers and impingement angles. [Yang et al. \(2014\)](#) acknowledged the importance of these parameters on collision process and formation of the first link. This analysis is used to generalize the effects of these parameters on the dimensions of the first link to the entire chain structure. The study is followed by the development of a regression model for the prediction of the shape and size of the first link using the control parameters of the liquid jets.

3.4.1 Variation of control parameters

Figure 3.9 shows the effects of the variation of the non-dimensional parameters on the first link which can be generalized in Figure 3.10 for the entire chain structure. Figures 3.10 (a)- 3.10 (d) show numerical chain structure for a several sets of parameters α , Fr , Bo and Re/Fr . An increase in impingement angle leads to decrease of jet momentum in direction of gravity ($u_j \cos \alpha$). Further, it must be noted that the sheet dimension in the direction parallel to that of gravity is dominated by the loss in gravitational potential ([Taylor 1960](#)), which remains unaffected during the transition. Further, the jet momentum in the plane perpendicular to the gravity is increased ($u_j \sin \alpha$). These effects result in a substantial increase in width of the sheet, keeping the length more or less intact (figures 3.9 (a) and 3.10 (a)). Alternatively, as the jet momentum is increased (increase in Fr), the resulting links are bigger (figures 3.9 (b) and 3.10 (b)) due to the fluid inertia. The increment can be

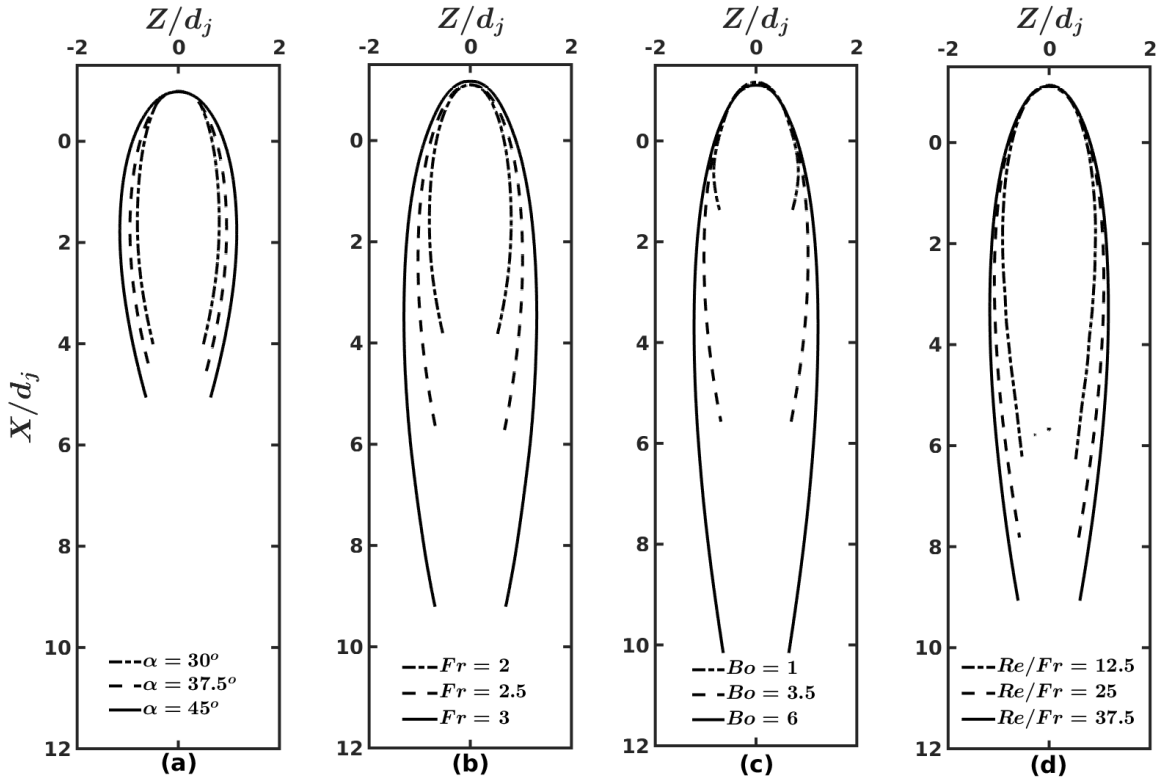


FIGURE 3.9: Variation of first link boundary with (a) α at $Fr = 2.5$, $Bo = 4.57$ and $Re/Fr = 34$ (b) Fr at $\alpha = 30^\circ$, $Bo = 3.4$ and $Re/Fr = 34$ (c) Bo at $\alpha = 30^\circ$, $Fr = 2.5$ and $Re/Fr = 34$ and (d) Re/Fr at $\alpha = 30^\circ$, $Fr = 2$ and $Bo = 3.4$.

explained with the fact that the increase in Fr or jets' momenta is directed related to the increase in the strength of the jets which in turn is a measure of the expansion tendency of the liquid sheets (Yang et al. 2014). One can clearly see this effect is transmitted to the subsequent links as well. Further, the surface tension is a crucial entity which influences the expansion of the link. As the surface tension is decreased (Bo increased), the link can expand until inertial and centrifugal forces balance it. This justifies obtaining larger links for higher values of Bo as seen in figures 3.9 (c) and 3.10 (c). As the surface tension is increased (low Bo regime), the system tries to go towards the minimum surface energy decreasing the dimensions of the corresponding links (link in Figure 3.10 (c) from $Bo = 6$ to 2). Further, the collision of cylindrical jets and rims is also observed to be influenced by viscous dissipations. Decrease of viscosity (increasing Re/Fr) leads to considerable increase in sheet dimensions but its effect saturates at lower ranges of liquid viscosities (figures 3.9 (d) and 3.10 (d)). This can be easily illustrated by observing the change in sheet dimension from $Re/Fr = 12.5$ to $Re/Fr = 37.5$ as compared to the change from $Re/Fr = 187.5$ to $Re/Fr = 1725$. Effect of change in liquid viscosity dies down as inertia and surface tension overshadow its resistance to form similar shape and sizes of links. It

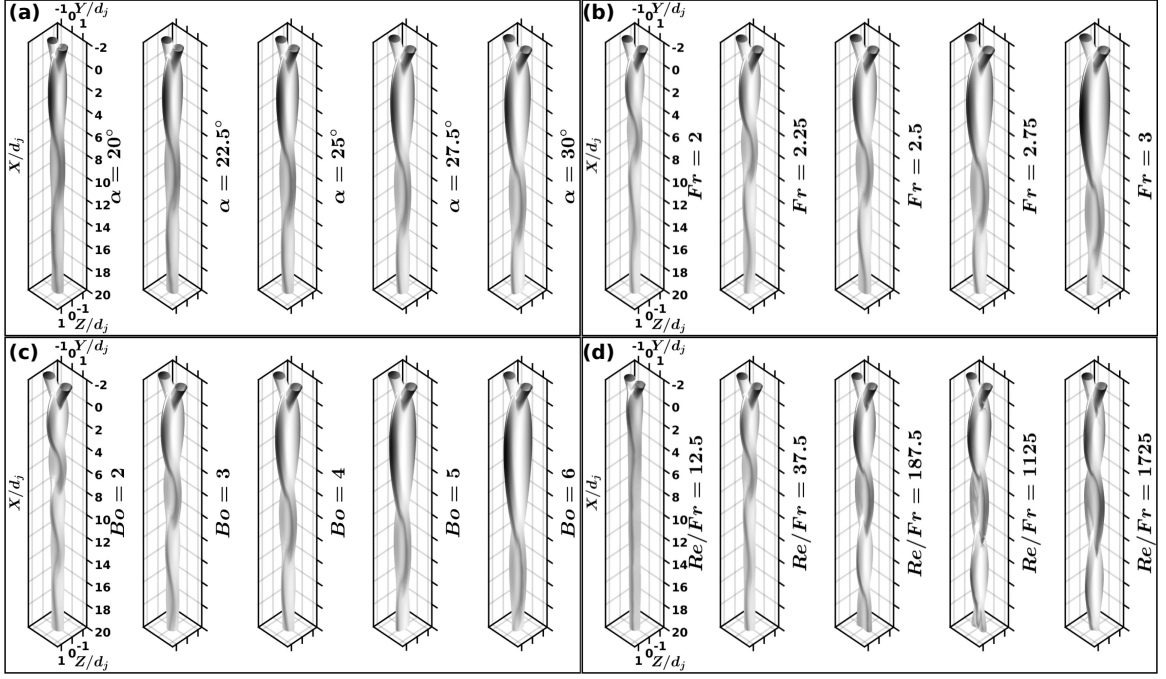


FIGURE 3.10: High fidelity numerical simulations of liquid jets collision to form chain structure for variation of (a) α at $Fr = 2.5$, $Bo = 4.57$ and $Re/Fr = 34$ (b) Fr at $\alpha = 30^\circ$, $Bo = 3.4$ and $Re/Fr = 34$ (c) Bo at $\alpha = 30^\circ$, $Fr = 2.5$ and $Re/Fr = 34$ and (d) Re/Fr at $\alpha = 30^\circ$, $Fr = 2$ and $Bo = 3.4$.

can also be noticed that it is the viscous dissipations that result in the decrement in the size of subsequent links leading to a point where the sheet coalesces into a single jet of fluid. The effect is prominent in Figure 3.10 (d) for $Re/Fr = 12.5$.

3.4.2 Prediction of chain structure using regression analysis

Considering ΔZ is the rim to rim distance at a particular vertical location (X) of the symmetric sheet, a third order polynomial is used to fit ($R^2 > 0.975$; $SSE < 0.01$) the sheet shape for various influencing parameters. The functional form of the polynomial is as follows:

$$\frac{\Delta Z}{2d_j} = \sum_{n=0}^{n=3} p_n \left(\frac{X}{d_j} \right)^n \quad (3.10)$$

Efforts are also made to relate polynomial coefficients (p_n) with non-dimensional numbers using linear regression analysis. Hence, p_n can be expressed as

$$p_n = C_{0,n} (\sin \alpha)^{C_{1,n}} (Fr)^{C_{2,n}} (Bo)^{C_{3,n}} (Re)^{C_{4,n}} \quad (3.11)$$

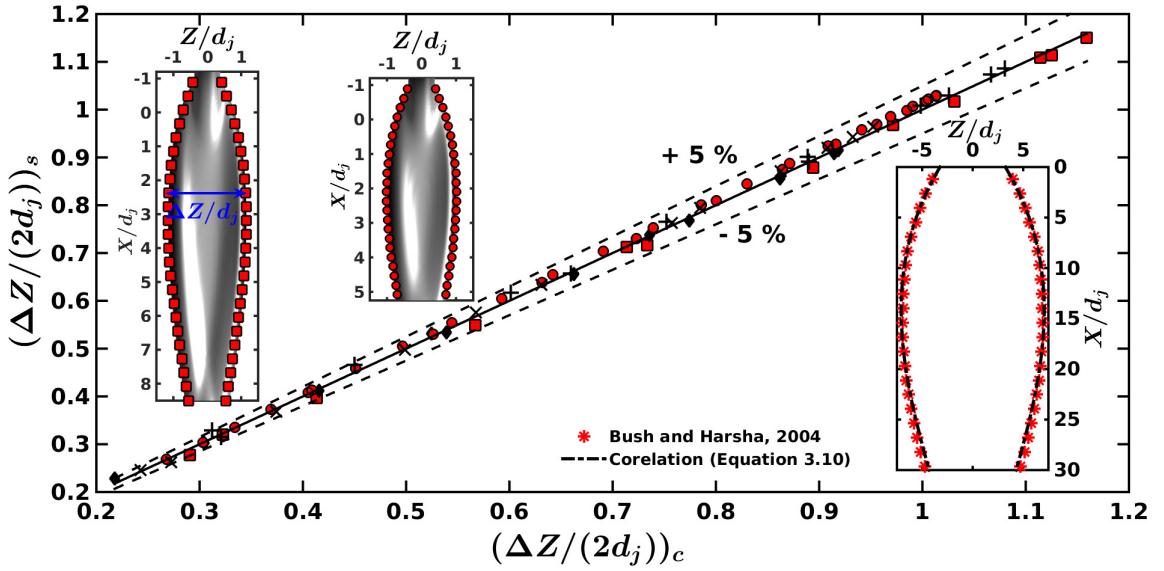


FIGURE 3.11: Comparison between the values of expansion of the sheet outer periphery ($\Delta Z(x)$) as predicted from equation 3.10 and from numerical simulations for different test cases with (symbol, α , Fr , Bo , Re/Fr) = (■, 30° , 2.5, 5, 34); (+, 30° , 2.5, 4, 34); (◆, 30° , 2.5, 2.3, 20); (×, 25° , 2.5, 4.57, 34) and (●, 30° , 2.5, 3.75, 20). The first two inset figures (from the left) visualize the corresponding three dimensional structure of the first link for the primary link and the third inset depicts the comparison between the equation 3.10 and the results of [Bush & Hasha \(2004\)](#).

Values of $C_{m,n}$ ($\forall m \in 0, 4$) in equation 3.11 are given in the Table 3.2 obeying R^2 norm of regression higher than 0.925. Predictability of the correlation with numerical chain contours are shown in the insets of Figure 3.11 for two different cases of non-dimensional numbers. It can be also observed from Figure 3.11 that the developed correlation gives a very good match ($\pm 5\%$) with the numerical sheet profiles. So as to check the capability of the correlation, for prediction of experimental profiles of the chain structure, the comparison is made between observation of [Bush & Hasha \(2004\)](#) and equation 3.10. The

TABLE 3.2: Factors ($C_{m,n}$) involved in equation 3.11 determined by linear regression analysis to find the polynomial coefficients of equation 3.10.

		n			
		0	1	2	3
$C_{m,n}$		0	1	2	3
m	0	3.662	2.720	0.353	0.512
	1	-0.082	0.490	1.146	0.592
	2	-2.166	-0.940	0.408	0.761
	3	-1.504	-0.831	0.074	-0.065
	4	-0.657	-0.290	0.029	0.039

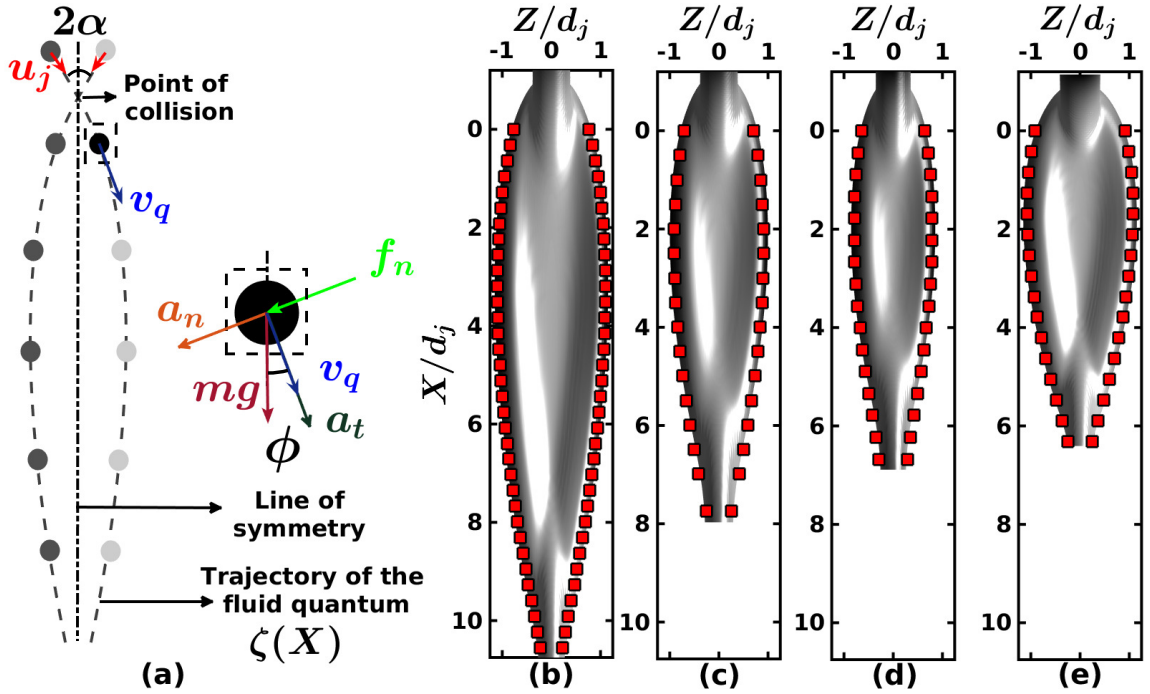


FIGURE 3.12: Fluid quanta collision analogy: (a) schematic of the model and free-body diagram and comparison between the link shape obtained through numerical simulations and the fluid quantum trajectory (ζ , ■) for $(\alpha, Fr, Re/Fr, Bo) =$ (a) $(30^\circ, 2.5, 34, 5)$, (b) $(30^\circ, 2.5, 23, 3.85)$, (d) $(30^\circ, 2, 34, 4.56)$ and (e) $(45^\circ, 2, 34, 3.4)$.

reported excellent match in the inset of Figure 3.11 confirms the universality of the developed correlation. It is essential to understand the formation physics of widely influenced sheet structure generated due to the collision of jets. Next section dedicatedly discusses the issue.

3.5 Analytical model

To bring out the physical insights of the liquid jet collision, idealizations are made for tracing back the sheet profile as a result of the collision between a train of fluid quanta (each of mass m), analogous to jet, in the plane of the sheet. It is assumed that the fluid quantum in a given jet interacts only with its mirror image in the other jet and that they are non-deformable. The collision is taken as friction-less. However, the follow-up trajectory of these fluid parcels after the collision is considered damped so as to mimic resistive forces like viscous and surface tension. A free body diagram and schematic of the fluid quanta collision are depicted to replicate the sheet structure in Figure 3.12 (a). Apart from inertial and gravitational forces, on the fluid particle, a damping force of magnitude f_n (to impose the effect of viscous dissipation and surface forces) is also attached in the direction

perpendicular to the individual packet's instantaneous velocity, post-collision. Absence of these resistive forces will make infinitely stretched sheet (Taylor 1960), with $f_n = 0$ case. In-situ assessment of damping force based on local velocity may improve the prediction of resistive forces which has not been targeted in the present effort. Reference frame for the trajectory of the fluid quantum (ζ) is considered to have the origin at the point of collision with $\zeta = 0$ at $X = 0$. Free body force analysis of the fluid particle, post-collision, can be expressed as equations 3.12a and 3.12b, with accelerations a_n and a_t in normal (n) and tangential (t) directions, respectively.

$$\text{Direction t: } a_t = v_q \frac{dv_q}{ds} = g \cos \phi \quad (3.12\text{a})$$

$$\text{Direction n: } a_n = g \sin \phi + \frac{f_n}{m} = \frac{v_q^2}{r_c} \quad (3.12\text{b})$$

Here, r_c is the radius of curvature in $\zeta - X$ plane and $\phi = \tan^{-1} \left(\frac{d\zeta}{dX} \right)$. Integrating tangential momentum equation with increment $ds = dX / \cos \phi$ along with boundary condition at $X = 0$, instantaneous fluid particle velocity (v_q) can be obtained as $\sqrt{u_j^2 + 2gX}$. Rearrangement of momentum equation in the normal direction after defining Λ as $\frac{f_n}{mg}$ and inertial length scale, χ equivalent to $\frac{u_j^2}{2g}$, one obtains:

$$r_c (\sin \phi + \Lambda) = 2\chi \left(\frac{X}{\chi} + 1 \right) \quad (3.13)$$

After necessary integration, equation 3.13 simplifies to:

$$\sin \phi = \sin \alpha + (\Lambda + \sin \alpha) \left(\frac{1}{\sqrt{\frac{X}{\chi} + 1}} - 1 \right) \quad (3.14)$$

Recalling that $\tan \phi = \frac{d\zeta}{dX}$ and expressing $\Lambda / \sin \alpha = \eta$, profile of fluid quantum movement can be characterized as:

$$\frac{d\zeta}{dX} = \tan \left\{ \sin^{-1} \left[\sin \phi_0 (1 + \eta) \left(\frac{1}{\sqrt{\frac{X}{\chi} + 1}} - 1 \right) \right] \right\} \quad (3.15)$$

The functional form of the fluid particle trajectory, the equivalence of sheet profile, can be integrated numerically to obtain the coordinate points in the $\zeta - X$ plane after tuning only control factor, η from some simulated profiles. In this process, L^1 relative error norm is kept below 10%. Efforts have been also made to express control parameter, η in terms of

non-dimensional numbers for the range of values presented in this work. With 99% R^2 regression norm, η can be related with non-dimensional numbers as:

$$\eta = 3.28(\sin \alpha)^{-0.077}(Fr)^{0.502}(Bo)^{-0.248}(Re)^{-0.084} \quad (3.16)$$

Proposed concept of collision of fluid quanta for mimicking the sheet profile is also tested with phase contours of numerical simulations. Some representative matches are shown in figures 3.12 (b) - 3.12 (e) in connection of primary link. Fundamental analysis of forces, a single controlling parameter in sheet profile (equation 3.15) and an excellent match with numerical data supply in-depth knowledge about the formation of the liquid chain. Next, focus has been kept on the mutual relationship between links formed at successive orthogonal planes.

3.6 Inter-relation between inter-connected links

The secondary and tertiary links observed in mutually perpendicular planes initiate with the collision of rims in preceding links. From numerous simulations in the wide range of operating parameters, it can be observed that secondary, tertiary and subsequent links of a chain are equivalent to primary, secondary and subsequent links of another chain having different operating parameters. Hence, it is proposed that subsequent links are equivalent to resultant of collision between two free jets having reduced strength. To prove the proposal in Figure 3.13 (a), a representative chain structure is identified for $\alpha = 30^\circ$, $Fr = 2.5$, $Bo = 4$, $Re/Fr = 34$ (Case 1), in which secondary links showed resemblance with primary link of $\alpha = 25^\circ$, $Fr = 2.2$, $Bo = 4$, $Re/Fr = 34$ (Case 2). Continuing this, one can also establish analogy among tertiary link of Case 1, secondary link of Case 2 and primary link of $\alpha = 11.25^\circ$, $Fr = 1.98$, $Bo = 4$, $Re/Fr = 34$ (Case 3). One to one correspondence of these links of different cases establishing present proposal is shown in the comparative graph of Figure 3.13 (b).

It can be commented that subsequent links are reduced in size, giving a feeling of resultant of impact between two weaker jets. The analogy between interconnected links in a chain and one level lower link of another chain is found to be valid with $\pm 10\%$ confidence for the entire region of search space of the operating parameters (α , Fr , Re/Fr , Bo). A critical assessment of links in chain structure and rim profile has also established that angle of impingement between rims successively reduces $\alpha_n/\alpha_{n-1} < 1 \forall n = 1, 2, 3$ and higher integers. It has been also checked that analogy of collision between fluid parcels and formation of the link by the interaction between rims is also valid after

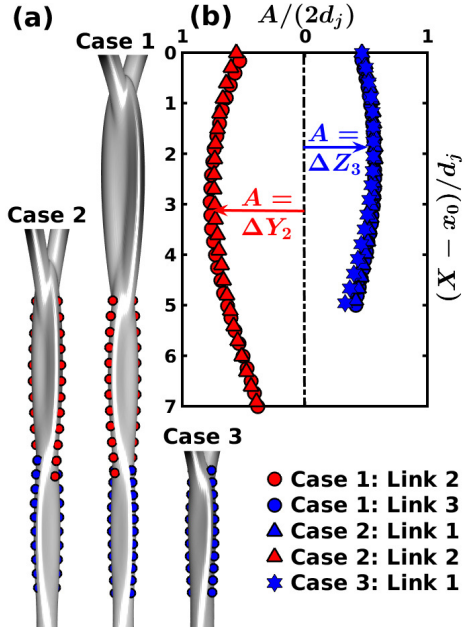


FIGURE 3.13: Inter-relation between links of chain reproduction of secondary link of Case 1 ($\alpha = 30^\circ$, $Fr = 2.5$, $Bo = 4$, $Re/Fr = 34$) as primary link of case 2 ($\alpha = 25^\circ$, $Fr = 2.2$, $Bo = 4$, $Re/Fr = 34$) and tertiary link of Case 1 as secondary link of Case 2 and primary link of case 3 ($\alpha = 11.25^\circ$, $Fr = 1.98$, $Bo = 4$, $Re/Fr = 34$) using (a) three dimensional chain structure and (b) two dimensional planar link locations.

taking the reduction of angle of impingement into consideration. This trend is shown in the figures 3.14 (a) - 3.14 (b) for secondary and tertiary links for few chain cases randomly scattered in search space. With only $\pm 10\%$ error, theory of collision between the fluid quanta (equations 3.15 - 3.16) has also found to be applicable for n^{th} order link of chain. Polynomial proposed in equation 3.10 also predicts formation of n^{th} order link satisfactorily with modified strength and impingement angle. Clustering of points near (1,1) for secondary link (Figure 3.14 (a)) and (0,0) for tertiary link (Figure 3.14 (b)) establishes continuous reduction of impingement angle α_n with increase in link number n . Besides the reduction in angle of impingements, the interaction between rims of a link can be also considered as the collision between jets of lesser Froude number (Fr_m) than Fr_j . The monotonous decrement of Fr_m is observed as one traverses in subsequent higher level links along a chain. Figure 3.14 (c) establishes this idea where the ratio between rim Froude number of secondary link (Fr_2) to jet Froude number (Fr_j) has been fitted as 0.88 and that of same for the tertiary link (Fr_3/Fr_j) as 0.8.

These decrements are a result of the viscous dissipations which are prominent at the time of the collision and has been illustrated in Figure 3.15 (with the extreme cases of variations shown as insets figures across each graph) for the entire domain of non-dimensional

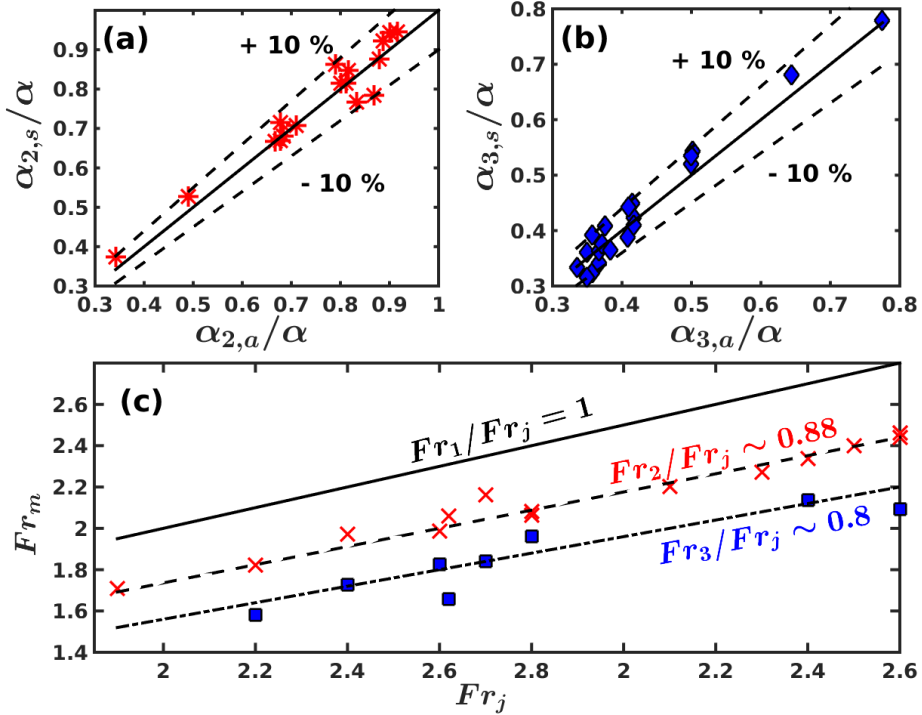


FIGURE 3.14: Generalization of fluid rim collision for the higher order links with the prediction of angles of impingement for (a) secondary and (b) tertiary collisions and (c) the account of rim strength (Fr) in different links.

numbers considered in the present work. The dimensional characteristics of the secondary and tertiary links are studied as relative to the primary link. The range of values of l_i/l_1 and d_i/d_1 is always less than 1. Further, it must be noted that the final resultant liquid jet formed after the diminishing of chain structure also shows some undulations on its surface. Therefore, we have considered the presence of higher order links only if the difference in relative dimensional characteristics is more than 30%. For fluids with higher viscosities, the formation of this resultant jet is most prominent as shown in Figure 3.15 (a). As the viscosity is decreased (Re is increased), there is a sudden increase in the dimensional characteristics because of the reduced viscous dissipations at the time of collision of subsequent rims of the sheet. However, similar to the effects of Re on single link dimensions, this influence saturates after the initial increase as for the less viscous fluids (high Re). The formation of chain structure is surface tension and inertia driven. Further, with an increase in the inertia of the liquid jets, the individual links grow in size but because of the viscous dissipations, this effect is not transmitted equally downstream of the flow. The second link also increases in dimensions but the length and width of the second link are always smaller than the primary link (Figure 3.15 (b)). Moreover, an increase in the Bo (decrement in the surface tension coefficient of the interface), the length and width of the first link increase

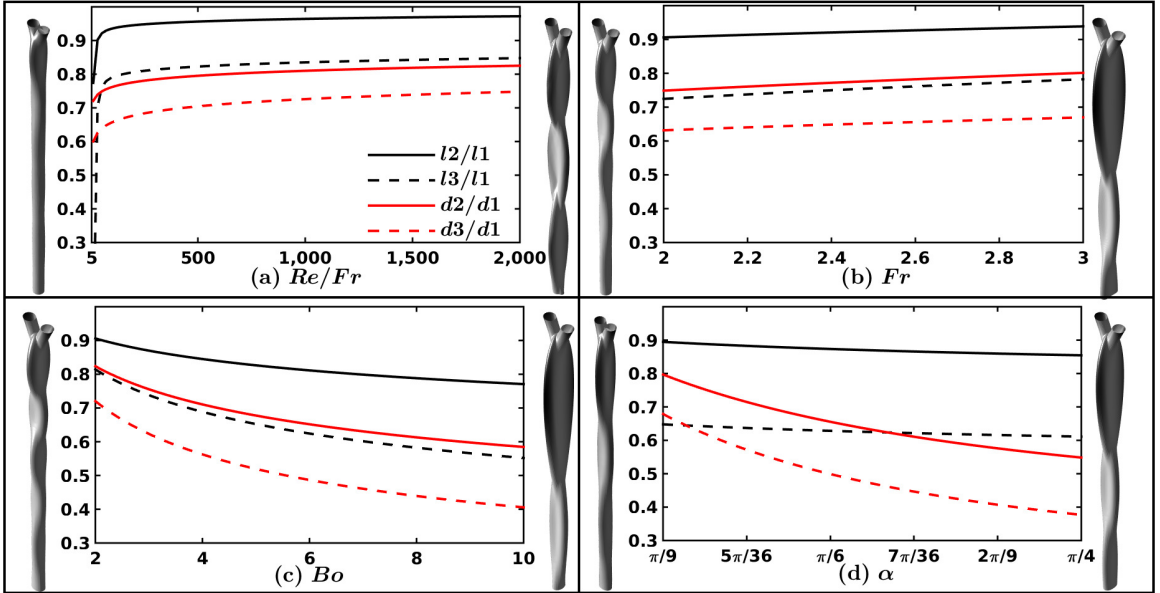


FIGURE 3.15: Evaluation of the dimensional characteristics of the secondary and tertiary links relative to the primary link, for variations of (a) α at $Fr = 2.5$, $Bo = 4.57$ and $Re/Fr = 34$ (b) Fr at $\alpha = 30^\circ$, $Bo = 3.4$ and $Re/Fr = 34$ (c) Bo at $\alpha = 30^\circ$, $Fr = 2.5$ and $Re/Fr = 34$ and (d) Re/Fr at $\alpha = 30^\circ$, $Fr = 2$ and $Bo = 3.4$.

substantially (Bremond & Villermaux 2006; Yang et al. 2014). As a result, the primary sheet thickness and the rim diameter decrease leading to the reduction of the inertia of the rims responsible for the secondary and subsequent collisions. Therefore, the dimensional characteristics of the higher order links as compared to the first one, decrease with an increase in Bo (Figure 3.15 (c)). A similar decrement is also observed if the angle of impingement is increased (Figure 3.15 (d)) as the primary link grows faster in size than the others. Though the idea of the interrelation between the links is established only for first three, it can be extrapolated for higher order elements in the chain until it transforms into a jet.

3.7 Summary

The stable chain structures are formed by the collision of laminar liquid jets when the inertia forces are, in order of magnitude, similar to the surface tension forces. A series of fully resolved numerical simulations showed that individual links, formed by collision of cylindrical jets (primary) or rims (secondary onward), occupy mutually orthogonal planes with a successive reduction in size owing to viscous effects. The fluid parcels inside these links are dispatched radially outwards from the stagnation point and follow trajectories self-similar to the phase boundary. The variation of the velocity field across the radial coordinate

is found to be negligible whereas the azimuthal variation of the sheet velocity is scaled using its average, given by an empiric relation. Further, at the collision planes, the velocity field is found to be retracting in the direction of the colliding jets and rims whereas it is expanding in the plane of the formed sheets. The inertial and gravitational forces provide a measure of the expansion of these sheets counteracted by the surface tension at the interface and viscous dissipations at the subsequent collisions. An increase in the impingement angle (α) leads to wider links of the chain with a negligible change in the length of individual links. Intuitively, the size of the stable chain structure increases with an increase in the momenta of the jets (Fr) or with a decrease in the strength of the surface tension force (increasing Bo). Increase in the Re presents a sharp increase in the dimensions of the chain, which saturates at the higher values of Re . Moreover, the individual symmetric sheet profile can be modeled using a third order polynomial, with an accuracy of $\pm 5\%$, with coefficients dependent on various non-dimensional numbers featuring the interplay of different forces. Effects of these forces have been understood by mimicking them onto the post-collision trajectory of fluid quanta. Higher order links are found to be similar to lower or primary level element formed due to impact between jets of reduced Fr and α .

Chapter 4

Air entrainment by jet impingement*

*The results presented in this chapter are published in: Sanjay, V and Das, A. K. (2017). “On air entrainment in a water pool by impingement of a jet”. AIChE Journal, 63.11, pp. 5169 – 5181. DOI : 10.1002/aic.15828.

4.1 Introduction

In this chapter, the investigation of air entrainment due to impingement of a water jet on a pool is studied extensively to understand the physics of the initiation and the cluster of bubbles formed below the free surface. A look around reveals the presence of this phenomenon in everyday life, ranging from filling of a glass of water using tap to several chemical reactions, such as mineral flotation, steel teeming process and gas absorption. [Evans et al. \(1996\)](#) defines a plunging liquid jet as a moving column of liquid that passes through a gaseous head-space before impinging on the horizontal free surface. In his review work, [Biñ \(1993\)](#) reviewed previous works in the area of the impinging jet in a pool and showed the application of the same in the field of wastewater treatment. Entrainment is desirable in processes like aeration reactions during wastewater treatment whereas it is undesirable in processes such as pouring of molten metals during casting or glass molding. Hence, it is important to understand the physics behind this phenomenon so that the processes it affects, directly or indirectly, can be optimized. Possible outcomes due to the jet impingement in a pool have been identified as smooth free surface without entrainment or formation of rigorous bubble cluster below the jet-pool contact ([Roy et al. 2013](#)). A triangular entrained region is found to be a three-dimensional association of disconnected bubble population continuously breaking and making with the neighbors ([Bagatur 2014; Belden et al. 2012; Harby et al. 2014](#)). A correlation for prediction of maximum entrained height for a range of jet diameters and lengths is proposed. The trajectory of a single bubble is also studied to understand the kinematics of the bubble cluster. Alongside, an electrical conductivity probe has been used to examine the probabilistic presence of the bubble at a given depth in the liquid pool.

4.2 Experimental setup and methodology

An in-house experimental setup to investigate the phenomenon of air entrainment by impinging liquid jet is developed. Figure 4.1 (a) illustrates the schematic of this experimental facility. A water pool in a Plexiglas tank ($0.5\text{ m} \times 0.5\text{ m} \times 0.5\text{ m}$), is impinged by a water jet (with properties as given in Table 4.1). The flow of the jet is controlled using valves and is measured with a calibrated rota-meter at ambient conditions. Arrangements are made to lower the jet for variation of its height from the pool (l_j). Further, the jet diameter (d_j) can be changed by using different guiding nozzles. The injection system is kept as sufficiently long ($\sim 120D$) to obtain fully developed velocity profile in the injected water jet.

Noticing the dynamics of the problem, it is realized that the depth of the entrainment (d_s) is

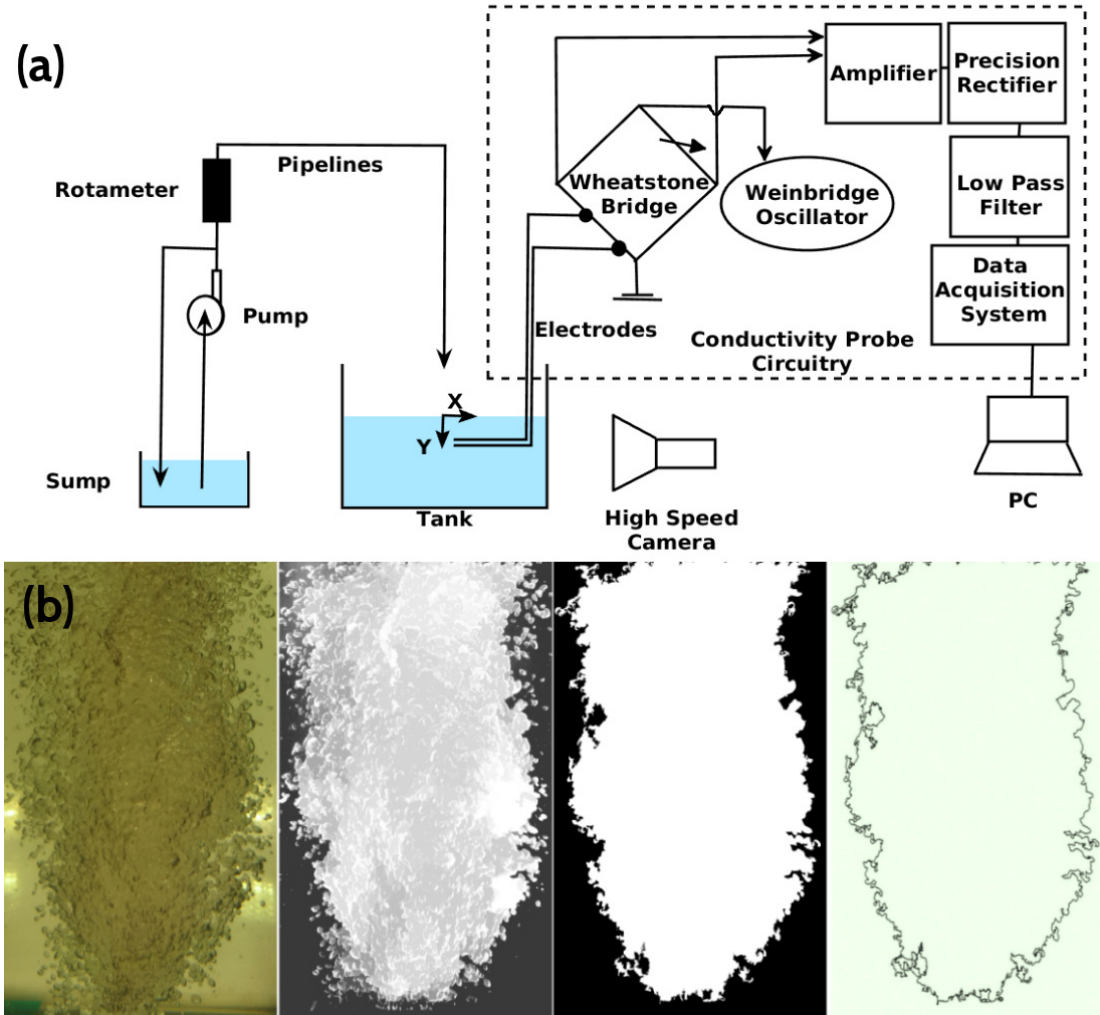


FIGURE 4.1: (a) In house developed experimental setup for the study of entrainment process. The coordinate system has been defined using the Cartesian system centered at the point of impact of the jet on the pool. (b) Sequence of image processing applied for the characterization of the bubble cluster.

dependent on the kinematic or geometric control parameters, such as the diameter of the jet (d_j), velocity of the jet (u_j), its length (l_j) along with other physical variables such as the density of the liquid (ρ_l), viscosity (μ_l), surface tension, σ and acceleration due to gravity (g).

$$d_s = \Phi(u_j, d_j, \rho_l, \mu_l, \sigma, g) \quad (4.1)$$

Assuming, u_j , d_j and ρ_l as the repeating variables in equation 4.1, the functional relation shown in equation 4.2 is obtained.

$$\frac{d_s}{d_j} = \Psi \left(\frac{\sqrt{gd_j}}{u_j}, \frac{l_j}{d_j}, \frac{\mu_l}{\rho_l u_j d_j}, \frac{\sigma}{\rho_l u_j^2 d_j} \right) \quad (4.2)$$

TABLE 4.1: Details of the physical properties of the tap water used in the experiments and the ambient air conditions.

Fluid	Density (kg/m ³)	Viscosity (Pas)	Surface Tension (Nm)
Water	1000	0.001	
Air	1.24	1.8e-5	0.072

TABLE 4.2: Variation of different parameters associated with the flow. The Reynolds number and the product of Froude numbers are based on jet characteristics

Flow Rate (x 10 ⁻⁵ m ³ /s)	Nozzle Diameter (m)	Reynold's Number Re	Froude Numbers Fr _D Fr _L
1.67 to 100	0.01 to 0.0256	2000 to 50000	1 to 4

The first term (inverse of the diametrical Froude number, Fr_D) is a measure of the inertia of the circular jet whereas the second term is directly associated with the gravitational potential available to the jet as it starts its descent towards the pool. Further, the last two terms can be identified as the inverse of the Reynolds and the Weber number. The diametrical Froude Number (Fr_D) and the jet length ratio ($\frac{l_j}{d_j}$) present the control aspects of these experiments and simulation. These terms can be combined into the product of the Froude Numbers and the uniqueness of a particular flow configuration is considered using the number, $Fr_D Fr_L = \left[\frac{V}{\sqrt{gD_j}} \right] \left[\frac{V}{\sqrt{gl_j}} \right]$, where Fr_L is the longitudinal Froude Number. Table 4.2 contains the range of variations involved in the present study. The high-speed camera is used to capture the dynamic behavior of the entrainment process with a maximum frame rate of 2000 frames per second at full resolution. The raw images obtained from the high-speed camera are passed through RGB to grayscale conversion, noise removal by subtracting background and grayscale to black and white conversion stages. From temporal black and white images, feature extraction, like the centre of mass evaluation and area determination of cluster, are performed. Sobel technique is used for interface tracking using which is the maximum depth of entrainment penetration is determined. Figure 4.1 (b) illustrates different stages of image analysis.

Moreover, an electrical conductivity probe is developed to detect the presence of entrapped air bubbles at a given spatial coordinate in the liquid pool. The working principle of conductivity probe is variable resistance when different (air/water) medium closes the circuitry between two copper electrodes as illustrated in figure 4.1 (a). To convert the instantaneous

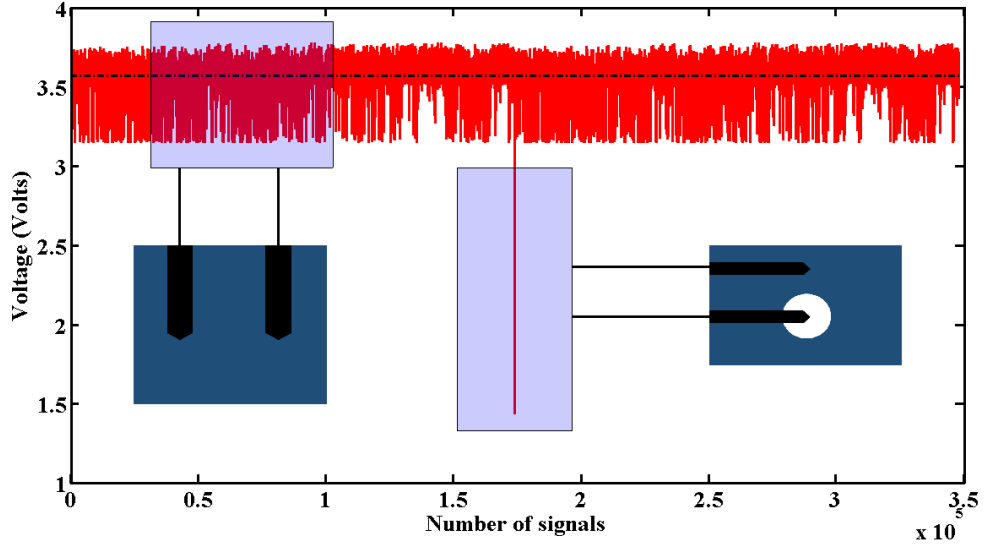


FIGURE 4.2: Signal behavior for different closure of circuitry. In case water closes the circuit the voltage signal is normal. However, with the presence of bubbles, an instantaneous dip can be observed

variable resistance into a measurable voltage signal, electronic circuitry has also been developed. Figure 4.2 gives an idea about the behavior of probe signals for different media completing the circuitry in between the electrodes. In the next section, the mathematical setup used for spatio-temporal fully resolved simulation of the process is explained. Care has been taken to accommodate at least 10 cells inside disconnected interface for accurate capture of the interfacial dynamics. No turbulence model is used in the model framework.

4.3 Numerical model

Bubble entrainment is studied in a three-dimensional finite volume framework using the Volume Of Fluid (VOF) approach for interface tracking. Open source solver, Gerris is used for the study ([Popinet 2003](#)). It implements the finite volume discretization on an octree adaptive grid with piecewise linear VOF model.

4.3.1 Setup of the numerical model

Figure 4.3 illustrates the computational domain with dimensions $30d_j \times 10d_j \times 10d_j$. The lateral surfaces are modeled as boundaries using no-slip condition. The distance of these walls from the centerline of the jet ($5d_j$) is kept large to avoid any biasing from boundaries. The bottom boundary is given a controlled velocity out-flux condition, to ensure

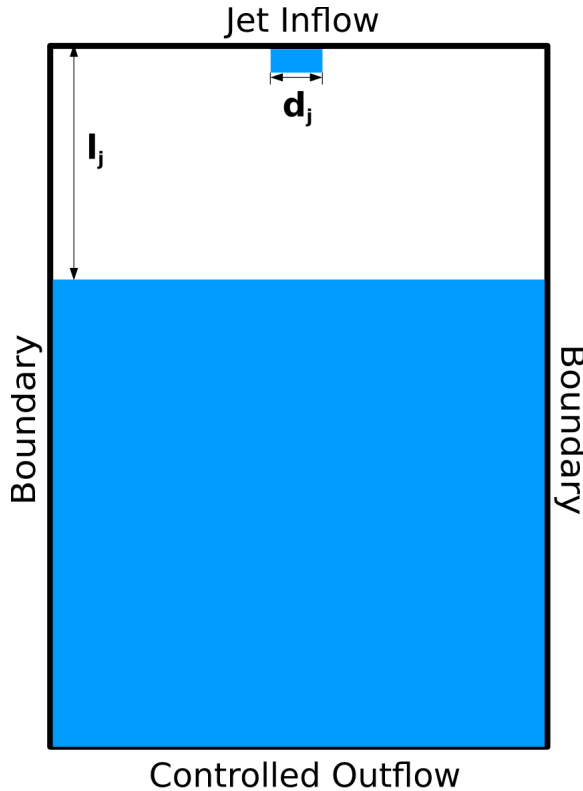


FIGURE 4.3: The computational domain with the implemented boundary conditions.

that the water level does not change whereas the top boundary has jet inflow and outflow boundary condition. A small jet is initialized at the start of the simulation, along with the water pool. The product of the Froude numbers ($Fr_D Fr_L$) determines the average inlet velocity of the liquid jet and the velocity profile depends on the turbulent character of the jet. If the Reynolds number of the jet is below 2300 (laminar jet), parabolic profile $\left[2\left(1 - \left(\frac{2r}{d_j}\right)^2\right)\right] u_j$ is patched whereas power law velocity profile $\left[\frac{8}{7}\left(1 - \frac{2r}{d_j}\right)^{\frac{1}{7}}\right] u_j$ is used for turbulent jets. With the above mathematical model in place, mesh sensitivity analysis is carried out.

Refinement is bestowed adaptively based on the gradient of the volume fraction of fluid $\alpha(x_i, t)$. This ensures that the number of cells around the interface is sufficient enough to capture small-scale variations. Let, δl be the size of a cell, which is non-dimensionalized as $\frac{d_j}{\delta l}$, a measure of the total number of cells across the diameter of the jet. Keeping the minimum $\frac{d_j}{\delta l}$ constant, the maximum $\frac{d_j}{\delta l}$ is varied from 204.8 to 6.4 (Level 11 and 6 respectively in Gerris 3D simulation) as cataloged in Table 4.3. On achievement of consistency in the result for the time taken (non-dimensionalized as $\frac{V_j t}{d_j}$) to first pinch off, the minimum $\frac{d_j}{\delta l}$ is varied. It must be noted that the minimum value of $\frac{d_j}{\delta l}$ is never reached near the interface as it is always well resolved with maximum refinement available. All the considered cases

Case	$\left(\frac{d_j}{\delta l}\right)_{max}$	Maximum level	$\left(\frac{d_j}{\delta l}\right)_{min}$	Minimum level
1.	6.4	6	1.6	4
2.	12.8	7	1.6	4
3.	25.6	8	1.6	4
4.	51.2	9	1.6	4
5.	102.4	10	1.6	4
6.	204.8	11	1.6	4
7.	102.4	10	3.2	5
8.	102.4	10	6.4	6
9.	102.4	10	12.8	7
10.	102.4	10	25.6	8

TABLE 4.3: Designation of cases considered for the grid sensitivity analysis.

Case	$\left(\frac{d_j}{\delta l}\right)_{max}$	$\left(\frac{t_{CPU}}{t_{actual}}\right)$ (days/s)
4	51.2	~ 7.5
5	102.4	~ 10
6	204.8	~ 15.5

TABLE 4.4: CPU performance data for simulations done for the Grid Independence Study. The simulations are done using four Intel Core i7-6500U CPU having clock speed of 2.5GHz each and 8 GB RAM.

are given in Table 4.3. The parameters for these cases are kept constant at $Fr_D Fr_L = 1.4$. Figure 4.4 shows the consequences of this analysis. It can clearly observed that the result saturates after the fourth case. From CPU performance data of Table 4.4, one can note that case 5 can be adopted as optimum grid structure keeping compromise between accuracy and runtime.

Figure 4.5 shows the velocity profile at different locations across the jet, out of which location 1 is very near to the boundary where power law velocity profile has been patched (as described earlier in the mathematical formulation). Downstream to this, point 2 lies outside the liquid pool and has a fully developed water jet with high magnitude of velocities near the periphery where the air is present. A part of jet's initial gravitational potential has been converted into its kinetic energy resulting in higher velocity and lower instantaneous diameter. Other points are inside the pool with location 3 in the region surrounded by the thin air sheath whose small velocity is reflected near the interface of the jet. Though the jet is inside the pool, it still retains its identity (with a lower velocity than expected due

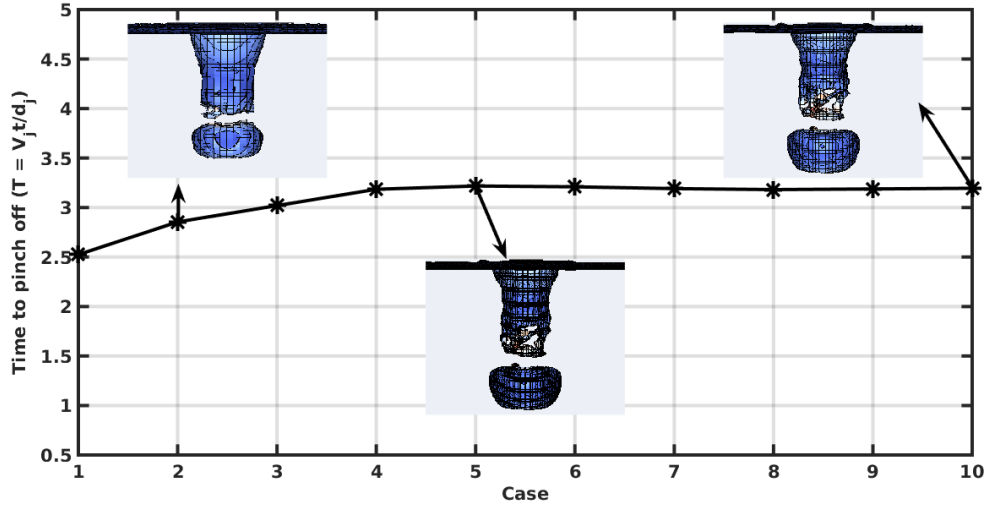


FIGURE 4.4: Determination of time taken for pinch off of first bubble after impact on the pool. The in-box figures represent instant of the pinch off. The $Fr_D Fr_L = 1.4$ and $Re = 8000$ are kept constant. Interfacial grids obtained by full Adaptive Mesh Refinement (AMR) are shown in the inset corresponding to case 2 with a relatively coarse grid as well as in case 5 and case 10 with fine grids.

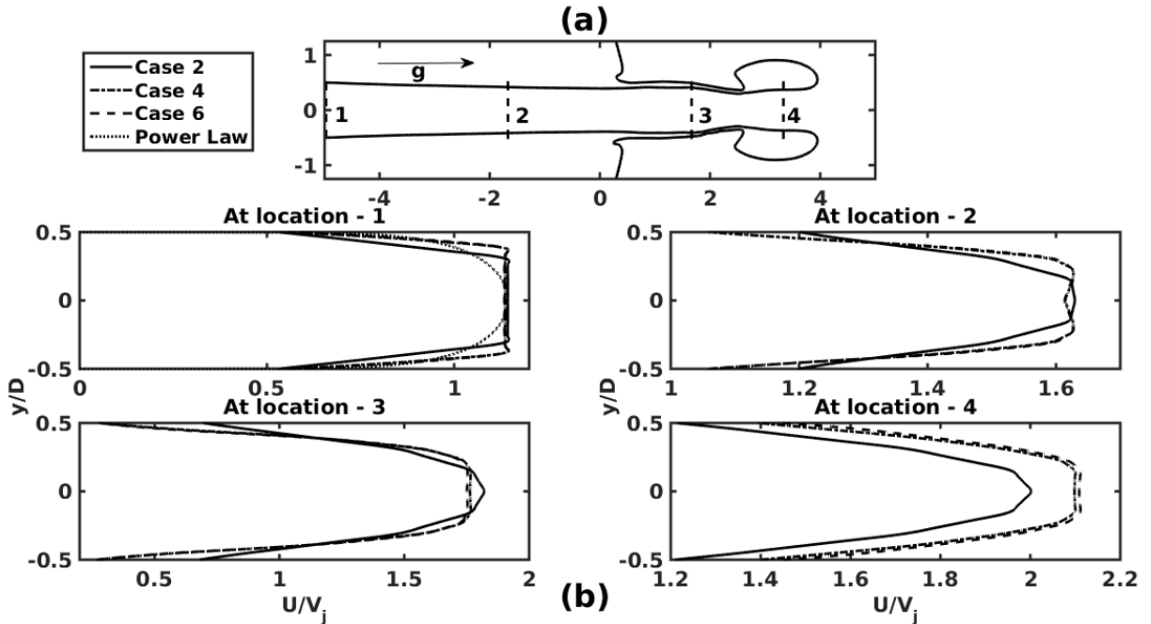


FIGURE 4.5: (a) Schematic of the different locations where the velocity profile is plotted and compared. The phase boundary corresponds to that of case 6. (b) Velocity profile as observed at indicated locations. ($Fr_D Fr_L = 1.4$ and $T = \frac{V_j t}{d_j} = 2.5$)

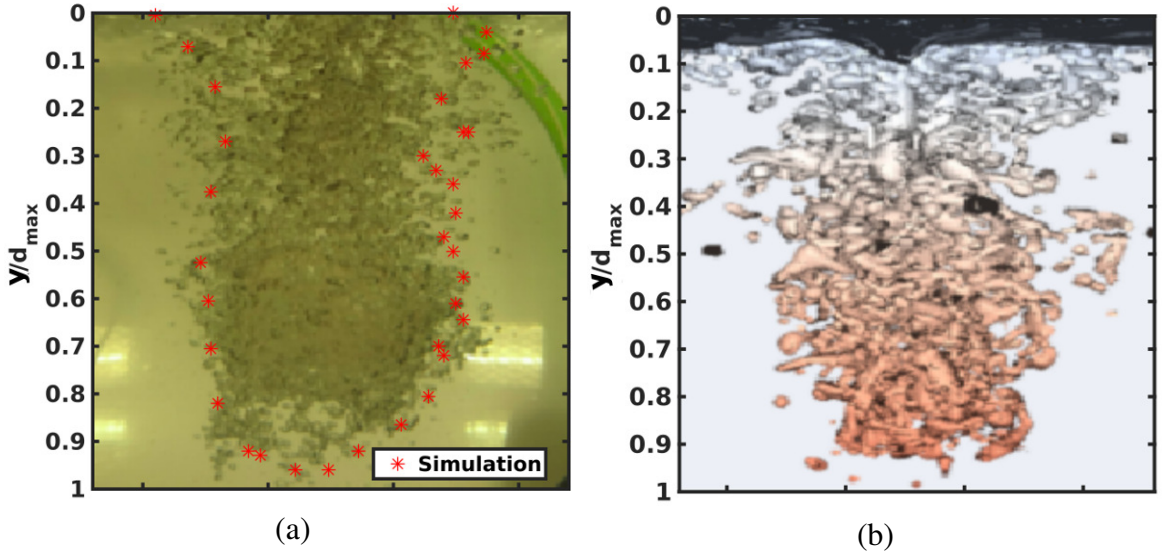


FIGURE 4.6: (a) Experimental snapshot of the bubble cluster below the liquid pool with points of the interface obtained from numerical simulation (b) Numerically obtained bubble cluster at $Fr_DFr_L = 1.4$; both experimental snap and numerical contours are plotted at $T = 300$ starting from jet touching the pool.

to impact with the pool) and after the pinch-off of the first bubble, jet continues to entrain bubbles inside the pool. Finally, location 4 is in the liquid region of the first annular bubble that pinches off. Figure 4.5 clearly demonstrates that the velocity profile is independent of spatial refinement beyond case 4, justifying the approach to select the mesh parameters of case 5 as the fundamental configuration.

4.3.2 Validation of the numerical code

Next, the numerical code employed is tested for its validity by virtue of its correspondence with the experimental observations. Figure 4.6 contains the results of validation test carried out for $Fr_DFr_L = 1.4$. The numerically simulated interface structure shows a remarkable similarity with the experimentally obtained bubble cluster interface. Velocity variation of a bubble in the cluster with time is obtained from experimental snaps and reported in figure 4.7 (a) along with data of a bubble from a numerical simulation. A close match between numerical prediction and experimental observation validates the developed model. Moreover, efforts are also made to measure the area occupied by the bubble cluster from temporal snaps of experimental observation. Development of cluster area with time from the experiment is plotted in figure 4.7 (b) along with numerical findings. It can be observed from the figure that experiment and numerical simulation corroborates similar observations for a range of Fr_DFr_L . Next section illustrates the two possible outcomes of the jet-pool

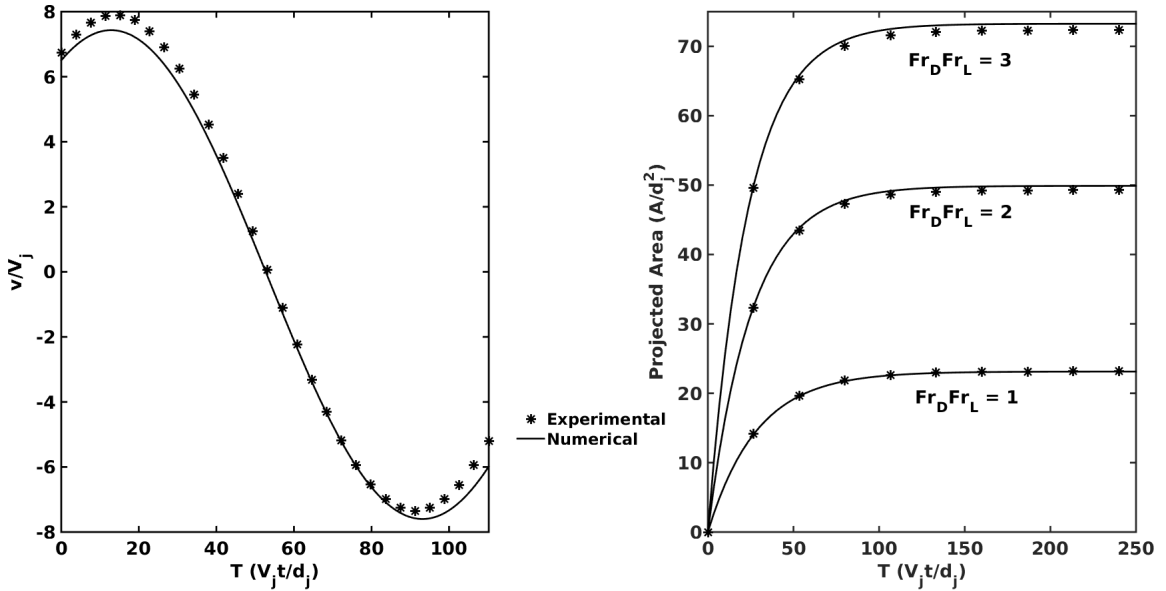


FIGURE 4.7: Comparison between experimental and numerically obtained results for temporal variation of (a) Velocity vector of a typical bubble in the entrained region at $Fr_D Fr_L = 1.8$ (b) Projected area of the entrained bubble cluster

interactions, no entrainment, and vigorous bubble cluster formation. These are obtained from experimental snapshots.

4.4 Continuous and no entrainment

Figure 4.8 shows two types of possibilities when the liquid jet impinges the water surface. Even though, the inception of air bubble entrainment is not easily characterized. Experimental observation showed that for a low inertial jet, the flow is likely to be laminar and there is no air entrainment (figure 4.8 (a)). With an increase of $Fr_D Fr_L$, an air bubble cluster is observed below the impact point inside the test pool. In figure 4.8 (b), at $Fr_D Fr_L = 1.1$, a diverging-converging shape is observed. At even higher $Fr_D Fr_L$, a triangular entrainment region is observed as shown in figure 4.8 (c). The outer bound of the bubble cluster is shown in the figure with a red line. The depth of the cluster is observed to be varied as a function of jet inertia as discussed later on. The transition between entrainment and no entrainment is not well defined and is prompt (Ervine et al. 1980; Harby et al. 2014). But it has been observed (discussed later) that entrainment height diminishes with $Fr_D Fr_L$ and there exists a critical $Fr_D Fr_L$ below which entrainment is not present. Assessment of this transition exactly in terms of $Fr_D Fr_L$ is quite difficult which requires precise control of

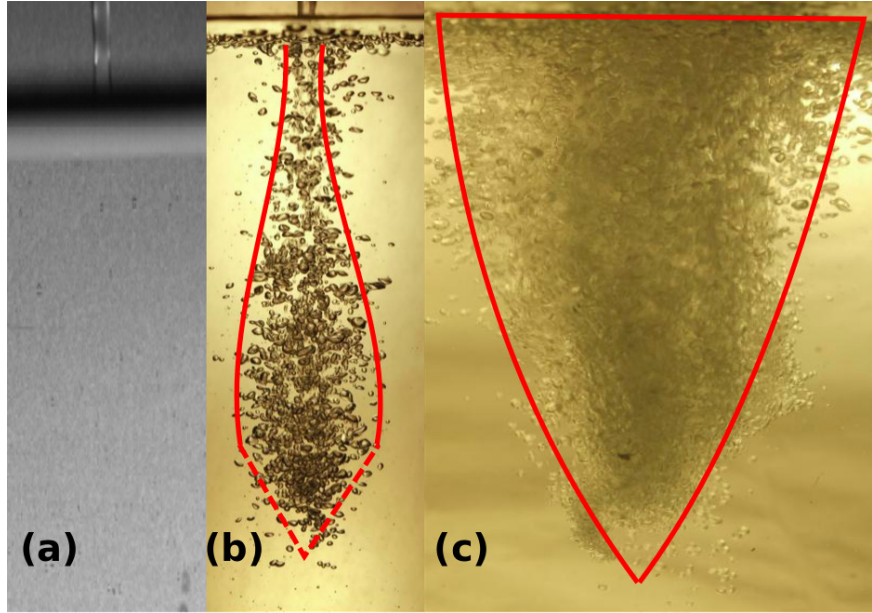


FIGURE 4.8: Possible outcomes as the jet impinges onto the pool: (a) No entrainment $Fr_D Fr_L = 0.125$, (b) Continuous Entrainment with diverging converging cluster $Fr_D Fr_L = 1.25$ and (c) Continuous Entrainment with triangular entrainment region $Fr_D Fr_L = 3.8$

flow rate. The present experimental setup is not equipped with such precision and therefore focus has been kept on the entrainment regime. But, [Harby et al. \(2014\)](#) have defined inception of entrainment as the entry of more than three bubbles in the liquid pool in three minutes and proposed inception velocity as a function of $\frac{l_j}{d_j}$. These isolated efforts showing no entrainment falls well within the limit mentioned by [Harby et al. \(2014\)](#). Based on present experimental efforts it can be ensured that for $Fr_D Fr_L$ less than 0.1 will not show any entrainment. For precise limit, one may follow limits proposed by [Harby et al. \(2014\)](#). Next, a subtle account of the onset of entrainment process is presented.

4.5 Onset of entrainment

To understand the two opposite possible outcomes mentioned above, the onset of entrainment is observed. Onset will be propagated or suppressed to reach either in the no entrainment or continuous entrainment scenario, respectively.

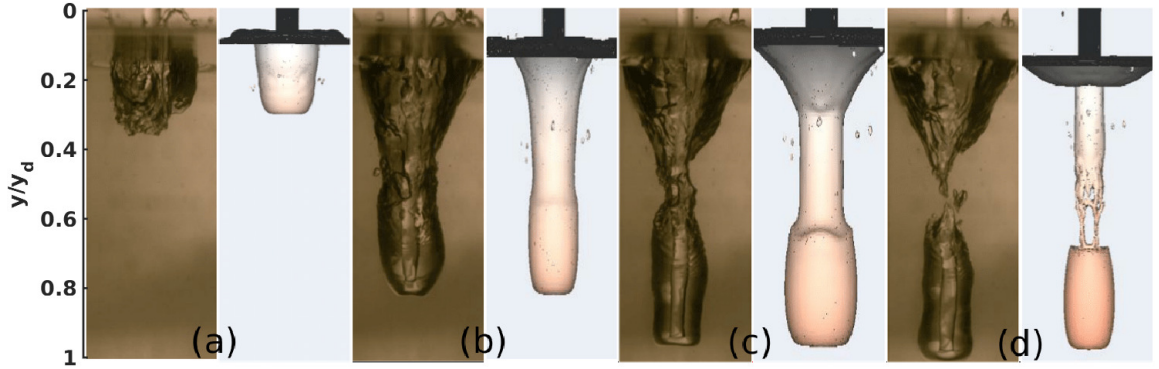


FIGURE 4.9: The temporal record of the onset of entrainment; (left: experimental and right: numerical) (a) Jet impacts the liquid pool and forms a cavity at $T = \frac{V_j t}{d_j} = 1$, (b) Elongation of the cavity formed at $T = 1.95$, (c) Necking of the elongated cavity at $T = 2.5$ as surface tension force tries to overcome jet's inertia and (d) Pinch off of the first annular air bubble at $T = 3.5$. ($Fr_D Fr_L = 2.2$).

4.5.1 Pinch-off of first annular bubble

Figure 4.9 consists of a detailed account of the jet - pool interaction from the point of impact to the point of pinch off. Both experimental snapshots and numerical tracer contours are shown side by side to establish the onset dynamics. As the jet strikes the liquid pool, a cavity is formed with the liquid core at the centerline surrounded by the air medium which by virtue of inertia penetrates inside resulting in the formation of a long cylinder. Surface tension and circulation surrounding the jet (as discussed later) results in necking which propagates further and pinches off as shown in figure 4.9 (d). The process has been studied from high-speed images in detail for the onset of entrainment for $Fr_D Fr_L = 1$ (figure 4.10). It can be observed from experiments that upon striking the free surface, due to inertia, jet creates a dimple and propagates downwards to form a cavity filled with air (figure 4.10 (a)). With time, the cavity enlarges (figure 4.10 (b) - 4.10 (e)) before surface tension becomes significant and starts contracting the cavity back to its original free surface. In the initial period, air cavity is formed as stepped cylinder with continuously decreasing diameter (figure 4.10 (a) - 4.10 (c)).

At a critical depth, surface tension starts dominating and cylinder turns into a sphere (figure 4.10 (d)) to initiate the contraction of the cavity. At this level, inertia gets weakened and surface tension starts dominating. Due to conversion of cylindrical cavity into spherical air mass (figure 4.10 (e)), pressure waves are generated which propagates in upward direction and contracts the stepped cylinder towards the jet (figure 4.10 (e) - 4.10 (f)), prompting collapse of the cavity. While the cavity is being collapsed, spherical air mass at the bottom of the cavity forms neck (figure 4.10 (e)) as a result of the higher amplitude

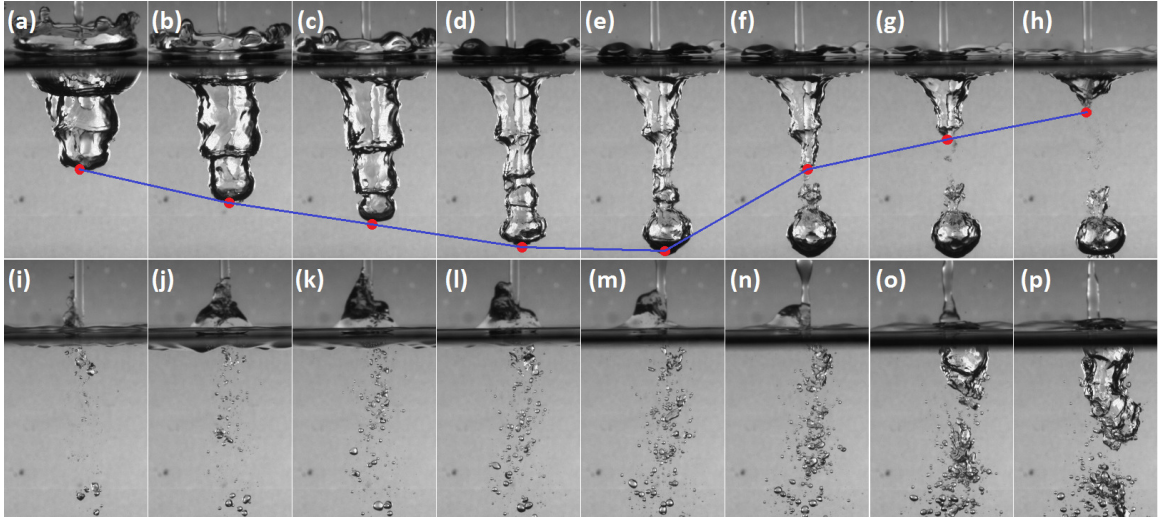


FIGURE 4.10: Experimental snapshots of pinch off for $Fr_D Fr_L = 1$ at $T =$ (a) 2.04, (b) 2.28, (c) 2.52, (d) 2.76, (e) 2.88, (f) 3, (g) 3.24, (h) 3.35, (i) 3.5, (j) 3.75, (k) 4, (l) 4.25, (m) 4.5, (n) 5, (o) 5.5 and (p) 6

of three-dimensional pressure waves. This leads towards pinching (figure 4.10 (f)) off the spherical bubble along with some satellites and retraction of rest cavity towards the free surface (figure 4.10 (f) - 4.10 (h)). The experiment shows that collapse of cavity generates an upward moving liquid jet (figure 4.10 (i)) thicker than the impinging one (figure 4.10 (j)). These two counteracting jets entrap air bubble in between them (figure 4.10 (k)). As the velocity of impinging jet is higher than the pressure wave jet, entrapped bubbles move down in the pool (figure 4.10 (k) - 4.10 (l)). With time, jet created by pressure wave falls down (figure 4.10 (m) - 4.10 (n)) and impinging jet starts second cycle of cavity formation (figure 4.10 (o)). The whole process repeats many times to entrap more and more bubbles (figure 4.10 (p)) and finally form a cluster as shown in experimental observation of figure 4.8 (c). The detached spherical bubble in each cycle comes back to the free surface and in its path, it dislodges daughters due to impact from bubbles in the cluster. At a lower value of the product of Froude numbers ($Fr_D Fr_L$), inertia never becomes dominated over surface tension and gravitational collapse strength to show all these sequences for the formation of the bubbly cluster. Impingement of jet at lower $Fr_L Fr_D$, creates a cavity but its propagation in the downward direction is suppressed and immediate collapse causes no entrainment of bubbles. But this requires further proof in future efforts.

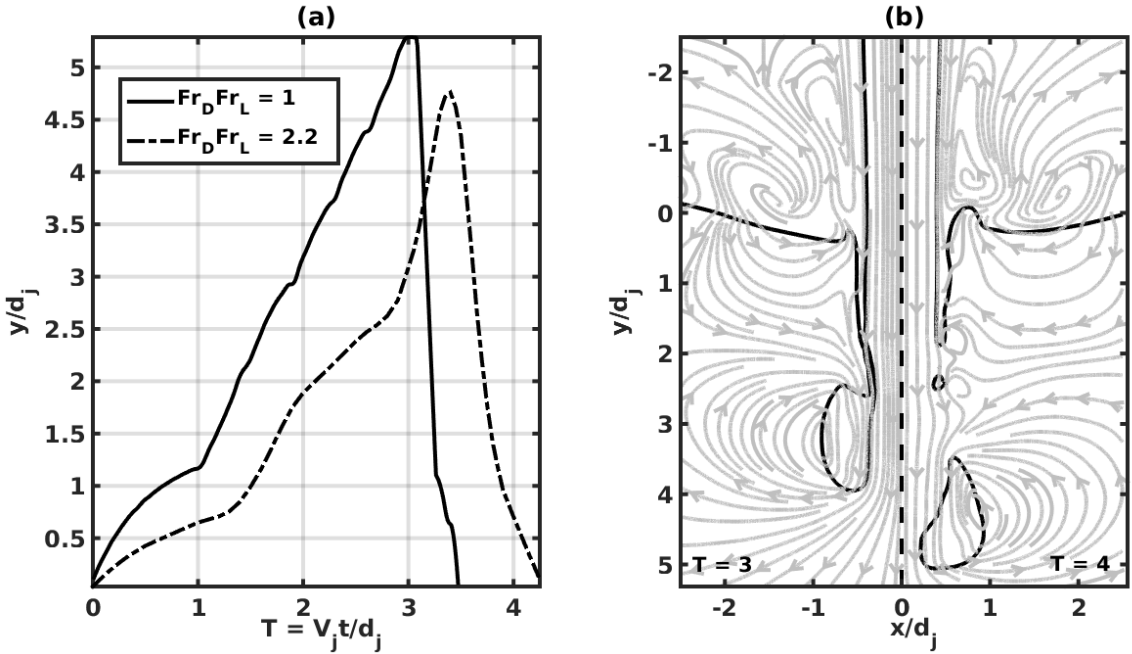


FIGURE 4.11: (a) Depth of penetration of liquid cavity formed during the impact of jet onto the pool and subsequent collapse of cavity. (b) Streamlines developed around the formed cavity before (on left) and after (on right) pinch off.

4.5.2 Dynamics of first pinch-off

One can clearly understand from the high-speed image sequences of figure 4.10 that during onset, the cavity collapses (surface tension driven) at a faster rate than formation (inertia dominated). Figure 4.11 (a) shows the maximum depth of the cavity with time as obtained from numerical simulations, for a complete cavity cycle. Initially, depth increases at a slower rate till pinch off of the bubble, as represented by steep fall in depth. Subsequently, the collapse of cavity occurs at a faster rate as shown in figure 4.11 (a). With the streamline field in figure 4.11 (b) obtained through numerical simulations, the dynamic process of pinch-off is studied. As the cylindrical cavity elongates (by virtue of jet's inertia) the surrounding air-sheath gets thinner and a region of high circulation is realized around the jet. As the jet tries to further elongate the cavity against the resistance of the pool, the developing circulations catapult the bubble and pinches it off from the thin air sheath. A look at the streamlines near the pool surface justifies the movement of the point of pinch-off towards the incoming jet as the cavity collapses back. As the cycle repeats, more bubbles are entrapped which ultimately leads to the formation of bubble cluster below the surface. Next, dynamic nature of the generated bubble cluster and characterize it based on the strength of the jet are illustrated.

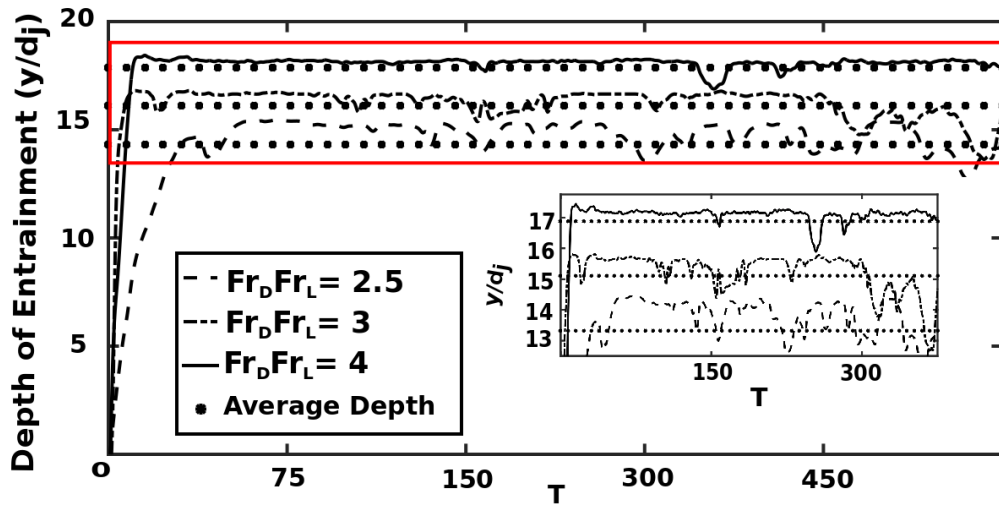


FIGURE 4.12: Temporal variation of maximum depth of entrainment. The inset figure takes a closer look at the variation of the height of entrainment, which pertains to a nearly constant value.

4.6 Dynamics of bubble cluster

In two-phase chemical reactors, the rate of reaction often depends on the available surface area in form of interfaces. Formation of bubbles inside the liquid pool increase this interfacial area and is responsible for the transfer of mass and energy through diffusion and advection. Therefore, it is pertinent to realize the characteristics of these bubble populations. The interaction between bubbles includes collision, coalescence, and dissociation. These processes lead to the formation of the bubble cluster which can be treated as a unique body whose dimensional characteristics are germane to the design of chemical reactors.

4.6.1 Attainment of quasi-steady bubble cluster

Once the cluster of different sized, shaped and interacting bubbles comes into existence, dynamics of an individual bubble is hard to follow. Overall nature of the bubble cluster remains almost same and the depth of entrainment attains a steady state value. In figure 4.12, from experimental observations, the variation of the depth of entrainment with time for different strengths ($Fr_D Fr_L$) of the jet is shown. Experimentally, after onset (increasing depth with time), saturation of depth is observed up-to a prolonged period. For different jet strengths, the average depth (with dots) which is in the range of saturation is also plotted. It shows that after onset, depth of entrainment is not a function of time, rather depends on the

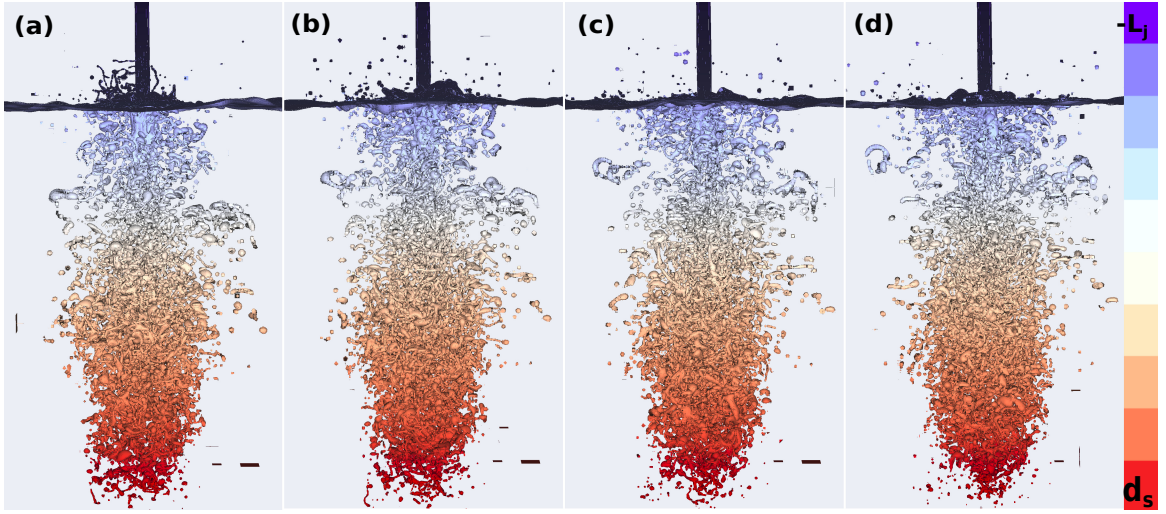


FIGURE 4.13: Attainment of steady state entrainment height for $Fr_D Fr_L = 4$ with the interface colored by the depth as measured from the liquid pool interface at $T =$ (a) 85, (b) 90, (c) 95 and (d) 100

strength of the impinging jet. This nature has been shown clearly in the inset of figure 4.12.

4.6.2 Characterization of bubble cluster

Steady penetration of entrainment inside pool is also confirmed by numerical simulations. In figure 4.13, detailed Volume of Fluid tracer colored using the distance from the liquid pool interface as the scalar has been shown. Numerical simulation shows that the depth of penetration of the bubble cluster pertains to a constant value as the time passes. Present numerical simulation matches well with the experimental observation here. In figure 4.12, experimentally, an increase of steady depth for three $Fr_D Fr_L$ is observed. Experimental and numerical snapshots of entrainment pattern at different $Fr_D Fr_L$ are shown in figure 4.14 to confirm the story of interface locations. From these photographic observations and numerical phase contours, one can observe that the entrained air penetration depth is proportional to $Fr_D Fr_L$. A complete range of depth (d_s) variation of entrainment from the free surface for a wide range of $Fr_D Fr_L$ is shown in figure 4.15. Both experimental and numerical data points are shown in figure 4.15. To express this increasing pattern of cluster depth as a function of $Fr_D Fr_L$, correlations (equation 4.3 for $\log(Fr_D Fr_L) < 1.2$ and equation 4.4 for $\log(Fr_D Fr_L) > 1.2$) with two empirical constants each in the form of a power law are proposed. The change in the behavior of the curves is because of the difference in entrainment cluster regimes as observed in figure 4.8. The empirical constants are fitted from experimental observations with Summed Square of Residue (SSE) equal to

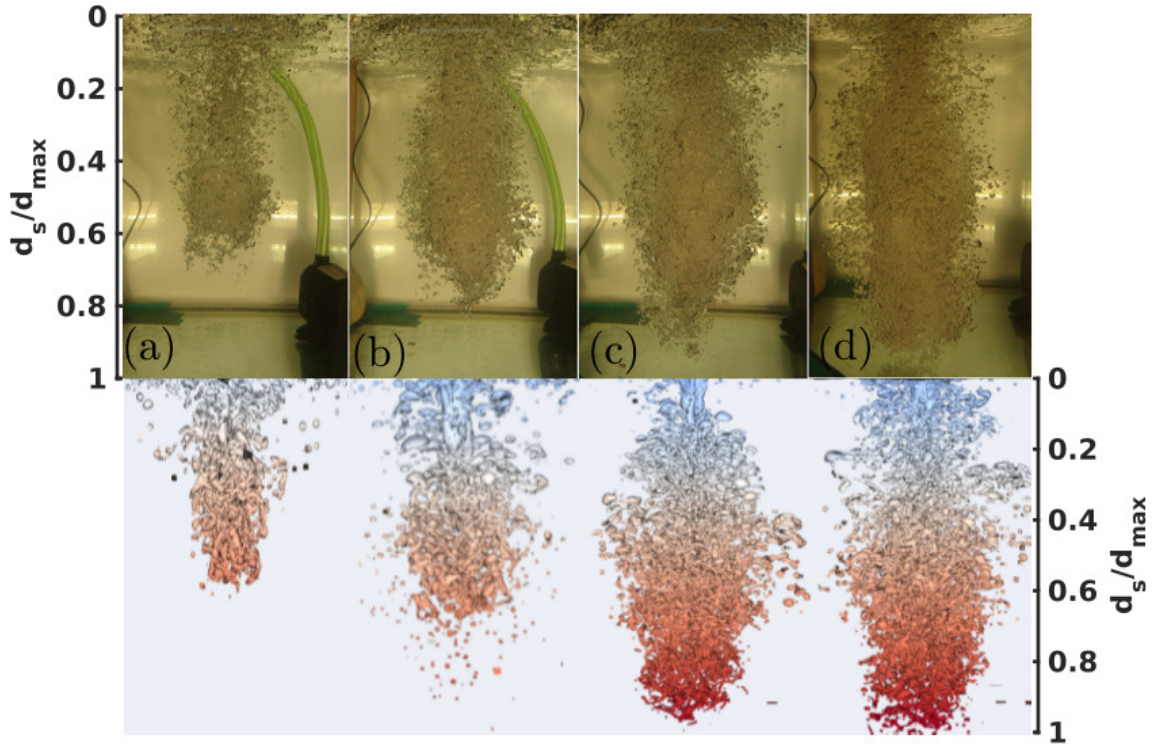


FIGURE 4.14: Steady entrainment pattern for $Fr_D Fr_L$ = (a) 1.4, (b) 2, (c) 3.25 and (d) 3.75

7.5×10^{-2} and 5×10^{-2} and R-square value as 0.9 and 0.95 respectively for equation 4.3 and 4.4.

$$\frac{ds}{dj} = 9.45(Fr_D Fr_L)^{0.33} \quad (4.3)$$

$$\frac{ds}{dj} = 3.3(Fr_D Fr_L)^{1.2} \quad (4.4)$$

To show the predictability of already available correlations against the experimental observations and establishment the improvement in prediction using equation (4.3-4.4), power law as proposed by [Ohkawa et al. \(1986\)](#) is also shown in Figure 4.15. Further, the volumetric strength of bubble cluster has been also observed to change with jet strength ($Fr_D Fr_L$) in Figure 4.14. The variation of the projected area of the cluster in a two-dimensional photographic plane along with the time at different jet strength is given. In Figure 4.16, projected area is plotted as a function of ($Fr_D Fr_L$) and time after post-processing the experimental data. One can clearly observe from this Figure that the projected area increases with $Fr_D Fr_L$ and time. Variation of the projected area with time can be attributed to the development of cluster initiating from the onset. On the other hand, the strength of inertia can be clearly seen from a higher projected area at strong jet than a weak one.

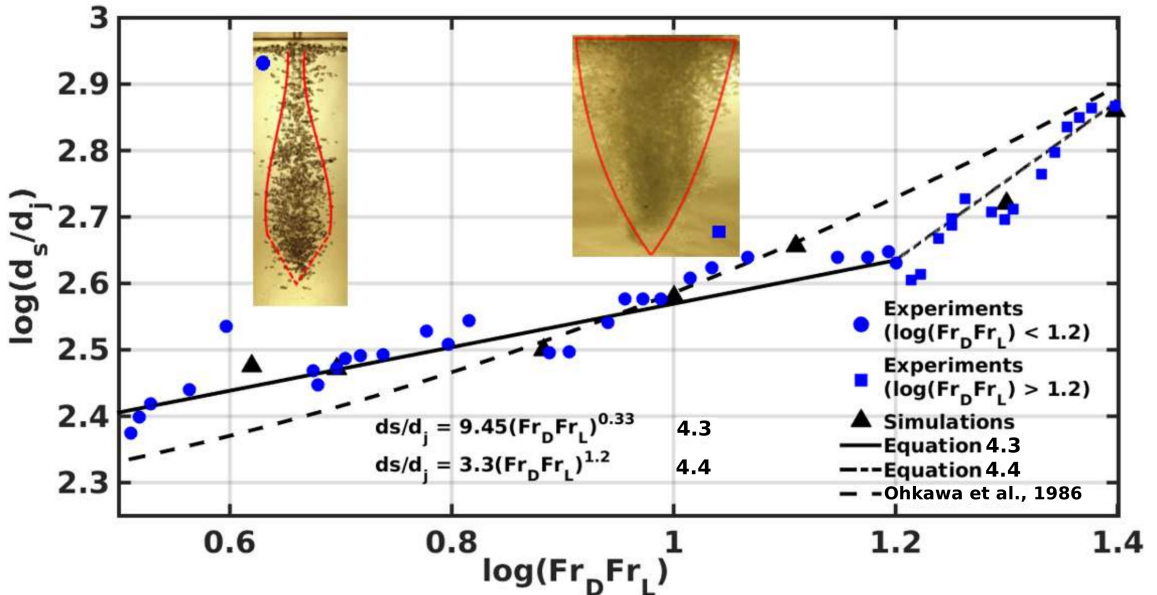


FIGURE 4.15: Steady state depth of entrainment as a function of the product of Froude numbers, $Fr_D Fr_L$; both experimental and numerical data points are mentioned.

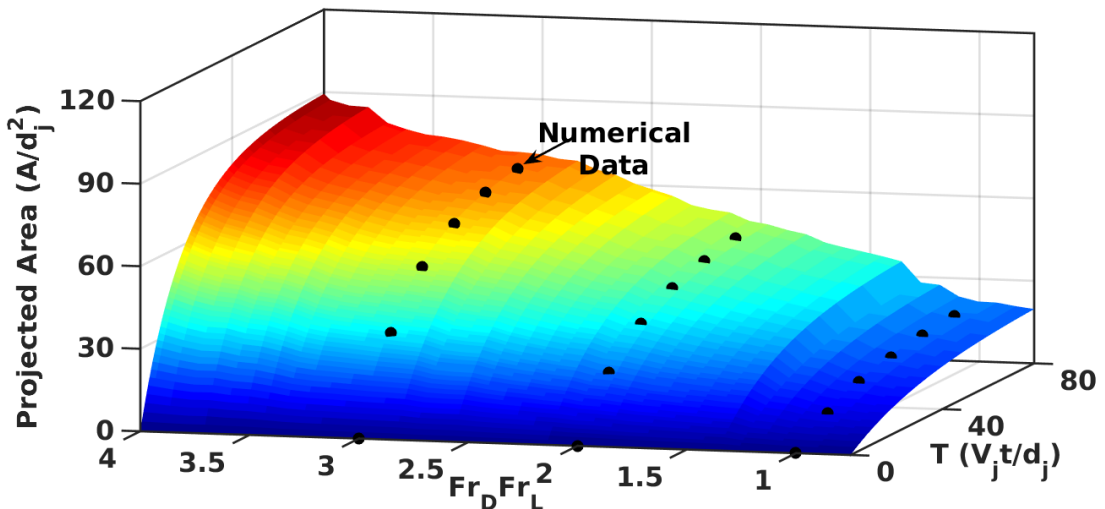


FIGURE 4.16: Projected area of the region affected by entrained bubble cluster; plane is constructed by experimental observations and numerical data points are shown by symbols.

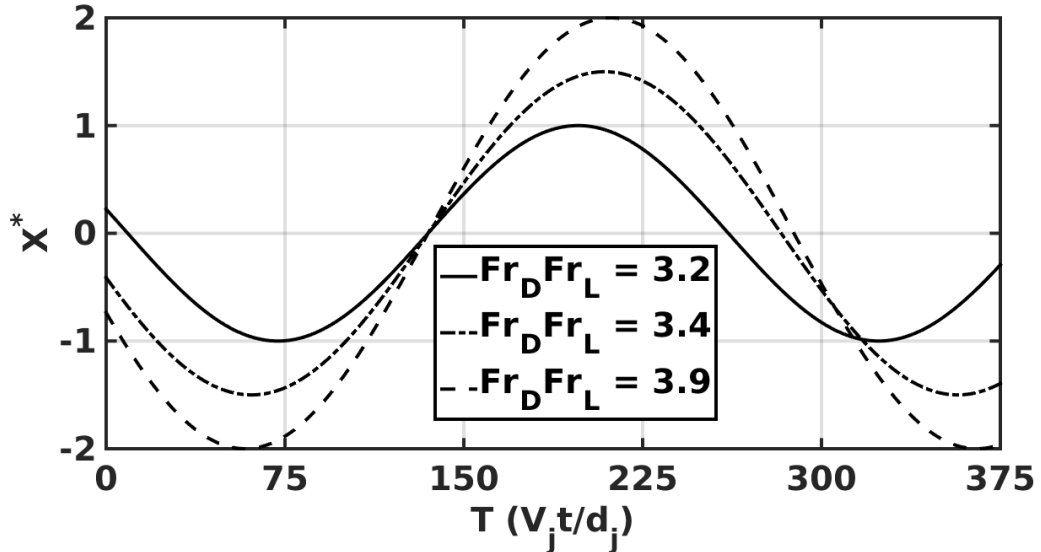


FIGURE 4.17: Temporal variation of the normalized abscissa of the centroid related to the entrainment cluster.

4.6.3 Kinematics of the cluster centroid

From a close look at experimental snaps, it has been observed that the centroid of the projected area (location x) shows periodic oscillation. Binary two-dimensional images, as shown in Figure 4.1 (b), are used to calculate the location of the centroid. Equation 4.5 is followed for calculation, where $\bar{x}(x_i, y_i)$ is the location of the pixel in the binary image corresponding to the cluster area (non-zero value) and N is the total number of non-zero pixels.

$$X_{centroid} = \frac{\int \bar{x} dA}{A} = \frac{\sum_{i=1}^N \bar{x}_i}{N} \quad (4.5)$$

Upon non-dimensionalizing with its mean and standard deviation as $X^* = \left(\frac{x - \text{mean}(x)}{\sigma_x} \right)$, the periodic movement as illustrated in equation 4.6 is obtained.

$$\frac{\partial^2 X^*}{\partial t^2} + \omega^2 X^* = 0 \quad (4.6)$$

Oscillations are observed in phases at all azimuthal planes. This represents the pseudo-randomness of the bubble cluster configuration having constant depth over time. As cluster is constructed by pinch off of bubbles from free surface, temporal dependence is not eliminated and became prompt in the lateral direction. From experimental observation, variation of X^* is obtained with non-dimensional time ($T = V_j t / d_j$) and plotted in Figure 4.17. The periodic nature is clearly depicted in Figure 4.17 having higher amplitude for lower

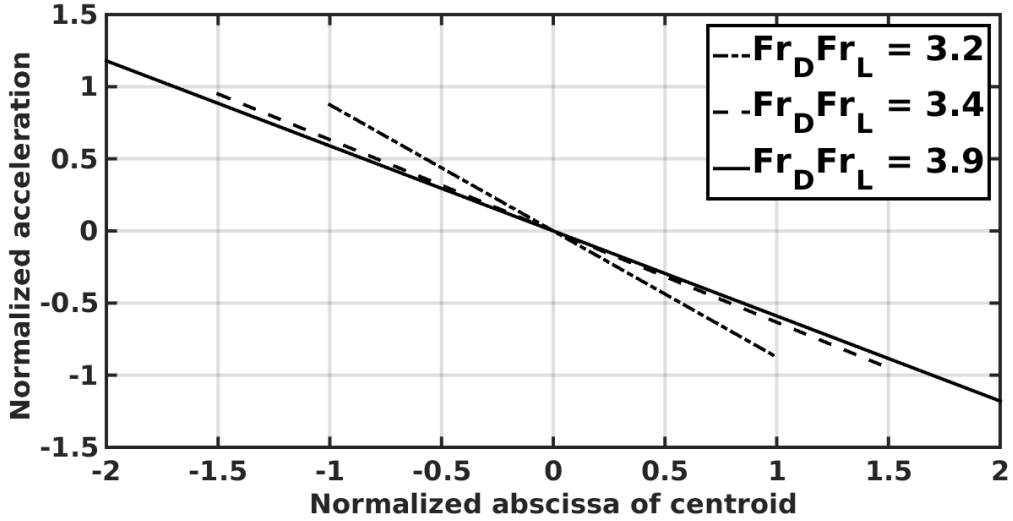


FIGURE 4.18: Variation of the acceleration of the centroid with its normalized abscissa related to the entrainment cluster.

$Fr_D Fr_L$. Increase of ω for lower $Fr_D Fr_L$ can also be seen from this figure as oscillation time periods for $Fr_D Fr_L = 3.2$ is lower than $Fr_D Fr_L = 3.9$. In equation 4.6, acceleration of centroid for the bubble cluster varies proportionally with its shift from the longitudinal jet plane. To depict that clearly, in Figure 4.18, normalized acceleration for different experimental conditions of $Fr_D Fr_L$ is shown. In all these cases, linear patterns have been observed confirming the validity of equation 4.6. At higher $Fr_D Fr_L$, it has been observed that the centroid acceleration increases and it deviates more from the jet plane. Acceleration of the centroid increases at a faster rate with shift from jet plane for lower $Fr_D Fr_L$ (resulting in higher proportionality constant ω^2 in equation 4.6).

Present experimental effort establishes the steady overall behavior of the cluster but keeps provision for monitoring the local behavior of bubbles. Next section targets towards an understanding of individual bubble dynamics with the help of visualization and signals from electrical conductivity probe.

4.7 Bubble kinematics

The bubble cluster consists different sized bubbles consistently making and breaking within the triangular entrainment region. The trajectory of a bubble is followed at a comparatively low-speed entrainment phenomenon from photographic observation in experiments and represented in Figure 4.19. After birth, the bubble moves downwards inside the cluster and reaches the maximum depth. It halts there for sometime before coming up from the other

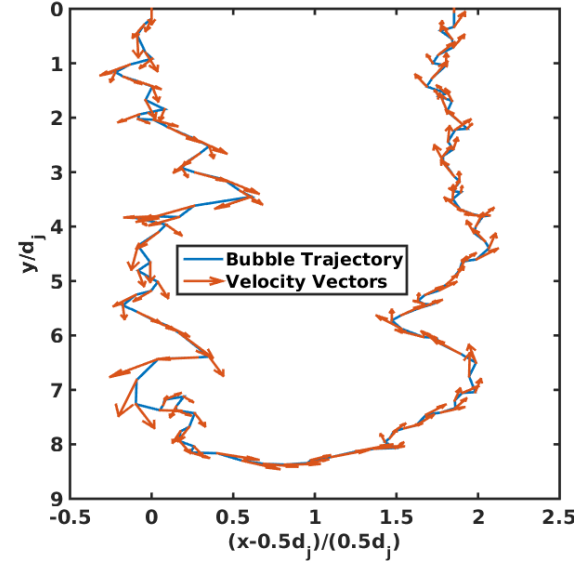


FIGURE 4.19: Bubble trajectory in the entrained region at $Fr_D Fr_L = 1.8$, as obtained from experimental observation. The bubble inception occurs at the tip of the thin air sheath, traverses through the entrainment region, stops the downward motion as the buoyancy dominates its motion and erupts back at the free surface.

side of the cluster. Its downward movement is driven by inertia and upward movement is due to buoyancy pull. Instantaneous velocity in the plot is also shown. In between initiation and collapse, the bubble is dominated by inertia, interaction and buoyancy pull inside the cluster (Figure 4.19).

Electrical conductivity probe signals have been recorded for varying flow rates and different lengths of jets inside the bubble entrainment zone. The physical illustration of the voltage signal is shown in Figure 4.2. The sharp downfalls represent the presence of bubbles. A representative signal of probes in the experimental cluster is shown in the inset of Figure 4.20. Even though the voltage signal, which varies in between 3.5 to 1.5 volts, clearly depicts the presence of entrapped air bubbles, it is difficult to get any kinematic inference. Therefore, from raw electrical signals, probability density function (PDF) has been plotted for three representative flow-rates in Figure 4.20. The peak in PDF shifts to the left and lowers down as the flow rate increases. The probability of getting lower voltage signifies vigorous cluster characteristics and high probability of bubble presence at a given spatial coordinate. With an increase in jet flow-rate, entrainment strength increases and causes peak at the lower voltage. This shows more and more bubbles are being trapped due to its random presence in the cluster at higher flow rates. This clearly demonstrates the bubble kinematics as well as cluster vibrations. Signals of probe confirm the presence of a bubble in the cluster and its peak of PDF at lower value signifies higher mobility of

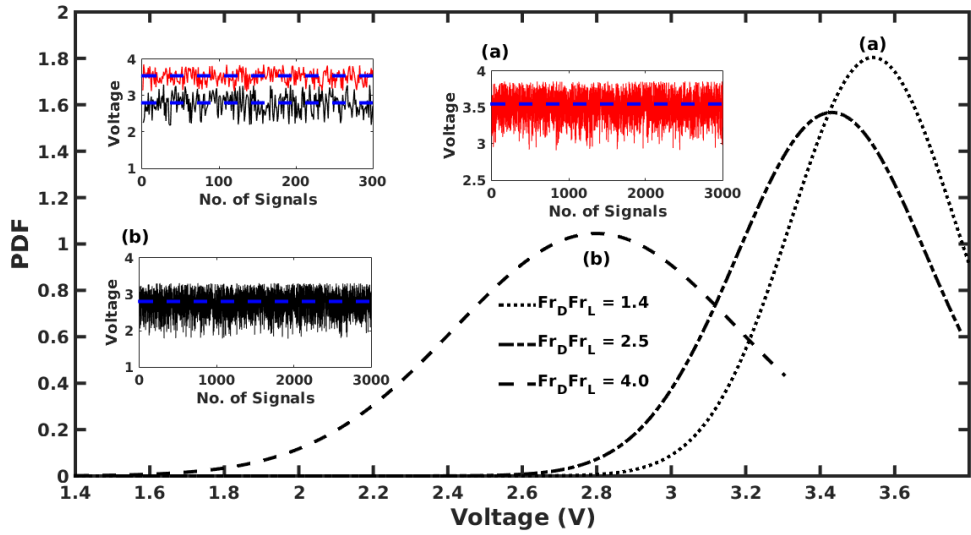


FIGURE 4.20: Characteristic probability density function of the experimental probe signals at different values of Fr_DFr_L . More the peak is shifted towards the left, the high density of bubbles are present at the spatial location of the electrodes.

bubbles at the cluster. At lower jet speed bubbles are produced but exhibit comparative calm behavior to have a liquid contact at the probe tip. On the other hand, at high jet speed, random motion of the generated bubble keeps always gaseous phase in contact with the probe. Present observation establishes highly random kinematic behavior at high jet speed.

4.8 Summary

Impingement of water jet on a pool is studied using full-scale experiments and detailed numerical simulation. High-speed imaging and electrical conductivity probes are used in experimental instrumentation. Depending on jet's strength, two opposite regimes have been identified as no entrainment and conical bubble cluster. Formation of inertia dominated cavity and surface tension dominated collapse have been identified as the basic consequences of the onset of bubble entrainment as a cluster. Repetitive formation and breakage of air cavity in the pool results in disconnected but interacting bubble population. The mutual interplay between inertia and surface tension determines the depth of entrained region which has been reported as a function of the product of Froude Numbers (Fr_DFr_L) in two correlations for different regimes with the boundary at $Fr_DFr_L = 1.2$. Proposed correlation shows accurate prediction (R-squared of 0.9 and 0.95) of depth for a wide range of jet diameters and heights. Using high-speed images, increasing projected area of entrainment has been observed for higher Fr_DFr_L and time which establishes the affected zone during

entrainment. Kinematics of entrainment has been studied using a spatio-temporal variation of centroid location of the cluster. Acceleration of the centroid is found to be linearly varying with the deviation of the entrained region from the plane of jet impact. The trajectory of a single bubble has been also reported in the study from visualization to establish formation, downward traverse, stabilized floating at critical height, buoyancy-driven approach towards free surface and collapse in its whole life cycle.

Chapter 5

Conclusion and Scope of Future Work

Combined experimental and numerical study has been performed to understand the dynamics of the interacting jets, and consequences of jet-pool impingement. Following categorical conclusion can be made from the present study.

5.1 Salient features and key findings

5.1.1 Collision of liquid jets

The stable chain structures are formed by the collision of laminar liquid jets when the inertia forces are, in order of magnitude, similar to the surface tension forces. A series of fully resolved detailed numerical simulations are performed to get the following conclusions:

- The individual links, formed by collision of cylindrical jets (primary) or rims (secondary onward), occupy mutually orthogonal planes with a successive reduction in size owing to viscous effects.
- The variation of the velocity field across the radial coordinate is found to be negligible whereas the azimuthal variation of the sheet velocity is scaled using its average, given by an empiric relation. At the collision planes, the velocity field is found to be retracting in the direction of the colliding jets and rims whereas it is expanding in the plane of the formed sheets.
- The inertial and gravitational forces provide a measure of the expansion of these sheets counteracted by the surface tension at the interface and viscous dissipations at the subsequent collisions. An increase in the impingement angle (α) leads to wider links of the chain with a negligible change in the length of individual links. Intuitively, the size of the stable chain structure increases with an increase in the momenta of the jets (Fr) or with a decrease in the strength of the surface tension force (increasing Bo). Increase in the Re presents a sharp increase in the dimensions of the chain, which saturates at the higher values of Re .
- The individual symmetric sheet profile can be modeled using a third order polynomial, with an accuracy of $\pm 5\%$, with coefficients dependent on various non-dimensional numbers featuring the interplay of different forces.
- An analytical model is developed by considering the fundamental forces of gravity and surface tension lead to the formulation of the sheet profile using only one free parameter which has been empirically related to the flow variables.

- Higher order links are found to be similar to lower or primary level element formed due to impact between jets of reduced Fr and α .

5.1.2 Air entrainment by impingement of liquid jet on a pool

- Entrainment of air bubbles due to impingement of liquid jet onto a pool has been modeled successfully using numerical simulations. This numerical model is validated with one to one correspondence with the experimental results. This cross-validation is done for the inception dynamics and pinch-off of the first annular bubble as well as the characteristics of bubble cluster.
- Depending on jet's strength, two opposite regimes have been identified as no entrainment and one with full-fledged bubble cluster. The latter is further categorized into two groups, namely, continuous entrainment with diverging-converging cluster for $Fr_D Fr_L < 1.2$ and continuous entrainment with triangular cluster for $Fr_D Fr_L > 1.2$.
- The inception of bubble entrainment consists of inertia influenced cavity formation and surface tension dominated collapse.
- The initial transients of bubble entrainment inception is tracked using high-speed imaging and numerical simulations. A quasi-steady state of the process is reached which has been used to study bubble cluster characteristics.
- With R-squared values of 0.9 and 0.95, the entrained cluster depth of penetration is correlated with the inertial strength of liquid jet for two distinct full-fledged entrainment cluster regimes.
- Centroid of the bubble cluster is tracked using in-house image processing code. The spatio-temporal variation of centroid location leads to a linear relationship between its acceleration and its deviation from the plane of jet impact. This accounts for the observed oscillations of the bubble cluster, whose time-period increases with the inertial strength of the liquid jet.
- Trajectory of a single bubble has been also studied to establish formation, downward traverse, stabilized floating at critical height, buoyancy-driven approach towards free surface and collapse in its whole life cycle.

5.2 Scope of future work

After a detailed study of the interaction between symmetric jets for the formation of a liquid chain-like structure and normal impingement of jet in a pool following topics can be identified as potential directions for future research:

1. Dynamics of jet interactions at higher Re may lead to the flapping of sheet, fragmentation, and atomization. A detailed experimental and numerical study can be performed to understand these rich fluidic physics.
2. Moreover, impingement between two asymmetric jets can lead towards complex liquid structures and such occurrences are quite relevant for industrial applications. A detailed study can be targeted towards that direction.
3. It will be also interesting to see the interaction between jet and sheet or sheets to have a three-dimensional mesmerizing fluidic structure. Study of such topics will be quite useful for batch processing of different chemical reactors and spray jet cooling technique.
4. Impingement of inclined jets in a pool can be readily observed in impingement cooling systems which will be an extension of present understanding of orthogonal jet impingement in a pool. A natural extension of the present work can be an experimental and numerical observation of entrained cluster under inclined impingement.
5. Cluster-cluster interaction during side by side impingement of jets in a pool can be also studied from the same setup developed in the present study. It will give insights towards population interactions between bubbles swarms.
6. Last but not the least, the bubble entrainment cluster penetrating through multiple layer liquid stratification may lead to the presence of complex multiphase situations. The study will be quite rich in fluid dynamics as the interaction between different scale and phases are involved.

References

- Agbaglah, Gilou, Thoraval, M-J, Thoroddsen, Sigurdur T, Zhang, Li V, Fezzaa, Kamel, & Deegan, Robert D (2015). “Drop impact into a deep pool: vortex shedding and jet formation”. *Journal of fluid mechanics* 764.
- Baek, Seungho & Han, JungHyun (2017). “Simulation of thin liquid jets with threads”. *Computer Animation and Virtual Worlds* 28.3-4, pp. 1–14.
- Bagatur, T. (2014). “Experimental Analysis of Flow Characteristics from Different Circular Nozzles at Plunging Water Jets”. *Arabian Journal for Science and Engineering* 39.4, pp. 2707–2719.
- Belden, J., Ravela, S., Truscott, T. T., & Techet, A. H. (2012). “Three-dimensional bubble field resolution using synthetic aperture imaging: application to a plunging jet”. *Experiments in fluids* 53.3, pp. 839–861.
- Bell, J. B., Colella, P., & Glaz, H. M. (1989). “A second-order projection method for the incompressible Navier-Stokes equations”. *Journal of Computational Physics* 85.2, pp. 257–283.
- Bergles, E & Ma, C-F (1983). “Boiling jet impingement cooling of simulated microelectronic chips”. *Heat Transfer in Electronic Equipment-1983*, pp. 5–12.
- Bin, A. K. (1988). “Gas entrainment by plunging liquid jets”. *Forschung im Ingenieurwesen* 54.4, pp. 136–136.
- Biń, A. K. (1993). “Gas entrainment by plunging liquid jets”. *Chemical Engineering Science* 48.21, pp. 3585–3630.
- Bonetto, F. & Lahey, R. T. (1993). “An experimental study on air carryunder due to a plunging liquid jet”. *International Journal of Multiphase Flow* 19.2, pp. 281–294.
- Brackbill, JU, Kothe, Douglas B, & Zemach, Charles (1992). “A continuum method for modeling surface tension”. *Journal of computational physics* 100.2, pp. 335–354.

Bremond, N. & Villermaux, E. (2006). “Atomization by jet impact”. *Journal of Fluid Mechanics* 549, pp. 273–306.

Brouilliot, D. & Lubin, P. (2013). “Numerical simulations of air entrainment in a plunging jet of liquid”. *Journal of Fluids and Structures* 43, pp. 428–440.

Bush, J. W. M. & Hasha, A. E. (2004). “On the collision of laminar jets: fluid chains and fishbones”. *Journal of Fluid Mechanics* 511, pp. 285–310.

Chanson, H. (1996). *Air bubble entrainment in free-surface turbulent shear flows*. Academic Press.

Chanson, H. & Cummings, P. D. (1994). “An experimental study on air carryunder due to a plunging liquid jet”. *International journal of multiphase flow* 20.3, pp. 667–670.

Chanson, H., Aoki, S., & Hoque, A. (2004). “Physical modelling and similitude of air bubble entrainment at vertical circular plunging jets”. *Chemical engineering science* 59.4, pp. 747–758.

Chen, F. & Hagen, H. (2011a). “A Survey of Interface Tracking Methods in Multi-phase Fluid Visualization”. *Visualization of Large and Unstructured Data Sets - Applications in Geospatial Planning, Modeling and Engineering (IRTG 1131 Workshop)*. Vol. 19. OpenAccess Series in Informatics (OASIcs). Schloss Dagstuhl–Leibniz-Zentrum fuer Informatik, pp. 11–19.

Chen, Fang & Hagen, Hans (2011b). “A survey of interface tracking methods in multi-phase fluid visualization”. *OASIcs-OpenAccess Series in Informatics*. Vol. 19. Schloss Dagstuhl–Leibniz-Zentrum fuer Informatik.

Chen, Kai, Jiang, Pei-Xue, Chen, Jian-Nan, & Xu, Rui-Na (2018). “Numerical investigation of jet impingement cooling of a flat plate with carbon dioxide at supercritical pressures”. *Heat Transfer Engineering* 39.2, pp. 85–97.

Chen, X., Ma, D., Yang, V., & Popinet, S. (2013). “High-fidelity simulations of impinging jet atomization”. *Atomization and Sprays* 23.12.

Choo, Y. J. & Kang, B. S. (2001). “Parametric study on impinging-jet liquid sheet thickness distribution using an interferometric method”. *Experiments in Fluids* 31.1, pp. 56–62.

- Choo, Y. J. & Kang, B. S. (2002). “The velocity distribution of the liquid sheet formed by two low-speed impinging jets”. *Physics of Fluids* 14.2, pp. 622–627.
- Choo, Y. J. & Kang, B. S. (2007). “The effect of jet velocity profile on the characteristics of thickness and velocity of the liquid sheet formed by two impinging jets”. *Physics of Fluids* 19.11, p. 112101.
- Chorin, A. J. (1968). “Numerical solution of the Navier-Stokes equations”. *Mathematics of Computation* 22.104, pp. 745–762.
- Clanet, C. & Lasheras, J. C. (1997). “Depth of penetration of bubbles entrained by a plunging water jet”. *Physics of Fluids (1994-present)* 9.7, pp. 1864–1866.
- Clanet, C. & Villermaux, E. (2002). “Life of a smooth liquid sheet”. *Journal of fluid mechanics* 462, pp. 307–340.
- Cummings, P. D. & Chanson, H. (1998). “Individual Air Bubble Entrapment at a Planar Plunging Jet With Near-Inception Flow Conditions”. *Proceedings, 13th Australasian Fluid Mechanics Conference*, pp. 13–18.
- Cummings, P. D. & Chanson, H. (1999). “An experimental study of individual air bubble entrainment at a planar plunging jet”. *Chemical Engineering Research and Design* 77.2, pp. 159–164.
- Da, F., Hahn, D., Batty, C., Wojtan, C., & Grinspun, E. (2016). “Surface-only liquids”. *ACM Transactions on Graphics (TOG)* 35.4, p. 78.
- Da Vinci, Leonardo (1508). “The Notebooks of Leonardo da Vinci”. *Trans: E MacCurdy, (New York: George Brazillier)*, p. 756.
- Deshpande, S. S. & Trujillo, M. F. (2013). “Distinguishing features of shallow angle plunging jets”. *Physics of Fluids (1994-present)* 25.8, p. 082103.
- Deshpande, Suraj S, Trujillo, Mario F, Wu, Xiongjun, & Chahine, Georges (2012). “Computational and experimental characterization of a liquid jet plunging into a quiescent pool at shallow inclination”. *International Journal of Heat and Fluid Flow* 34, pp. 1–14.

- Detsch, R. M. & Sharma, R. N. (1990). “The critical angle for gas bubble entrainment by plunging liquid jets”. *The Chemical Engineering Journal* 44.3, pp. 157–166.
- Donk, J A C Van de, Lans, R G J M Van der, & Smith, John M (1979). “Effect of contaminants on the oxygen transfer rate achieved with a plunging jet contactor”. *Proceedings of the 3rd European Conference on Mixing, York*, pp. 4–6.
- Driessens, Theo, Sleutel, Pascal, Dijksman, Frits, Jeurissen, Roger, & Lohse, Detlef (2014). “Control of jet breakup by a superposition of two Rayleigh–Plateau-unstable modes”. *Journal of fluid mechanics* 749, pp. 275–296.
- Duchemin, L., Popinet, S., Josserand, C., & Zaleski, S. (2002). “Jet formation in bubbles bursting at a free surface”. *Physics of Fluids (1994-present)* 14.9, pp. 3000–3008.
- Durve, A. P. & Patwardhan, A. W. (2012). “Numerical and experimental investigation of onset of gas entrainment phenomenon”. *Chemical engineering science* 73, pp. 140–150.
- Eggers, J. & Villermaux, E. (2008). “Physics of liquid jets”. *Reports on Progress in Physics* 71.3, p. 036601.
- Ekimova, M., Quevedo, W., Faubel, M., Wernet, P., & Nibbering, E. T. J. (2015). “A liquid flatjet system for solution phase soft-x-ray spectroscopy”. *Structural Dynamics* 2.5, p. 054301.
- El Hammoumi, M., Achard, J. L., & Davoust, L. (2002). “Measurements of air entrainment by vertical plunging liquid jets”. *Experiments in fluids* 32.6, pp. 624–638.
- Erni, P. & Elabbadi, A. (2013). “Free impinging jet microreactors: controlling reactive flows via surface tension and fluid viscoelasticity”. *Langmuir* 29.25, pp. 7812–7824.
- Ervine, D. A., McKeogh, E., & Elsawy, E. M. (1980). “Effect of turbulence intensity on the rate of air entrainment by plunging water jets.” *Proceedings of the Institution of Civil Engineers* 69.2, pp. 425–445.
- Evans, G. M., Jameson, G. J., & Rielly, C. D. (1996). “Free jet expansion and gas entrainment characteristics of a plunging liquid jet”. *Experimental Thermal and Fluid Science* 12.2, pp. 142–149.

- Fetisov, Y. M. (1996). “Experimental investigations of the conditions of the onset of air entrainment by plunging liquid jets”. *Power Technology and Engineering (formerly Hydrotechnical Construction)* 30.2, pp. 87–91.
- Francois, Marianne M, Cummins, Sharen J, Dendy, Edward D, Kothe, Douglas B, Sicilian, James M, & Williams, Matthew W (2006). “A balanced-force algorithm for continuous and sharp interfacial surface tension models within a volume tracking framework”. *Journal of Computational Physics* 213.1, pp. 141–173.
- Fuster, D., Matas, J-P., Marty, S., Popinet, S., Hoepffner, J., Cartellier, A., & Zaleski, S. (2013). “Instability regimes in the primary breakup region of planar coflowing sheets”. *Journal of Fluid Mechanics* 736, pp. 150–176.
- Goldring, B. T., Mawer, W. T., & Thomas, N. (1980). “Level surges in the circulating water downshaft of large generating stations”. *Proc. 3rd Intl Conf. on Pressure Surges*, pp. 279–300.
- Harby, K., Chiva, S., & Muñoz-Cobo, J. L. (2014). “An experimental study on bubble entrainment and flow characteristics of vertical plunging water jets”. *Experimental Thermal and Fluid Science* 57, pp. 207–220.
- Hasson, D. & Peck, R. E. (1964). “Thickness distribution in a sheet formed by impinging jets”. *AICHE Journal* 10.5, pp. 752–754.
- Hoeve, Wim van, Gekle, Stephan, Snoeijer, Jacco H, Versluis, Michel, Brenner, Michael P, & Lohse, Detlef (2010). “Breakup of diminutive Rayleigh jets”. *Physics of fluids* 22.12, p. 122003.
- Ibrahim, E. A. & Przekwas, A. J. (1991). “Impinging jets atomization”. *Physics of Fluids A: Fluid Dynamics* 3.12, pp. 2981–2987.
- Inamura, T. & Shirota, M. (2014). “Effect of velocity profile of impinging jets on sheet characteristics formed by impingement of two round liquid jets”. *International Journal of Multiphase Flow* 60, pp. 149–160.
- Inoue, C., Watanabe, T., & Himeno, T. (2008). “Study on atomization process of liquid sheet formed by impinging jets”. *44th AIAA/ASME/SAE/ASEE Joint Propulsion Conference & Exhibit*, p. 4847.

- Inoue, C., Watanabe, T., & Himeno, T. (2009). “Liquid sheet dynamics and primary breakup characteristics at impingement type injector”. *45th AIAA/ASME/SAE/ASEE Joint Propulsion Conference & Exhibit*, p. 5041.
- Jian, Z., Josserand, C., Popinet, S., Ray, P., & Zaleski, S. (2018). “Two mechanisms of droplet splashing on a solid substrate”. *Journal of Fluid Mechanics* 835, pp. 1065–1086.
- Kate, RP, Das, PK, & Chakraborty, Suman (2007). “Hydraulic jumps due to oblique impingement of circular liquid jets on a flat horizontal surface”. *Journal of Fluid Mechanics* 573, pp. 247–263.
- Kersten, B., Ohl, C. D., & Prosperetti, A. (2003). “Transient impact of a liquid column on a miscible liquid surface”. *Physics of Fluids (1994-present)* 15.3, pp. 821–824.
- Kiger, Kenneth T & Duncan, James H (2012). “Air-entrainment mechanisms in plunging jets and breaking waves”. *Annual Review of Fluid Mechanics* 44, pp. 563–596.
- Koralek, Jake D, Kim, Jongjin B, Bruza, Petr, Curry, Chandra B, Chen, Zhijiang, Bechtel, Hans A, Cordones, Amy A, Sperling, Philipp, Toleikis, Sven, Kern, Jan F, et al. (2018). “Generation and characterization of ultrathin free-flowing liquid sheets”. *Nature communications* 9.1, p. 1353.
- Kumar, P., Das, A. K., & Mitra, S. K. (2016). “Physical understanding of gas-liquid annular flow and its transition to dispersed droplets”. *Physics of Fluids* 28.7, p. 072101.
- Kumar, P., Das, A. K., & Mitra, S. K. (2017a). “Air entrainment driven by a converging rotational field in a viscous liquid”. *Physics of Fluids* 29.10, p. 102104.
- Kumar, P., Das, A. K., & Mitra, S. K. (2017b). “Bending and growth of entrained air filament under converging and asymmetric rotational fields”. *Physics of Fluids* 29.2, p. 022101.
- Lhuissier, H. & Villermaux, E. (2011). “The destabilization of an initially thick liquid sheet edge”. *Physics of Fluids* 23.9, p. 091705.
- Lin, T. J. & Donnelly, H. G. (1966). “Gas bubble entrainment by plunging laminar liquid jets”. *AICHE Journal* 12.3, pp. 563–571.

- Ling, Y., Zaleski, S., & Scardovelli, R. (2015). “Multiscale simulation of atomization with small droplets represented by a Lagrangian point-particle model”. *International Journal of Multiphase Flow* 76, pp. 122–143.
- Lord Rayleigh (1879). “On the capillary phenomena of jets”. *Proceedings of the Royal Society of London* 29.196-199, pp. 71–97.
- Lord Rayleigh (1889). “On the tension of recently formed liquid surfaces”. *Proceedings of the Royal Society of London* 47.286-291, pp. 281–287.
- Ma, Jingsen, Oberai, Assad A, Drew, Donald A, Lahey Jr, Richard T, & Hyman, Mark C (2011). “A comprehensive sub-grid air entrainment model for RaNS modeling of free-surface bubbly flows”. *The Journal of Computational Multiphase Flows* 3.1, pp. 41–56.
- Ma, Jingsen, Oberai, Assad A, Drew, Donald A, & Lahey, Richard T (2012). “A Two-Way Coupled Polydispersed Two-Fluid Model for the Simulation of Air Entrainment Beneath a Plunging Liquid Jet”. *Journal of fluids engineering* 134.10, p. 101304.
- Martin, Holger (1977). “Heat and mass transfer between impinging gas jets and solid surfaces”. *Advances in heat transfer*. Vol. 13. Elsevier, pp. 1–60.
- Matas, Jean-Philippe & Cartellier, Alain (2013). “Flapping instability of a liquid jet”. *Comptes Rendus Mécanique* 341.1-2, pp. 35–43.
- Matas, Jean-Philippe, Marty, Sylvain, & Cartellier, Alain (2011). “Experimental and analytical study of the shear instability of a gas-liquid mixing layer”. *Physics of fluids* 23.9, p. 094112.
- McKeogh, E. J. & Ervine, D. A. (1981). “Air entrainment rate and diffusion pattern of plunging liquid jets”. *Chemical Engineering Science* 36.7, pp. 1161–1172.
- Oguz, H. N., Prosperetti, A., & Lezzi, A. M. (1992). “Examples of air-entraining flows”. *Physics of Fluids A: Fluid Dynamics (1989-1993)* 4.4, pp. 649–651.
- Ohkawa, A., Kusabiraki, D., Kawai, Y., Sakai, N., & Endoh, K. (1986). “Some flow characteristics of a vertical liquid jet system having downcomers”. *Chemical Engineering Science* 41.9, pp. 2347–2361.

- Popinet, S. (2003). “Gerris: a tree-based adaptive solver for the incompressible Euler equations in complex geometries”. *Journal of Computational Physics* 190.2, pp. 572–600.
- Popinet, S. (2009). “An accurate adaptive solver for surface-tension-driven interfacial flows”. *Journal of Computational Physics* 228.16, pp. 5838–5866.
- Qu, X., Goharzadeh, A., Khezzar, L., & Molki, A. (2013). “Experimental characterization of air-entrainment in a plunging jet”. *Experimental Thermal and Fluid Science* 44, pp. 51–61.
- Qu, X. L., Khezzar, L., Danciu, D., Labois, M., & Lakehal, D. (2011). “Characterization of plunging liquid jets: A combined experimental and numerical investigation”. *International Journal of Multiphase Flow* 37.7, pp. 722–731.
- Renardy, Yuriko & Renardy, Michael (2002). “PROST: a parabolic reconstruction of surface tension for the volume-of-fluid method”. *Journal of computational physics* 183.2, pp. 400–421.
- Roy, A. K., Maiti, B., & Das, P. K. (2013). “Visualisation of air entrainment by a plunging jet”. *Procedia Engineering* 56, pp. 468–473.
- Sande, E. Van de & Smith, J. M. (1976). “Jet break-up and air entrainment by low velocity turbulent water jets”. *Chemical Engineering Science* 31.3, pp. 219–224.
- Sene, K. J. (1988). “Air entrainment by plunging jets”. *Chemical Engineering Science* 43.10, pp. 2615–2623.
- Shen, Y. B. & Poulikakos, D. (1998). “Thickness variation of a liquid sheet formed by two impinging jets using holographic interferometry”. *ASME Journal of Fluids Engineering* 120.3, pp. 482–487.
- Singh, Digvijay & Das, Arup Kumar (2018). “Computational Simulation of Radially Asymmetric Hydraulic Jumps and Jump-Jump Interactions”. *Computers & Fluids*.
- Soh, W. K., Khoo, B. C., & Yuen, W. Y. D. (2005). “The entrainment of air by water jet impinging on a free surface”. *Experiments in fluids* 39.3, pp. 498–506.

- Taylor, G. (1960). “Formation of thin flat sheets of water”. *Proceedings of the Royal Society of London A: Mathematical, Physical and Engineering Sciences* 259.1296, pp. 1–17.
- V. Donk, Jan A. C. (1981). *Water aeration with plunging jets*. TU Delft, Delft University of Technology.
- Villermaux, E. & Clanet, C. (2002). “Life of a flapping liquid sheet”. *Journal of Fluid Mechanics* 462, pp. 341–363.
- Visser, C. W., Frommhold, P. E., Wildeman, S., Mettin, R., Lohse, D., & Sun, C. (2015). “Dynamics of high-speed micro-drop impact: numerical simulations and experiments at frame-to-frame times below 100 ns”. *Soft matter* 11.9, pp. 1708–1722.
- Wadhwa, N., Vlachos, P., & Jung, S. (2013). “Noncoalescence in the oblique collision of fluid jets”. *Physical review letters* 110.12, p. 124502.
- Walls, Peter LL, Henaux, Louis, & Bird, James C (2015). “Jet drops from bursting bubbles: How gravity and viscosity couple to inhibit droplet production”. *Physical Review E* 92.2, p. 021002.
- Xie, Luo, Yang, Li-jun, & Ye, Han-yu (2017). “Instability of gas-surrounded Rayleigh viscous jets: Weakly nonlinear analysis and numerical simulation”. *Physics of Fluids* 29.7, p. 074101.
- Yang, L.-J., Zhao, F., Fu, Q.-F., & K.-D.Cui (2014). “Liquid sheet formed by impingement of two viscous jets”. *Journal of Propulsion and Power* 30.4, pp. 1016–1026.
- Yang, X. & Turan, A. (2017). “Simulation of liquid jet atomization coupled with forced perturbation”. *Physics of Fluids* 29.2, p. 022103.
- Zhang, P. & Wang, B. (2017). “Effects of elevated ambient pressure on the disintegration of impinged sheets”. *Physics of Fluids* 29.4, p. 042102.
- Zhu, Y., Oguz, H. N., & Prosperetti, A. (2000). “On the mechanism of air entrainment by liquid jets at a free surface”. *Journal of Fluid Mechanics* 404, pp. 151–177.

Publications

Relevant to current work

Journal

Published

Sanjay, V. & Das, A. K. (2017a). “Formation of liquid chain by collision of two laminar jets”. *Physics of Fluids, Impact Factor = 2.232*, 29.11, p. 112101. DOI: [10.1063/1.4998288](https://doi.org/10.1063/1.4998288).

Sanjay, V. & Das, A. K. (2017b). “On air entrainment in a water pool by impingement of a jet”. *AICHE Journal, Impact Factor = 2.836*, 63.11, pp. 5169–5181. DOI: [10.1002/aic.15828](https://doi.org/10.1002/aic.15828).

In Press / Under Review

Jain, A., **Sanjay, V.**, & Das, A. K. (2018). “Consequences of inclined and dual jet impingement in stagnant liquid and stratified layers”. *AICHE Journal, Impact Factor = 2.836*.

Soni, A., **Sanjay, V.**, & Das, A. K. (2018). “Formation of fluid structures due to jet-jet and jet-sheet interactions”. *Chemical Engineering Science, Impact factor= 2.895*.

Conference

Aggarwal, A., **Sanjay, V.**, Kumar, P., & Das, A. K. (2016). “Generation of a liquid sheet by an oblique impingement of interacting jets: a numerical investigation”. Paper ID: 267, *Proceedings of Chemcon*.

Jain, A., **Sanjay, V.**, & Das, A. K. (2017a). “Asymmetry in air entrainment inside liquid pool due to impingement of an inclined jet”. Paper ID: IHMTC2017-13-0828; *24th National and 2nd International ISHMT-ASTFE Heat and Mass Transfer Conference*.

Jain, A., **Sanjay, V.**, & Das, A. K. (2017b). “Interaction of bubble clusters formed due to adjacent impingement of liquid jets in a pool”. *Paper ID: 68, 44th National Conference on Fluid Mechanics and Fluid Power*.

Soni, A., **Sanjay, V.**, & Das, A. K. (2017). “Consequences of interaction between asymmetric liquid jets”. *Paper ID: 64, 44th National Conference on Fluid Mechanics and Fluid Power*.

Sanjay, V. & Das, A. K. (2015a). “Bubble life cycle during entrainment by Jet impingment in liquid pool”. *ID FM-052, Proceedings of Chemcon*.

Sanjay, V. & Das, A. K. (2016a). “On the gas-liquid entrainment by impingement of liquid jet onto a pool”. *Paper ID: 50, 9th International Conference on Multiphase Flow*.

Other Publications

Journal

Published

Sanjay, V. & Das, A. K. (2018). “Numerical assessment of hazard in compartmental fire having steady heat release rate from the source”. *Building Simulation, Impact Factor = 1.170*, 11.3, pp. 613–624.

In Press / Under Review

Rathia, S. K., **Sanjay, V.**, & Das, A. K. “Numerical understanding of fire in patterned obstructions: effect of spacing, multi-point ignition, and wind speed”. *Under Review*.

Conference

Agarwal, Abhishek, Sarda, Manoj, Kaushik, Juhi, **Sanjay, V.**, & Das, Arup Kumar (2016). “Investigation of Flame and Soot Propagation in Non-Air Conditioned Railway Locomotives”. *World Academy of Science, Engineering and Technology, International Journal of Energy and Power Engineering* 3.9.

Datta, S., **Sanjay, V.**, Kumar, P., & Das, A. K. (2016). “Investigation of Jet Atomization -A Multi-scale Approach”. *Paper ID: 218, 44th National Conference on Fluid Mechanics and Fluid Power.*

Kaushik, Juhi, Agarwal, Abhishek, Sarda, Manoj, **Sanjay, V.**, & Das, Arup Kumar (2016). “Study of Fire Propagation and Soot Flow in a Pantry Car of Railway Locomotive”. *World Academy of Science, Engineering and Technology, International Journal of Mechanical, Aerospace, Industrial, Mechatronic and Manufacturing Engineering* 10.9, pp. 1696–1701.

Rathia, S. K., **Sanjay, V.**, & Das, A. K. (2017a). “Extent of fire spread during interaction of two ignition points”. *Paper ID: 65, 44th National Conference on Fluid Mechanics and Fluid Power.*

Rathia, S. K., **Sanjay, V.**, & Das, A. K. (2017b). “Study of fire propagation in the presence of patterned flammable obstructions”. *Paper ID: IHMTC2017-04-0814, 24th National and 2nd International ISHMT-ASTFE Heat and Mass Transfer Conference.*

Sarda, Manoj, Agarwal, Abhishek, Kaushik, Juhi, **Sanjay, V.**, & Das, Arup Kumar (2016). “Numerical Simulations of Fire in Typical Air Conditioned Railway Coach”. *World Academy of Science, Engineering and Technology, International Journal of Computer, Electrical, Automation, Control and Information Engineering* 10.9, pp. 1666–1673.

Sanjay, V. & Das, A. K. (2015b). “Building Fire Safety: Numerical Simulation and Evacuation Planning”. *14th International Conference of the International Building Performance Simulation Association.*

Sanjay, V. & Das, A. K. (2016b). “On the Numerical Simulations of Kitchen Sink Vortex”. *Paper ID: 217, 44th National Conference on Fluid Mechanics and Fluid Power.*

Sanjay, V., B., Darshan M., P., Kumar, & Das, A. K. (2017). “Spatial preference of film growth in boiling and localized suppression of bubble release”. *Paper ID: IHMTC2017-09-1283, 24th National and 2nd International ISHMT-ASTFE Heat and Mass Transfer Conference.*